Shell Model Study of the Shape Coexistence in Doubly Magic ^{40}Ca

* * *

Nuclear Structure Aspects of the Neutrinoless Double Beta Decay

Memoria de Tesis presentada para optar al grado de Doctor por

Javier Menéndez Sánchez

Dirigida por el Profesor

Alfredo Poves Paredes

Departamento de Fisica Teórica
Facultad de Ciencias
Universidad Autónoma de Madrid
Enero 2009

Contents

1 Introduction **1**

2 Nuclear Structure Models **11**

2.1 Introduction 11

2.2 Ab initio methods 12

2.3 Self Consistent Mean Field 13

2.4 Interacting Shell Model 14

2.4.1 The original Shell Model 14

2.4.2 The ISM: Choice of the basis states 15

2.4.3 The valence space 18

2.4.4 The effective interaction 20

2.4.4.1 The monopole and multipole Hamiltonians . . . 22

2.4.5 The solution of the Schrödinger equation 24

3 Study of the Shape Coexistence in the nucleus ^{40}Ca **27**

3.1 Introduction 27

3.1.1 Collective behaviour in nuclei 28

3.1.2 Collective behaviour within the ISM 29

3.2 Previous works on shape coexistence and ^{40}Ca 31

3.3 Valence space and effective interaction 33

3.4 Results of the calculations at fixed $n\hbar\omega$ 34

3.5 Energies of the $n\hbar\omega$ bandheads relative to the closed shell 38

3.6 Results of the complete calculations in the r_2pf space 43

3.6.1 The superdeformed band 44

3.6.2 The normal deformed triaxial bands 48
3.6.3 Out-band transitions 52
3.7 Summary 58

4 Study of the Neutrinoless Double Beta Decay: General Considerations 61
4.1 Introduction 61
4.2 Theoretical framework 65
4.2.1 Short range correlations 71
4.3 Results of NME's of $0\nu\beta\beta$ decays 72
4.3.1 Gamow-Teller, Fermi and Tensor components 75
4.3.2 HOC, FNS and SRC contributions 75
4.3.3 Final value of the NME's 79
4.4 Radial dependence of the NME 82
4.5 Transitions to excited final states 83
4.6 Summary 86

5 Study of the Neutrinoless Double Beta Decay: Nuclear Structure Aspects 89
5.1 Introduction 89
5.2 Pairing and the $0\nu\beta\beta$ decay 90
5.2.1 Pairing and the full NME 90
5.2.2 Pairing and the Fermi and Tensor components 97
5.2.3 Pairing and the HOC, FNS and SRC contributions 99
5.3 Deformation and the $0\nu\beta\beta$ decay 100
5.3.1 Unphysical mirror $\beta\beta$ decays 101
5.3.2 Real $0\nu\beta\beta$ decays 107
5.3.3 Pairing and deformation 111
5.4 Occupancies on the $A = 76$ $0\nu\beta\beta$ decay 115
5.5 Summary 121

6 Conclusions and perspectives 123

A Algebraic models and nuclear deformation 133
A.1 The Elliott SU(3) model 133

A.2 The pseudo-SU(3) model 136
A.3 The quasi-SU(3) model 137

B The Center of Mass **141**

C Analytical form of the neutrino potentials **145**

List of Figures **151**

List of Tables **155**

Bibliography **159**

Chapter 1

Introduction

The origins of what we understand nowadays as nuclear physics date back to the late nineteenth century, with the discovery of radioactivity by Becquerel and the pioneering studies of radioactive substances by Marie and Pierre Curie. However, it was not until 1911 that the very existence of atomic nuclei was first proposed by Rutherford, following the celebrated gold foil experiment [1]; he was studying, at that time, the ultimate components of matter.

Some years had to pass before Heisenberg, in 1932, shortly after the discovery of the neutron by Chadwick [2], proposed the first Nuclear Structure model [3]. Nowadays, more than 75 years after this seminal work, Nuclear Structure, in spite of the overwhelming achievements managed in the way, remains a field of quite active scientific research. It is true that its foundations seem rather solid: Quantum Chromodynamics (QCD) provides the theoretical background for the interaction between quarks and gluons, the ultimate component of nucleons. On the other hand if, as is ordinarily assumed in Nuclear Structure, we consider these protons and neutrons as the basic building blocks of atomic nuclei, Schrödinger's equation —Dirac's in the relativistic case— holds.

Nevertheless, when trying to solve the problem of atomic nuclei by applying these theories we face several problems that eventually lead to the complexity and richness of Nuclear Structure. On the one hand QCD, while well known at high energies —where it can be treated perturbatively— has not been solved yet at the low energies that concern the nuclear problem. On the other hand, even in the

case that we knew with full confidence the interaction, based on QCD, to be used, when solving the Schrödinger equation we face the problem of many interacting bodies, which cannot be solved analitically nor numerically in general —indeed, for more than four bodies—. In addition to that, this quantum many body problem is mesoscopic, this is, the number of nucleons involved in nuclei is not large enough to apply statistical mechanics' techniques.

These difficulties are the reason that, even though the growth of knowledge on nuclear systems has been huge over the past 75 years, open questions still remain to be answered. Which is also due to the wide variety of phenomena that atomic nuclei exhibit: beginning with the nuclear binding energies and the related topic of the limits of nuclear stability (driplines); nuclear spectra that can show both single particle behaviour —magnetic moments, giromagnetic factors or multiparticle-hole states— and, at the same time, collective features —rotational bands, vibrational states, giant resonances; nuclear decays such as beta, double beta, fussion, fission; several types of nuclear reactions... To mention only a few.

The present state of the art in Nuclear Physics tries to improve our understanding of all the nuclear processes and properties —like those presented in the last paragraph— either by improving the present methods and models or by developing new techniques. At the same time, notable interest is placed to reduce the gap between QCD and what we understand as Nuclear Structure. Specially important is the problem of the nuclear interaction, which in principle could be obtained only from QCD —or, hopefully, from enough empirical data— and which is obviously central in Nuclear Physics. To these effects, the use of enhanced computational capacities has become a very valuable tool. In any case, in spite of all the efforts of the Nuclear Physics community to give an structured, detailed and precise description of all nuclear phenomena, the time for all —interesting— problems to be solved does not seem to be close.

At the same time, new experimental facilities keep on collecting new data with which we can test and improve the theoretical comprehension of nuclei. Among present topics of study we can mention the shape coexistence in nuclei —which is treated in this work—, the determination of the driplines, the disappearance of classical magic numbers and the appearance of new ones in nuclei far from the valley of stability or the occurrence of phase transitions in isotopic chains. All

this new data and much more that are expected to come out in the new facilities planned like FAIR at GSI, SPIRAL2 at GANIL, RIBF at RIKEN or the future FRIB —the first two in Europe, the third in Japan and the latter in the USA— pose a very appealing challenge for theoretical nuclear physics in order to be able to successfully explain all these new phenomena.

All this said, perhaps it is time to mention why should we bother at all to study systems such as nuclei. The importance of Nuclear Physics knowledge, very much related to Quantum Mechanics, is difficult to exaggerate. Historically, the obtention of energy through nuclear fission may have been the most obvious but this is by no means the most relevant process related to nuclei —and nuclear plants are still being built today; as a non polluting energy source, their use may rise in the future. The energy coming from stars —e.g. the sun— comes from nuclear fussion, which is in addition responsible of the creation of light elements —including carbon. In addition to that, all heavy elements come from beta decays or fission processes that happen after supernova explosions, and these are nuclear processes as well. Now we see that there is a strong link between Nuclear Physics and astrophysics. Hence the knowledge of nuclei helps also to the understanding of the origin, evolution and composition of the Universe —not so surprisingly, since the Universe is composed mainly, in the parts we understand today, of nuclei and photons. Of course, there are other fields in which the insights gained by Nuclear Physics are of the utmost importance. One of these —which is treated in this work— is particle physics. In particular, double beta decay will be very well key to identify the very nature of neutrinos, as well as their mass. This is, with the help of Nuclear Physics we could obtain the information about physics beyond the Standard Model of high energy physics. To mention only one further example, the applications of Nuclear Physics to medicine are growing constantly: devices such as magnetic resonance imaging (MRI) or positron emission tomography (PET) have been only possible by the previous grasp of the underlying nuclear phenomena involved.

In summary, Nuclear Physics has been for nearly eight decades a prominent field of scientific research and, in spite of the spectacular advances that it has undergone —useful also in other branches of physics, and even beyond—, still today many interesting questions wait to be solved. In the present thesis work, a —very— tiny contribution has been tried to be made.

The structure of the memory is as follows. In Chapter 2 the most relevant models and methods that are used to solve the Nuclear Structure problem are introduced. Then, special emphasis is given to the Interacting Shell Model, within which this work has been performed. The framework of the model is presented in detail and the principal advantages —good quantum numbers, rich correlations— and drawbacks —non unique determination of the interaction, limitation to treatable valence spaces— of the method are exposed. A description of the codes used to obtain the results of this work is also given.

With the theoretical framework already settled, the following Chapters present the results fruit of the present research. The work has been accomplished in two relatively different topics. First, in a pure Nuclear Structure problem as is the study of the shape coexistence in the nucleus ^{40}Ca. This doubly magic nucleus presents three different structures at low energy: the spherical ground state plus a deformed and a superdeformed intrinsic states. In the Chapter 3, the results obtained within the Interacting Shell Model context are presented. The very existence of the spherical ground state and the two deformed bands is studied, as well as the out-band transitions that connect states with different nature.

Chapter 4 is devoted to the other topic studied, which is the study of the —still unobserved— neutrinoless double beta decay process. It may occur in some selected nuclei and its observation will stablish the nature of neutrinos, as mentioned above. A complete study of the process is performed. Results are obtained for the Nuclear Structure part of the process —the Nuclear Matrix Element. Much interest has been placed to understand to which parts of the transition operator and the nuclear wave functions the final result is most sensitive. As a result, the role of topics like short range correlations, deformation or seniority truncations in the Nuclear Matrix Element is explored. This study is required to estimate the uncertainties of the calculation and to establish how stable the obtained results are.

Finally, some conclusions and perspectives of future work are outlined in Chapter 6.

Introducción

El origen de lo que hoy en día se conoce como Física Nuclear se remonta a finales del siglo XIX, con el descubrimiendo de la radiactividad por Bequerel y los estudios pioneros, de Marie y Pierre Curie, con sustancias radiactivas. Sin embargo, el núcleo atómico no fue propuesto hasta 1911, cuando Rutherford lo hizo tras los resultados de su célebre experimento de la lámina de oro, en su búsqueda de los últimos componentes de la materia [1].

Aún tuvieron que pasar algunos años antes de que Heisenberg, en 1932, poco después del descucbrimiento del neutrón por Chadwick [2], propusiera el primer modelo de Estructura Nuclear [3]. Hoy, más de 75 años despúes de este trabajo fundacional, la Estructura Nuclear, a pesar de la increíble cantidad de logros que ha conseguido, continúa siendo un campo con una gran actividad científica. Ciertamente, los pilares en los que se fundamenta parecen muy sólidos: la cromodinámica cuántica (QCD) proporciona el marco teórica para las interacciones entre quarks y gluones, que son los componenetes últimos de los núcleos. Por otro lado, si, como se supone normalmente en Estructura Nuclear, consideremos a protones y neutrones como los componentes básicos de los núcleos atómicos, la dinámica nuclear está dictada por la ecuación de Schrödinger —o la de Dirac, en el caso que adoptemos un enfoque relativista.

Sin embargo, cuando tratamos de resolver el problema del núcleo atómico aplicando estas teorías, nos encontramos con una serie de problemas que, al final, no son sino los responsables de la complejidad y riqueza de la Estructura nuclear. Por un lado, tenemos que QCD, que se conoce muy bien a altas energías —donde se puede tratar de manera perturbativa— aún no ha sido resuelta a bajas energías, que son las relevantes para el problema que nos ocupa. Por otra parte, incluso en

el caso de que conociésemos perfectamente la interacción, proveniente de QCD, cuando tratamos de resolver la ecuación de Schrödinger nos encontramos con un problema de muchos cuerpos interactuantes, que no se sabe resolver númericamente para más de cuatro cuerpos. Es más, este problema cuántico de muchos cuerpos es mesoscópico, es decir, el número de nucleones que hay en el núcleo no es suficiente para aplicar técnicas de Física Estadística.

Estas dificultades muestran por qué, aunque el conocimiento de los sistemas nucleares ha aumentado enormemente durante los últimos 75 años, aún quedan numerosas cuestiones por resolver. Esto se debe tambien a la amplia variedad de fenómenos que nos podemos encontrar cuando estudiamos el núcleo atómico: comenzando por las energías de ligadura nucleares y los límites de estabilidad nucleares (líneas de goteo); espectros de energía que presentan tanto comportamientos de partícula independiente, tales como momentos magnéticos, factores giromagnéticos, estados multi-partícula–hueco; y, al mismo tiempo, carácterísticas colectivas como bandas rotacionales, estados vibracionales o resonancias gigantes; también podemos encontrar desintegraciones nucleares, ya sean de tipo beta, doble beta, fusión, fisión; numerosos tipos de reacciones nucleares... Solo por mencionar algunos de los fenómenos que podemos encontrar en núcleos atómicos.

Actualmente, la Física Nuclear trata de mejorar el conocimiento sobre todos estos comportamientos, bien sea mejorando los métodos y modelos existentes o bien introduciendo nuevas técnicas. Al mismo tiempo, es de gran interés reducir la distancia que actualmente separa QCD y la Estructura Nuclear. Respecto a esto, un problema especialmente importante es el de la interacción nuclear, que en principio debería poder calcularse a partir de QCD —o de los datos empíricos de dispersión nucleón–nucleón. A este respecto, la capacidad computacional ha pasado a ser una herramienta fundamental. En todo caso, a pesar de todos los esfuerzos de la comunidad de Física Nuclear por obtener una descripcion estructurada, detallada y precisa de todos los fenómenos relacionados con la disciplina, el momento en que todos los problemas —interesantes— hayan sido resueltos parece bastante lejano.

Al mismo tiempo, nuevos complejos experimentales siguen consiguiendo nuevos datos con los que podemos comprobar y mejorar nuestra comprensión teórica de los núcleos. Entre los temas más actuales que se están estudiando se pueden mencionar la coexistencia de forma en núcleos —que es parte de este trabajo—, la

determinación de las líneas de goteo, la desaparición de los números mágicos "clásicos" y la aparición de otros nuevos en núcleos alejados del valle de la estabilidad o la existencia de transiciones de fase en cadenas isotópicas. Todos estos nuevos datos y muchos más que se esperan de las nuevas instalaciones planificadas como FAIR en GSI, SPIRAL2 en GANIL, RIBF en RIKEN o la futura FRIB —las dos primeras en Europa, la tercera en Japón y la última de los Estados Unidos— forman un estimulante reto para la Física Nuclear teórica, que tratará de explicar satisfactoriamente los nuevos fenómenos que sean descubiertos.

Habiendo dicho esto, tal vez sea el momento de pasar a mencionar por qué deberíamos molestarnos en estudiar sistemas como los núcleos atómicos. La importancia del conocimiento de la Física nuclear, íntimamente relacionada a la de la Mecánica Cuántica, es difícil de exagerar. Históricamente, la obtención de energía a través de la fisión nuclear es la razón más evidente y, hoy día las centrales nucleares, que son una fuente de energía no contaminante —excluyendo sus propios residuos— son utilizadas y construidas, y su uso podría aumentar en el futuro. Sin embargo, esta no es el proceso más relevante que tiene a los núcleos como protagonistas. La energía que generan las estrellas —por ejemplo, el Sol— tiene su origen en la fusión nuclear que, además, es la responsable de la creación de todos los elementos (átomos) ligeros, el carbono incluido. Es más, todos los elementos pesados existen gracias a explosiones de supernovas y las desintegraciones beta o fisión posteriores que se producen en los núcleos inestables creados en dicho procesos. El vínculo entre Física Nuclear y Astrofísica es, entonces, patente, así como lo es el hecho de que el conocimiento de los núcleos sea esencial para comprender el origen, evolución y composición de nuestro Universo —esto no es tan sorprendente dado que el Universo está formado fundamentalmente, en las partes que comprendemos hoy en día, de núcleos y fotones. Por supuesto, hay otros muchos campos en los que la Física Nuclear es de gran importancia. Uno de ellos es la Física de Partículas. En concreto, las desintegraciones dobe beta —que son estudiadas en este trabajo— pueden ser la clave para determinar la naturaleza de los neutrinos, así como su masa. Esto es, con ayuda de la Física Nuclear, podemos obtener información acerca de Física más allá del Modelo Estándar de Física de Altas Energías. Para mencionar solamente un ejemplo más, las aplicaciones de la Fisica Nuclear a la medicina son cada día más numerosas: dispositivos como

las Resonancias Magnéticas o las Tomografías solamente son posibles gracias al dominio previo de los fenómenos de Física Nuclear subyacentes a estas técnicas.

En resumen, la Física Nuclear ha sido durante cerca de ocho décadas un campo de excelente investigación científica y, a pesar de los espectaculares avances que se han producido en él —útiles no sólo dentro sino también fuera de la comunidad de la Física Nuclear— hoy en día aún quedan muchas preguntas por responder. Este trabajo de tesis trata de ser una —muy— pequeña contribución.

La estructura de esta memoria es la siguiente. En el Capítulo 2 se exponen los métodos y modelos más relevantes que se emplean para resolver el problema de la Estructura Nuclear, con especial énfasis en el Modelo de Capas Interactuante, en cuyo marco se encuadra este trabajo. Dicho modelo se presenta en detalle y tanto las principales ventajas —buenos números cuánticos, correlaciones muy ricas entre nucleones— como sus inconvenientes —limitación de los espacios de valencia— se discuten ampliamente. Además, se describen los códigos que se han usado para obtener los resultados de este trabajo.

Una vez que el método ha quedado discutido, en los Capítulos siguientes se preentan los resultados obtenidos. A lo largo de este trabajo se han tratado dos temas relativamente diferentes. En primer lugar, un problema de Estructura Nuclear pura como es el estudio de la coexistencia de forma en el núcleo doblemente mágico ^{40}Ca. Este núcleo presenta tres estructuras de diferente naturaleza a baja energía: el estado fundamental esférico y dos estados intrínsecos uno deformado y otro superdeformado. En el Capítulo 3, se presentan los resultados obtenidos en el marco del Modelo de Capas Interactuante. En él, se estudian tanto la existencia del estado fundamental esférico y las dos bandas rotacionales como las transiciones que conectan estados de distinta naturaleza.

El Capítulo 4 está dedicado al otro tema estudiado que es la desintegración doble beta sin neutrinos —aún no observada experimentalmente—. Este proceso podría ocurrir en algunos núcleos y su observación establecería, como se ha dicho anteriormente, la naturaleza de los neutrinos. En él se presenta un estudio completo acerca de este proceso. No solamente se exponen los resultados obtenidos de la parte correspondiente a la Estructura Nuclear de estos procesos —los Elementos de Matriz Nucleares— sino que una buena parte del Capítulo se dedica a comprender qué componentes del operador de transición o de las funciones de onda influyen

más en el resultado final. Así, se estudia el papel de las correlaciones de corto alcance, la deformación o las truncaciones en “seniority” de los núcleos inicial y final. Estas consideraciones son necesarias para estimar las incertidumbres de nuestros cálculos, así como para establecer cómo de estables son los resultados que hemos obtenido.

Para terminar, se mencionan algunas conclusiones y perspectivas para posteriores trabajos en el Capítulo 6.

Chapter 2

Nuclear Structure Models

2.1 Introduction

As we sketched in the Introduction, the problem of nuclear structure, —the subject of this work— is that of many quantum interacting bodies, with the extra difficulty that the actual interaction is not completely known.

Since this problem is so complex not to be exactly solvable —apart from a small number of nuclei— several methods or models have been proposed to deal with it. None is completely successfull to describe all nuclear features or all nuclei appearing in the nuclear chart, and generally, depending on which nuclei or properties are under study one or other method may be preferred.

We can classify the most successful methods in describing nuclear structure in three main categories: ab initio calculations, self consistent mean field techniques (SCMF) and the interacting shell model (ISM).

The common feature of these models is that they all take, as fundamental components of nuclei, protons and nucleons, not their internal degrees of freedom —quarks and gluons—, which are not considered to play a role at nuclear structure energies. Within this approach, each method chooses a determinate configuration space to pose the problem and an interaction adapted to it. Then, the Schrödinger —or Dirac's— equation is solved.

Letting aside the ab initio methods, which can deal with a very limited number of nucleons, both SCMF and ISM are based upon the idea of the Mean Field. This

is, even though the interaction between nucleons is 'strong', when forming nuclei it can be seen that nucleons behave as independent particles moving in a common —Mean Field— potential. This idea, taken from atomic physics, might seem hardly appropriate for the case of nuclei due to the strength of the interaction. However, that effective strength in nuclei is softened, for instance by the fermionic nature of nucleons: the Pauli principle, in the nuclear medium, blocks many of the available states, and consequently the effect of the interaction is reduced. Eventually, the soundness of this Mean Field approximation is supported by the nuclear observables which abundantly have corroborated the validity of the models that are based upon this simple approximation.

2.2 Ab initio methods

Ab initio calculations try to solve the nuclear problem of interacting nucleons, without any additional approximation. The interactions used come from fits to experimental nucleon-nucleon data, and the configuration space is large enough to contain all states of practical interest at low lying nuclear structure. Hence, these are essentially exact calculations.

Among these methods we can distinguish those that can be used up to $A \leq 4$ — A, the mass number, denotes number of nucleons. The best known are the Fadeev-Yakubovsky equations —first exact solution of an $A = 3$ nucleus [4]— or the hyperspherical harmonics variational method [5], even though other mainly variational procedures exist. The results obtained are very similar between different methods, as much as 0.5% convergence for ^{4}He, so we can speak safely of an exact solution [6, 7].

The Green Function Monte Carlo approach (GFMC) [8, 9] can also account for the above nuclei but also has been applied to nuclei up to $A \simeq 12$. It is based on the variational principle, and from a set of trial wave functions the energy is minimized. The corresponding integrals are evaluated through the Monte Carlo algorithm. It was within this method that, for the first time, exact results for nuclei with $A = 6 - 10$ could be obtained [10, 11, 12].

One can study essentially the same region with the No Core Shell Model (NCSM) [13, 14], which is a especial kind of Interacting Shell Model —it will

be explained in detail in Section 2.4— in which no restrictions are placed upon the configuration space. This method also allows us to explore nuclei up to the mid *p* shell.

One the main achievements of these two methods is that after these calculations the need of three body forces in nuclei was first stablished. Particularly crucial was to show that the spectrum of ^{10}B could not be satisfactorily explained unless some three body potential was assumed [12, 15, 16].

The handicap of these ab initio methods is that their complexity grows exponentially with the number on nucleons *A* involved, so they cannot be applied to much heavier nuclei. Hence, other type of models are required to attack the nuclear problem in other regions. Another ab initio approach close to those above is that of the recently proposed (modern) coupled cluster methods (CCM) [17, 18]. The idea is that *n*-body cluster expansion is performed, and the method converges well enough to be sure that most correlations are included at some level. The advantage of this methods is that it shows polynomial complexity growth with *A*, and consequently appears very promising for the future. Up to now, only selected nuclei have been studied within these techniques [19, 20, 21].

In any case, nowadays the two standard models to treat the many body problem in non-light nuclei are the SCMF and the ISM. As we said above, both are based on the idea of a Mean Field in the nuclear medium.

2.3 Self Consistent Mean Field

The Self Consistent Mean Field method solves variationally the *A* body problem in a very large configuration space with a universal —common for light, medium and heavy nuclei— nuclear interaction. This interaction is obtained by fitting properties of selected nuclei such as binding energies and radii and, to obtain realistic results, it must be density dependent. Depending on the interaction used, different branches of this method can be distinguished: calculations performed with the family of Skyrme interactions [22, 23, 24, 25], those using the Gogny force [26, 27] and, more recently, the relativistic mean field interaction [28].

Then, the Hartree-Fock or Hartree-Fock-Bogoliubov (HFB)—the Bogoliubov part is required to treat pairing properly— self consistent method is applied to solve

the nuclear problem. This gives a Mean Field solution whose wave function is a single Slater determinant —or a product type wave function in the more general HFB case—, not accurate enough for standard purposes. To improve on this, beyond Mean Field techniques are used. For instance, the variational configuration space is enlarged by means of the projection techniques, which consist in restoring the symmetries inherent to the Hamiltonian —such as particle number or rotational symmetry— that are not preserved by the HFB method [29]. In addition to that, not only one solution is considered but a linear combination of non orthogonal Mean Field states, following the Generating Coordinate Method (GCM). Here, the coefficients of the linear combination are found by diagonalizing the full Hamiltonian in this restricted configuration space.

As already mentioned above, the most appealing virtue of this methods is their universality: they can cover the full nuclear chart on the same ground, in the Gogny case altogether with the same effective interaction, which gives the method a great capacity to explain many different properties in quite different nuclear regions [30, 31]. On the other hand, this SCMF–and–beyond description usually lacks of important degrees of freedom —triaxiality— or correlations —particle-hole excitations—, whose inclusion into the method increases considerably the complexity of the calculations.

As a consequence, whenever the calculations are feasible, the results of the Interacting Shell Model tend to be more accurate than those of the SCMF.

2.4 Interacting Shell Model

2.4.1 The original Shell Model

Finally, we have the Interacting Shell Model. Its origin dates back to the discovery, in the 1930's, that nuclei with special proton or neutron numbers exhibited properties of closed shells, similarly to what happens in atoms. This is, the first proton (or neutron) beyond these numbers was shown to be less bound than the previous one. These numbers were called the magic numbers, and in the nuclear case were found to be at first 8, 20 and in the next decade also 50, 82 and 126 [32]. Even though the first two could be obtained from a simple potential —a square well potential or a

harmonic oscillator potential— 50, 82 and 126 were more difficult to explain, and this lead to some skepticism on the idea of a Shell Model in nuclei. It was in 1949 when, as the evidence of these shell closures became experimentally more evident, Goeppert-Mayer [33] and independently Haxel, Jensen and Suess [34] gave the correct description of the Mean Field potential: a harmonic oscillator with a large spin-orbit term. With the minor addition of a surface correction term to better fit the experimental numbers, this potential looks like:

$$U(r) = \frac{1}{2}\hbar\omega\mathbf{r}^2 - D\mathbf{l}^2 - C\mathbf{l}\cdot\mathbf{s}. \tag{2.1}$$

This original Shell Model (SM) is able to explain, for instance, spins and parities of states consisting of a closed shell plus (minus) a single nucleon, since the net contribution would come only from this extra (missing) nucleon —being the rest of the nucleons coupled to a 0^+ state as corresponding to a shell that is closed. It also successfully accounted for other nuclear properties such as the magnetic moments of these particular nuclei, systematics on beta decay and nuclear isomerism [35]. Given such an agreement between theory and experiment the basis of the SM was settled.

2.4.2 The ISM: Choice of the basis states

Even though the main feature of the ISM is the independent particle motion in this Mean Field, a further step is to take into account not only this potential but also the residual interaction between nucleons, which will lead to correlations absent in the Mean Field. This interaction can be seen as a correction to the Mean Field, and consequently it will be treated perturbatively acting on the unperturbed space generated by it. Hence, we have the following situation for our Hamiltonian:

$$\begin{aligned} H &= \sum_{i=1}^{A} t_i + \sum_{i\leq j}^{A} v_{ij} \\ &= \left(\sum_{i=1}^{A} (t_i + u(r_i))\right) + \left(\sum_{i\leq j}^{A} v_{ij} - \sum_{i=1}^{A} u(r_i)\right) \end{aligned}$$

$$
\begin{aligned}
&= \sum_{i=1}^{A} h_i + \sum_{i \leq j}^{A} \widetilde{v}_{ij} \\
&= H_0 + H_{res}.
\end{aligned} \tag{2.2}
$$

The H_0 is the average potential that will give us the independent particle motion, and at the same time will fix our single particle wave functions. Since we are dealing with a self-bound system with a rotationally invariant Hamiltonian, the best choice is the isotropic —three dimensional— harmonic oscillator, which naturally quantizes our states. Moreover, this election is also supported by Eq. (2.1). Consequently, our major oscillator shells will be given by the oscillator principal number p. The orbits forming these major shells are: $0s_{1/2}$ for $p = 0$, $0p_{1/2}$ and $0p_{3/2}$ for $p = 1$, $1s_{1/2}$, $0d_{3/2}$ and $0d_{5/2}$ for $p = 2$, and so on. The complete relation of orbits can be seen in Figure 2.1, where it is also shown how the presence of the large spin-orbit coupling present in Eq. (2.1) can reproduce the experimental magic numbers.

Hence, the single particle states of our problem can be written as:

$$
a_i^+ \left|0\right\rangle . \tag{2.3}
$$

Thus, our many body basis will be the set of the products of the single particle harmonic oscillator states, and consequently the components of the many body basis will be:

$$
\left|\phi_\alpha\right\rangle = a_{i1}^+ a_{i2}^+ ... a_{iA}^+ \left|0\right\rangle , \tag{2.4}
$$

which is a Slater determinant provided that the antisymmetry of all the states is guaranteed. In this formalism this is obtained by the anticonmutating relation:

$$
\left\{a_i^+, a_j\right\} = \delta_{ij}. \tag{2.5}
$$

Finally, the resulting many body wave function will be a linear combination of these Slater Determinants,

Figure 2.1: Energy levels of the isotropic three dimensional harmonic oscillator and shell structure modification when a large spin-orbit potential is added.

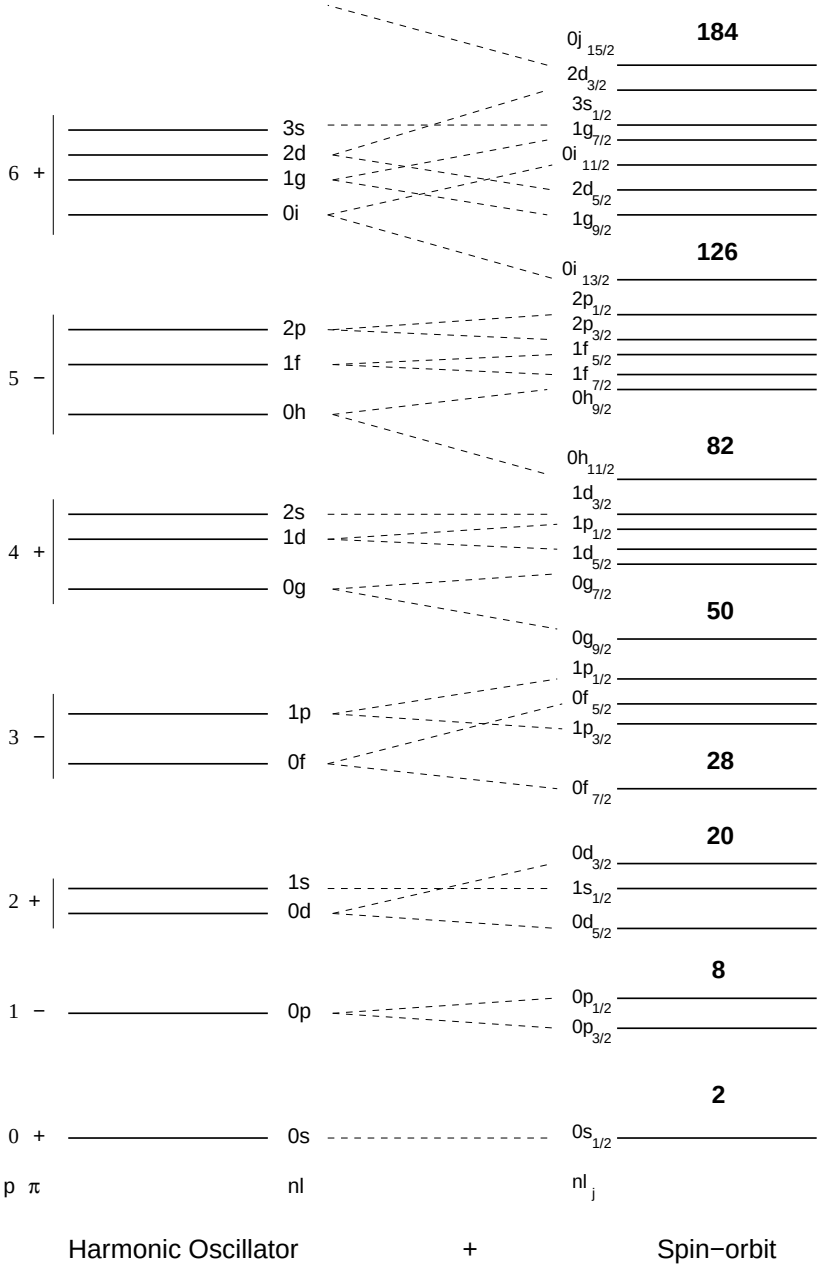

$$|\Psi\rangle = \sum_{\alpha} c_{\alpha} |\phi_{\alpha}\rangle \,. \tag{2.6}$$

2.4.3 The valence space

The problem the ISM faces when dealing with these bases is that, for all nuclei but the lightest ones, the dimension of the configuration space is too large to be treated within the present computing capabilities. This limitation forces us to make some approximation in order to reduce this configuration space, in such a way that the importart degrees of freedom of the system remain and the solution of this reduced problem is still physically sound.

This is done by dividing the configuration space into three different parts:

Inert core — Since we know that the shell structure of nuclei is very well established, we assume that there is an inert core, consisting on several shells, which is always full and hence plays no role in the nuclear problem.
In the few special cases that nuclei are so light that the calculation can be performed even without the assumption of this Inert core, we are dealing with the No Core Shell Model (NCSM) method, already mentioned in Section 2.2.

Valence space — It is the space where the problem will be solved, and typically will consist of one or two major oscillator shells where the available nucleons —which are called the valence nucleons— can be placed, according to the interaction.

Outer space — These are the orbits that will be kept always empty in the calculation, no nucleon is allowed to promote to them.

Hence, in order to solve the problem we have to decide which will be the valence space used. One must notice that, depending on the properties of the nucleus we want to study, a valence space may be adequate or not. For instance, in this work we have used one or two shells, depending on the problem treated. In any case, the issue is to identify the relevant degrees of freedom of each particular situation and incorporate them to the valence space. Clearly, this will not always be

possible, and some correlations due to the absence of active orbits may be missing [36]. Some cures to take into account these effects within the ISM exist, such as effective charges —in the case of electromagnetic transitions— and operators —for example, in the case of single beta decay.

However, even in these valence spaces, when we move into heavier nuclei, even a calculation in a single shell—either oscillator or spin-orbit—, is not feasible without further truncation. To grasp the increasing difficulty in trying to solve the nuclear problem in larger valence spaces, the number of Slater determinants on a single Oscillator shell p with z_v protons and n_v neutrons is given by:

$$\left(\begin{array}{c} (p+1)(p+2)_\nu \\ n_v \end{array} \right) \cdot \left(\begin{array}{c} (p+1)(p+2)_\pi \\ z_v \end{array} \right), \tag{2.7}$$

which grows combinationally. In practice, this number can be slightly reduced by use of the rotational symmetry that degenerates states with the same angular momentum third component m.

This is the major limitation to the ISM, that many nuclei remain beyond present capabilities. Nevertheless, computational resources grow rapidly and also the codes used to solve the nuclear problem are under continuous improvement, so that new nuclei and properties are permanently entering within the range of application of the ISM.

To give a historic perspective of the progress made so far, we can say that until the appearance of modern codes to solve the Schrödinger equation in the late 1960's very small spaces were treatable, such as light nuclei around the $0p$ orbit [37] —or simply p shell, not to be confused with the principal oscillator number, here $p = 1$—, or the $0f_{7/2}$ orbit [38]. With the modern codes, calculations such as ^{16}O with 4 particles in the $0p_{1/2}$, $0d_{5/2}$, $1s_{1/2}$ could be performed [39] and the lower part of the$1s0d$ shell —sd in short, corresponding to $p = 2$— was explored. However it was not until the 1980's that this shell became thoroughly studied [40]. The turn of the next $1p0f$ shell —pf, $p = 3$— came in the 1990's, when systematic calculations were performed [41, 42, 43]. In the recent years calculations on two major shells like $sd - pf$ shells have become feasible [44]. In the case of heavier nuclei, the so called r_3g and r_4h spin-orbit shells have become suitable for standard calculations [45]. The notation r_p means the p oscillator shell

except the highest j orbit, which lowers its energy due to the spin-orbit interaction. In addition to that, these spaces contain also another orbit coming from the next oscillator shell Hence, the r_3g space comprises the $1p_{3/2}$, $1p_{1/2}$, $0f_{5/2}$ and $0g_{9/2}$ orbits. On the other hand the r_4h space is formed by the $1d_{5/2}$, $1d_{3/2}$, $2s_{1/2}$,$0g_{7/2}$ and $0h_{11/2}$ orbits.

2.4.4 The effective interaction

Once we have the basis in which we will solve the problem and we have selected our valence space, we still need a proper interaction between nucleons. It is important to notice that, since we are not working in the full configuration space but in a truncated one, the interaction must be necessarily different than the original one. This is, the problem we are facing is:

$$H\left|\Psi\right\rangle = E\left|\Psi\right\rangle \rightarrow H_{eff}\left|\Psi\right\rangle_{eff} = E\left|\Psi\right\rangle_{eff}, \tag{2.8}$$

since we require the eigenvalues —which are the measurable quantities— to be the same as in the full calculation. The consequence is that each valence space must have an interaction adapted to it, hence we cannot speak of a general interaction but distinguish between different valence spaces.

As can be seen from Eq. (2.2), this interaction will be composed of the single particle energies and some two body matrix elements. In the case of the single particle energies, they can be taken directly from the experimental data of one nucleon outside a close shell or from SCMF calculations —that reproduce these experimental data.

The two body matrix elements constitute the basics of the ISM interaction. There are two different approaches to obtain them. The first is to try to get this part of the nuclear interaction from the bare one stemming from nucleon-nucleon scattering data. Alternatively, a fit to selected nuclei in the region —valence space— of interest can be performed. Both provide interactions that are regularly used with excellent results.

Probably the most appealing method is to obtain the two body matrix elements from the phase-shifts of nucleon-nucleon scattering data at low energies —up to 350 MeV, so that the mesonic degrees of freedom do not appear—, which are

nowadays numerous and known to a very high precision [46]. Based on this data, a number of phenomenological potentials —all based on the idea of meson exchange, this is, the very original idea of Yukawa [47]— have appeared that fit this bare two nucleon interaction [48, 49, 50, 51] with great precission. A more recent idea is to fit the experimental data to potentials derived from quiral effective Field Theory (χEFT), this is, the effective Field Theory coming from QCD at low —nuclear— energies [52, 53]. This χEFT does not know about the internal degrees of freedom of QCD but respects its fundamental symmetries —this is the only thing we need to know about QCD, not the actual path that links it to a particular χEFT or to nuclear physics. Potentials coming from χEFT can be as accurate as the phenomenological potentials with a similar number of parameters [54, 55].

But these data, no matter which potential we are considering, present the inconvenient property that they show a very repulsive core at short distances —two nucleons cannot close too much. As a consequence, the two body matrix elements of the nuclear interaction would diverge. This problem was faced since the origin of the ISM and the solution was provided by Bruekner [56, 57, 58, 59] who developed a method to regularize the bare nucleon-nucleon data into the subject-to-Pauli-principle many body nuclear medium. The result of this process is the so called $G-$matrix [60]. Then, two body nuclear matrix elements can be calculated adapted to the valence space of interest. They were first obtained already in the 1960's for the *sd* and pf shells [61, 62, 63] using as a starting point the Hamada-Johnston nucleon-nucleon potential [64].

A more modern approach to regularize the interaction is the $V_{low\,k}$ method, that eliminates the repulsive hard core at short distances by assuming a large momentum cutoff, using renormalization group ideas, to give a soft —regular at the origin— potential [65, 66]. This method also shows that this soft potential is universal, no matter which of the two-body bare potentials used [67]. Moreover, the two body matrix elements obtained by this $V_{low\,k}$ method and that of $G-$matrices are very similar [68].

The problem posed by the interactions obtained in this way, the so called realistic interactions, is that they are unable to explain properly nuclear structure data. Indeed, the results obtained with realistic interactions deteriorate when the number of particles in the valence space grows, which already led in the 1980's to the USD

fitted interaction for the *sd* shell [40]. On the other hand, some years ago, the development of the GFMC and NCSM methods presented in Section 2.2, permitted to obtain the exact solution of the nuclear problem for light nuclei, and gave the proof that these realistic interactions did not explain the low lying spectra of the nuclei studied [12, 15, 16]. Moreover, when a three body potential was added, the agreement with experiment became apparent. This is, three body interactions —coming from the underlying interaction between quarks— are an intrinsic part of the nuclear interaction. When referring to the two body matrix elements of Eq. (2.2), this means that those provided by the realistic interactions are lacking the contribution of these three body forces, and some modifications are compulsory in order to obtain proper agreement with the experimental data.

The problem that this poses is that very few nucleon-nucleon-nucleon data are known compared to the two body nuclear data, and consequently these effects are difficult to extract from experiment. On the other hand, let us mention that these three body terms arise, in a natural form, at third order (called N^2LO) in the expansion of the nuclear potential given by χEFT. They also can be easily accommodated in the phenomenological potentials, so their presence may not be that much unexpected. We will take up again these phenomenological modifications below.

Conversely, the fitted interactions neither require a regularization process nor present the problem of the lack of three body interactions, since the fit is done to nuclear properties in which these effects are implicitly included. Interactions of this type are also available for the *sd* and pf shells [69, 70]. Besides, the departure point for a fitted interaction can be a realistic one, and the fit in this case will indicate the manner the realistic interaction has to be modified in order to better reproduce experimental nuclear data [71, 45].

2.4.4.1 The monopole and multipole Hamiltonians

In principle, the modifications needed by realistic interactions could be any. However, it turns out that only very selected two body matrix elements need to be varied to obtain experimental agreement. To better understand the nature of these matrix elements it is very useful to separate the Hamiltonian as [72, 73]:

$$H = H_m + H_M, \tag{2.9}$$

where:

H_m is the monopole Hamiltonian, which is defined in such a way that every aspect of the interaction that involves the number of particles is included on it.

H_M is the multipole Hamiltonian, which contains the rest of the interaction. This is, every correlation term, such as paring, quadrupole and other collective contributions, are contained in this part.

The advantage of this separation is that the monopole part satisfies:

$$\langle CS \pm 1 | H | CS \pm 1 \rangle = \langle CS \pm 1 | H_m | CS \pm 1 \rangle , \tag{2.10}$$

where CS means closed shell.

This is, H_m is responsible for the saturation properties of the interaction, as well as every aspect related to independent particle behaviour. In particular, it will give the correct position of single particle stales as predicted by Eq. (2.1).

But these are the precisely the nuclear properties that the realistic interactions fail to reproduce, so it is only the monopole part of a given realistic interaction that needs to be modified. Furthermore, small monopole modifications of realistic interactions cure the experimental disagreement they show. This have been known since the 1970's [74, 75], and has been specially fruitful in the pf shell [76, 43]. How three body monopole corrections could affect realistic interactions in the p, sd and pf shells has been studied in Ref. [77].

To understand why the results obtained with realistic interaction rapidly deteriorate as the number of valence particles, n_i, increases, we can have a look at the diagonal form of the monopole Hamiltonian:

$$H_m = H_{sp} + \sum_{i \leq j} \left[\frac{1}{(1+\delta_{ij})} a_{ij} n_i (n_j - \delta_{ij}) + \frac{1}{2} b_{ij} \left(T_i \cdot T_j - \frac{3}{4} n_i \delta_{ij} \right) \right], \tag{2.11}$$

where H_{sp} contains the single particle energies and T_i represents the isospin operator. The a_{ij} and b_{ij} coefficients are defined as functions of the centroids V_{ij}^T by:

$$\begin{aligned} a_{ij} &= \frac{1}{4}\left(3V_{ij}^1 + V_{ij}^0\right), \\ b_{ij} &= V_{ij}^1 - V_{ij}^0, \\ V_{ij}^T &= \frac{\sum_J V_{ijij}^{JT}(2J+1)}{\sum_J (2J+1)}. \end{aligned} \tag{2.12}$$

This is, only matrix elements which are centroids appear in the monopole Hamiltonian, and consequently only them are subject to modification in realistic interactions. In addition to that, we see that the dependence of H_m on these matrix elements is quadratic in the number of particles, which shows that results are very sensitive to small changes in the centroids. A small deviation in the realistic interaction value of these matrix elements will turn out in poor results when increasing the number of particles.

On the other hand, the multipole Hamiltonian H_M can be shown to be fairly common to different interactions —realistic or not— [78] and does not require any modification since it turns out to take properly into account the nuclear correlations it describes.

2.4.5 The solution of the Schrödinger equation

The last main basic ingredient of the ISM, once the configuration space and the effective interaction are settled, are the codes that will be used to solve the nuclear many body problem. In the case of the ISM, the challenge is to solve the Schrödinger equation in the valence space of our problem, namely Eq. (2.8), which is accomplished by diagonalising the following equation:

$$\langle \Psi_\alpha | H_{eff} | \Psi_\beta \rangle . \tag{2.13}$$

Once the wave function of the nucleus is known, other observables apart from

the energy will be easily obtained by the calculation of the corresponding matrix element involving the appropriate effective operator, final and initial states:

$$o =_i \langle \Psi | \, O \, | \Psi \rangle_f \, . \tag{2.14}$$

Since it is the size of the valence space which poses major limitations on the application of the Shell Model, the aim is to be able to solve this secular equation in the largest possible configuration space. Two different approaches can be followed in order to face the diagonalization that solves Eq. (2.13).

The first is to reduce the dimension of the problem by working with states with good angular momentum —this is called $j-j$ coupling or simply coupled scheme. The drawback is that calculations take longer since they involve cfp's and $9j$ symbols. The main gain of this method is obtained for low angular momentum states, altogether with its capacity to permit to impose, due to its coupling nature, seniority truncations—the seniority counts the number of particles that do not form pairs coupled to $J = 0$. The first modern ISM code, the MULTISHELL [79], was of this type.

The other choice is not to perform any angular momentum algebra and work in the so called *m*-scheme, where each Slater determinant is represented in the computer by an integer word. Every bit takes either the value 1 or 0, depending on whether this particular state is occupied or empty. Now the dimensions of the matrices are maximal, but the calculations have no additional complexity. The first modern code of this type was developed by the Glasgow group [80]. It is also possible to adopt a somewhat mixed approach between *m*-scheme and a coupled code, as is the case of the popular OXBASH code [81, 82].

In this thesis work the advanced computer programs ANTOINE [83, 84] —*m*-scheme— and NATHAN [85, 86]—coupled code— have been used. They have been developed by Caurier and Nowacki [87] and represent a central element of the Strasbourg-Madrid collaboration. These codes take and improve the ideas of the ones described above [88] and are among the most successful and popular concerning the ISM. At present time they allow for diagonalizations of dimensions up to 10^{11} Slater determinants using relatively modest computer computational resources. Accordingly, these are the largest valence spaces that we can treat. To

give some numbers, following the remarks after Eq. (2.7), the full dimension of the pf shell is $2.3 \cdot 10^9$ and that of the r_3g shell $1.3 \cdot 10^{10}$. This is, we can deal with the full pf shell and the r_3g space. Larger valence spaces, like for instance r_4h have to be dealt either without too many active nucleons or with some kind of truncations.

The central idea to carry out the diagonalization is to notice that solving the problem exactly would involve algorithms whose computing time will grow as n^3, being n the dimension of the matrix to diagonalize—which in our case we would like to be as large as possible. Hence, since nuclear structure is mainly interested in the low lying spectra, an approximate calculation is performed instead, in particular taking advantage of the standard Lanczos method, for whom the computing time grows only like n. Other groups have used statistical —Monte Carlo— techniques to save this limitation [89, 90]. Even though the solution obtained is not exact, the associated error to the Lanczos method will be much smaller than other uncertainties of the ISM, for instance those coming from the effective interaction or even for the limitations of the valence space. Hence, we will take the results given by the diagonalization —energies and wave functions— as the actual solutions to our problem.

Which code is to be used depends on the type of calculation to be fulfilled. Whenever only $J = 0$ states were to be calculated and seniority information was important, as happens in Chapter 4 NATHAN has been used; in the cases when full spectra with the corresponding rotational bands were required, as is the case of Chapter 3, the choice was ANTOINE.

Chapter 3

Study of the Shape Coexistence in the nucleus ^{40}Ca

3.1 Introduction

^{40}Ca is a textbook example of doubly magic nucleus, corresponding to nucleons and protons filling the three lowest harmonic oscillator shells with $p = 0,1,2$, as can be seen in Figure 2.1. The $N = Z = 20$ shell gap, defined as:

$$\begin{aligned} zgap &= 2BE(N,Z) - BE(N,Z-1) - BE(N,Z+1) \\ ngap &= 2BE(N,Z) - BE(N-1,Z) - BE(N+1,Z), \end{aligned} \tag{3.1}$$

is about 7 MeV for both neutrons and protons, so that in a naive SM view the first excited states would be odd parity states at this energy, while the first positive parity states would appear around 14 MeV.

However, the first excited state of ^{40}Ca happens to be a 0^+ state at 3.35 MeV. Moreover, it turns out to be the head of a rotational band. Excited deformed bands in spherical nuclei like this one provide a spectacular example of shape coexistence of very different structures at the same energy scale, a rather peculiar aspect of nuclei. In the case of ^{40}Ca it is magnified by the existence of another deformed band, in this case of superdeformed character —this is, bearing an axis ratio in the intrinsic state close to 2:1— with its bandhead at 5.21 MeV. This state is the

third even parity state of the nucleus. The simultaneous explanation of the coexistence or these three different structures at low energy and the understanding of the mixing mechanism among themselves while preserving their identity constitutes a challenge for the ISM.

3.1.1 Collective behaviour in nuclei

Indeed, the very explanation, within the ISM, of a typical collective behaviour such as rotational motion —this is, deformation— may seem surprising. If we look back at the origins of nuclear structure, phenomena such as deformation, vibrations and their interplay where very well described and explained by the Collective Model proposed by Bohr and Mottelson [91, 92]. This model places emphasis on the collective degrees of freedom of nuclei rather than in their single particle behaviour.

In fact, the Collective model is in a sense heir to one of the the very first nuclear models, the Liquid Drop model for the nuclear masses [93, 94], in the sense that it considers nuclei as composed objects without taking care of the nucleonic degrees of freedom explicitly —as the microscopic models do. Indeed, a Liquid Drop model for vibrations and rotations, based on the idea of a moving nuclear surface, can be proposed [95].

The reconciliation of the Collective Model with the idea of a Mean Field came with the work of Nilsson, who was able to describe intrinsic states based upon single particle determinants within a deformed potential [96]. Hence, the collective coordinates describe the motion of the deformed state and the remaining internal motion is given by the single particle motion within the Mean Field —in this case, a quadrupole deformed potential.

In general, in this framework the nuclear wave functions are assumed to be separable into low frequency collective and high frequency intrinsic variables. The latter are referred to the body-fixed collective frame. The high frequency intrinsic problem can be solved —its solution will in general depend on the collective variables as parameters— and then the corresponding energy will be considered as an additional potential energy affecting the collective motion. Typically the energy difference between intrinsic levels is large compared to the spacing of the collective ones, and both modes do not interfere.

Since a quadrupole term is introduced in the Mean Field, the spherical symmetry of the Hamiltonian is broken. Therefore, the corresponding states do not have well defined angular momentum. Obviously, for actual states angular momentum is required to be a good quantum number. It is recovered when the rotation of the body-fixed frame is taken into account, by means of projection techniques [97].

In addition, pairing can also be introduced in this picture [98]. The whole framework is called the unified model, since it contains both single particle — Mean Field— and collective features.

This model sets the definition of a collective rotational band that we use for our analysis. According to it, a nucleus is a good rotor when we can find a rotational band showing the following properties:

1. The energy spectrum has the form:

$$E_J \propto J\left(J+1\right), \tag{3.2}$$

   where the proportionality factor is $\frac{1}{2I}$, with I the moment of inertia of the nucleus.

2. There is a common intrinsic quadrupole moment Q_0 throughout the band. Its value is common both in the static and dynamic cases. The former is obtained from the spectroscopic quadrupole moment while the latter comes from the $B(E2)$ electromagnetic transitions. Specifically, they read:

$$Q_0\left(s\right) = \frac{\left(J+1\right)\left(2J+3\right)}{3K^2-J\left(J+1\right)}Q_{spec}\left(J\right), \qquad K\neq 1, \tag{3.3}$$

$$Q_0\left(t\right)^2 = \frac{16\pi}{5\left|\left\langle JK20\left|J-2K\right\rangle\right|^2}B\left(E2,,J\rightarrow J-2\right), K\neq\frac{1}{2},1. \tag{3.4}$$

3.1.2 Collective behaviour within the ISM

The ISM gives results directly in the laboratory frame, hence it is not capable of describing the intrinsic deformed nuclear states. On the contrary, it gives information of associated quantities, namely the electromagnetic transitions and the

spectroscopic quadrupole moments, which are related to the intrinsic quantities by Eqs. (3.3) and (3.4). Indeed, these are the experimentally accessible quantities. Consequently, the explanation the ISM gives of collective behaviour such as rotations is of quite different nature than that of the unified model.

In particular, the microscopic foundations of rotational motion are based on the symmetries of the Mean Field as was pointed out by Elliott [99, 100]. In this work, Elliott showed that, given the underlying SU(3) symmetry of the harmonic oscillator, the eigenstates of the problem could be grouped according to the irreducible representation (irrep) of SU(3) they belong. All states in the same irrep are degenerated in energy. When a quadrupole–quadrupole interaction is added to this picture, the previously exact symmetry becomes dynamic, meaning that the degeneracy within irreps is broken while the independence between different irreps is preserved. The form of the spectra for a given irrep turns out to be of the form:

$$E_L \propto L\,(L+1)\,, \tag{3.5}$$

which reminds to Eq. (3.2). Since the transitions within irreps are expected to be large while those to different irreps will vanish, one can identify them with rotational bands.

The drawback of the model is that it is based on the SU(3) symmetry of the harmonic oscillator Hamiltonian which according to Figure 2.1 is known not to be preserved whenever the spin-orbit interaction is relevant. This limited the applications of the model to light nuclei in the *sd* shell such as ^{20}Ne or ^{24}Mg. These nuclei only require irreps with maximal spatial symmetry and hence $S = 0$, and accordingly the spin-orbit coupling does not play a role.

Therefore, a different scheme is required for heavier nuclei. In our case, we will study two different variations of the Elliott model, namely the pseudo-SU(3) [101, 102] and the quasi-SU(3) [103, 42] models.

The pseudo-SU(3) scheme is based on the fact that the spin-orbit coupling, mostly affecting to the orbit with $j = l + 1/2$ in a certain shell p, lowers its energy to the point that it lies out of the major shell. Then, the remaining orbits can be approximated to become a pseudo $p-1$ shell. The quasi-SU(3) model takes into account the $j = l + 1/2$ orbit when it comes close to those belonging to the $p-1$

shell. In this case, a quasi *p* shell is formed. Further details on these algebraic models that sustain the origin of collectivity in the ISM are left to Appendix A.

Previous ISM works have studied the collective behaviour of nuclei within the ISM framework. For instance, the rotor behaviour of ^{48}Cr [41] and the related particle plus rotor mirror nuclei ^{47}V–^{47}Cr and ^{49}V–^{49}Mn [42]. This kind of structures were typical in heavy nuclei, but its discovery and explanation in such light nuclei is relatively recent.

3.2 Previous works on shape coexistence and ^{40}Ca

Other cases of shape coexistence in spherical nuclei have been known for a long time. For instance, the four particle-four holes and eight particle-eight holes states in ^{16}O, starting at 6.05 MeV and 16.75 MeV of excitation energy [104, 105]. The theoretical descriptions based in multiple particle-hole excitations that can accommodate deformation already started in the 1960's with the works of Brown and Green [106] and Zuker, Buck and McGrory [39].

In ^{40}Ca, there has been since long experimental indications showing that the two low-lying sequences, 0^+, 2^+, 4^+, starting at 3.35 MeV and 5.21 MeV, may correspond to deformed or superdeformed bands [107]. However, it is only in the last decade that such bands, deformed and superdeformed, have been explored up to high spin in several medium-light nuclei such as ^{56}Ni [108], ^{36}Ar [109] and of course ^{40}Ca [110]. This issue has been accomplished thanks to the availability of large arrays of γ detectors like Euroball —in Europe— and specially Gammasphere —in the US.

One characteristic feature of these bands is that they may belong to rather well defined shell model configurations; for instance, the deformed excited band in ^{56}Ni can be associated with the configuration $\left(0f_{7/2}\right)^{12}\left(1p_{3/2}, 0f_{5/2}, 1p_{1/2}\right)^{4}$ while the superdeformed band in ^{36}Ar is based in the structure $(sd)^{16}(pf)^{4}$.

The location of the *n*p-*n*h states in ^{40}Ca was first studied in Ref. [111]. After it, the theoretical works by Gerace and Green [112, 113], similar to those mentioned above for ^{16}O, already assigned a 4p-4h and 8p-8h character for these bands. Their triaxial normal deformed and superdeformed natures, respectively, were predicted. A modern calculation of the position of the *n*p-*n*h states was performed

in Ref. [114], within the Hartree-Fock approximation with blocked particles and Skyrme forces.

While many approaches are available for the microscopic description of these bands —Projected Shell Model [115], cranked Nilsson-Strutinski [109], cranked Skyrme Hartree-Fock [116], Skyrme Hartree-Fock plus BCS with configuration mixing [117], Angular Momentum Projected Gogny HFB plus Generator Coordinate Method [118], Relativistic Mean Field [119], Alpha Cluster Model [120], Antisymmetrized Molecular Dynamics model [121, 122] or cranked triaxial HFB [123]— the ISM is, when affordable, a prime choice. The problems come, as stated in Chapter 2, from the size of the valence spaces needed to accommodate the *n*p-*n*h configurations.

In the case of ^{36}Ar, it was shown that ISM calculations within a valence space consisting on the *sd* and pf shells can describe the coexistence of the spherical ground state and the superdeformed band, both the very existence of the spherical and the superdeformed states forming a band and the configuration mixing that permits transitions connecting them [44].

A similar explanation is required for ^{40}Ca, with the additional difficulty that, in this case, three intrinsic states are at play, the spherical ground state, a first excited deformed state and finally a superdeformed one. Previous ISM works pointed, with fixed *n*p-*n*h valence space calculations, to a $(sd)^{20}(pf)^4$ structure for the normal deformed band and a $(sd)^{16}(pf)^8$ structure for the superdeformed one [124, 125]. This is, the structure of the bands corresponds to the promotion of four and eight particles across the Fermi level, from the *sd* to the pf shell, that we call 4p-4h and 8p-8h configurations.

These configurations come also from a study of the underlying pseudo-SU(3) and quasi-SU(3) structures presented in the Introduction to this Chapter. For this nucleus, in the *sd* shell we have a pseudo-SU(3) scheme formed by the nearly degenerate $1s_{1/2}$ and $0d_{3/2}$ orbits, while in the pf the quasi scheme can be applied, mainly originated by the $\Delta j = 2$, $\Delta l = 2$ pair of orbits $0f_{7/2}$–$1p_{3/2}$. Within this models we can compute the intrinsic quadrupole moments associated to the different *n*p-*n*h deformed structures. Using the pseudo+quasi-SU(3) prescription we find $Q_0 = 125\ e\ \mathrm{fm}^2$ for the 4p-4h configuration and $Q_0 = 180\ e\ \mathrm{fm}^2$ for the 8p-8h. The deformation parameter for this values can be calculated through the relation:

$$\beta = \sqrt{\frac{\pi}{5}} \frac{Q_0}{Ze\left\langle r^2 \right\rangle_{ch}} \tag{3.6}$$

which gives values of $\beta = 0.39$ and $\beta = 0.56$ using the experimental rms radius $\left\langle r^2 \right\rangle_{ch}^{1/2}$ given in Ref. [126]. This is consistent with what one would expect for a deformed and a superdeformed band. Then, superdeformation in this region of nuclei can be achieved readily in the space of two major oscillator shells, provided that SU(3)-like geometries of the spherical mean field are at hand. The SU(3) limit gives $Q_0 = 148\ e\ \mathrm{fm}^2$ and $Q_0 = 226\ e\ \mathrm{fm}^2$ instead. As the quadrupole correlation energy should vary as the square of the quadrupole moment, the pseudo+quasi-SU(3) correlation energy can be estimated to represent about two thirds of the SU(3) limit.

However, this description is too crude, because the physical states contain components of different *n*p-*n*h rank. The mixing should allow for transitions connecting the superdeformed and normal deformed bands as well as both bands with the spherical ground state, while remaining gentle enough not to jeopardize the very existence of the bands.

To obtain such explanation of the coexistence of the different states and their mixing has been the aim of the work presented in this Chapter. Most of it has already been published in Refs. [127, 128].

3.3 Valence space and effective interaction

As has been explained above, an adequate valence space for the study of the coexisting bands in ^{40}Ca consists of the *sd* and *pf* major oscillator shells. Its only drawback is that the dimensions involved —10^{12} in the m-scheme— are beyond our present computing capability. A possible way out is to close the $d_{5/2}$ orbit, that is, to work with a virtual ^{28}Si inert core. The quadrupole collectivity of the solutions will be reduced by this truncation, but it was checked in ^{36}Ar that the effect is moderate [44]. As a bonus, this truncation reduces drastically the spurious center of mass components of the wave functions that can therefore be controlled perturbatively. The origin of this spurious mode can be found in Appendix B. Hence, the chosen valence space will encompass the $1s_{1/2}$, $0d_{3/2}$, $0f_{7/2}$, $1p_{3/2}$, $0f_{5/2}$ and

$1p_{1/2}$ orbits, leading to maximum basis sizes of $\sim 10^9$. We call this valence space r_2pf. In a harmonic oscillator major shell p, r_p will represent all the orbits except the one with the largest $j = p + \frac{1}{2}$.

For this valence space the effective interaction SDPF.SM will be used, described in detail in Ref. [88]. In addition, to reduce the effects of the mixing with states with spurious centre of mass excitations, the center of mass Hamiltonian, $\lambda_{cm}H_{cm}$, will be added to the interaction, with $\lambda_{cm} = 0.5$, following the approach explained in detail in Appendix B. The effect of this correction is small, since the blocking of the $d_{5/2}$ orbit reduces greatly the centre of mass contamination.

An unwelcome consequence of the blocking is that it does not affect equally to the different np-nh configurations. Indeed, it has no influence ion the closed shell and becomes maximal for the 12p-12h excitations. Following Ref. [44] the losses of correlation energy are compensated with an attractive monopole term parabolic in n. It is adjusted so as to locate the two excited 0^+ states close to their experimental values. This issue will be discussed in more detail in section 3.5, along with the presentation of the results of the fully mixed calculations.

3.4 Results of the calculations at fixed $n\hbar\omega$

With the effective interaction and the valence space ready, the first step will be to make calculations at fixed $n\hbar\omega$. The aim is to verify that expectations based in previous experiences and in algebraic models are fulfilled.

In Figure 3.1 the results of the fixed $8\hbar\omega$ calculation are compared with the experimental superdeformed (SD) band from Ref. [110] in a backbending plot. The accord is excellent, only the slight change of slope at $J = 10$ is not reproduced by the calculation. Notice that the band is very regular, showing no backbending up to $J = 24$, contrary to the situation in other deformed nuclei such as ^{48}Cr or ^{36}Ar. This delay in the alignment regime is surely due to the extra collectivity induced by the presence of eight particles in quasi-SU(3) orbitals —four in ^{36}Ar— and four particles in pseudo-SU(3) orbitals, absent in ^{48}Cr. The tiny backbending at $J = 20$ produced by the truncated calculation of Ref. [125], disappears when the unrestricted r_2pf valence space is employed. The rather impressive agreement of the energetics of the superdeformed band with the calculation at fixed $8\hbar\omega$ suggests

Figure 3.1: Superdeformed band in ^{40}Ca. E_γ's, experimental data *vs* fixed $8\hbar\omega$ theoretical calculation.

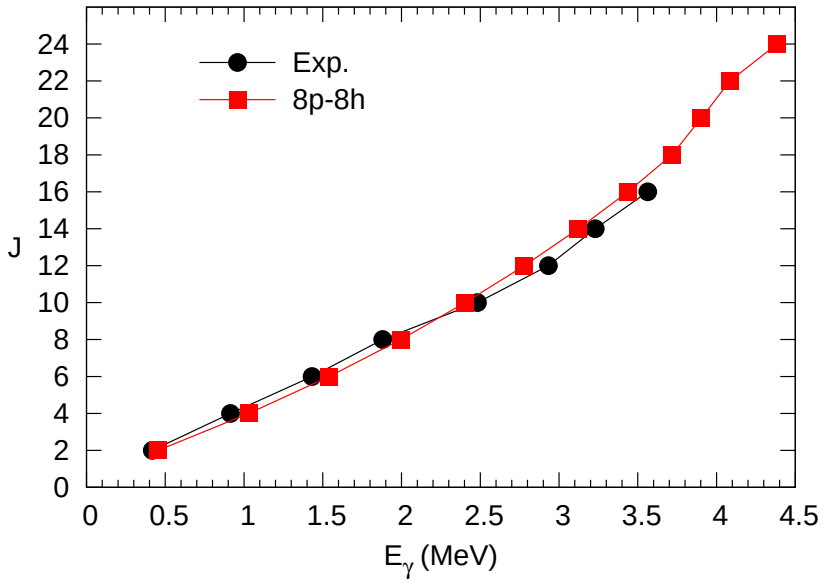

that the SD band is certainly of rather pure 8p-8h character.

The quadrupole properties of the superdeformed band are collected in Table 3.1. The $B(E2)$'s and the spectroscopic quadrupole moments Q_{spec} have been computed using the conventional effective charges $\delta q_\pi = \delta q_\nu = 0.5$ and the oscillator parameter is taken $b = 1.974$ fm, obtained from the experimental charge radius. Then, the intrinsic static and transition quadrupole moments $Q_0(s)$ and $Q_0(t)$, have been extracted, assuming $K = 0$, through Eqs. (3.3) and (3.4).

The value of the intrinsic quadrupole moment roughly corresponds to a deformation parameter $\beta = 0.6$, which is characteristic of a superdeformed shape and agrees with the experimental value of Ref. [110] —a comparison with a subsequent analysis of the same experiment [130] will be made below. In Figure 3.2 we have plotted the calculated and experimental results; they agree within the large experimental error bars. Notice that as J grows, the theoretical results lose some collectivity, whereas the experimental fit to the Doppler Shift Attenuation data is

Table 3.1: Quadrupole properties —in e fm^2 and e^2 fm^4— of the superdeformed band in ^{40}Ca for a fixed 8p-8h configuration calculation.

J	$Q_{spectroscopic}$	$B(E2)_{J\to J-2}$	$Q_0(s)$	$Q_0(t)$
2	-51.4	643	180	180
4	-64.6	905	178	178
6	-68.4	968	171	176
8	-69.6	980	165	173
10	-69.9	953	161	168
12	-70.5	896	159	162
14	-72.0	804	159	152
16	-72.5	696	159	141

compatible with a constant transition quadrupole moment. The experimental point corresponding to the $4^+ \to 2^+$ transition comes from an earlier measurement of the lifetime of the 4^+ state and its in-band branching ratio [129].

A fixed 4p-4h calculation was performed as well in order to describe the normal deformed bands in ^{40}Ca. The most salient aspect of the calculated results is the triaxial character of the solution, with a well developed band based in the second 2^+ state —2^+_γ— in addition to the band based on the first 0^+ —all states referred to the 4p-4h configuration. These bands will be named *gamma* band and normal deformed (ND) band, respectively. They are assigned the quantum numbers $K = 0$ and $K = 2$. Of course, the two bands are of normal deformed nature since both stem from the same intrinsic state.

The results for the ND band are compared to the experimental ones from Ref. [110] —band 2— in Figure 3.3. The agreement is now much worse than that for the SD band, although the main trends are already present in the calculation. At $J = 12$ the experimental band up-bends while the calculation produces a strong backbending.

Figure 3.2: Superdeformed band in ^{40}Ca. Transition quadrupole moments $Q_0(t)$; experimental data from Ref. [129] (lozenges) and from Ref. [110] (circles) *vs* the theoretical results of the fixed 8p-8h calculation (squares).

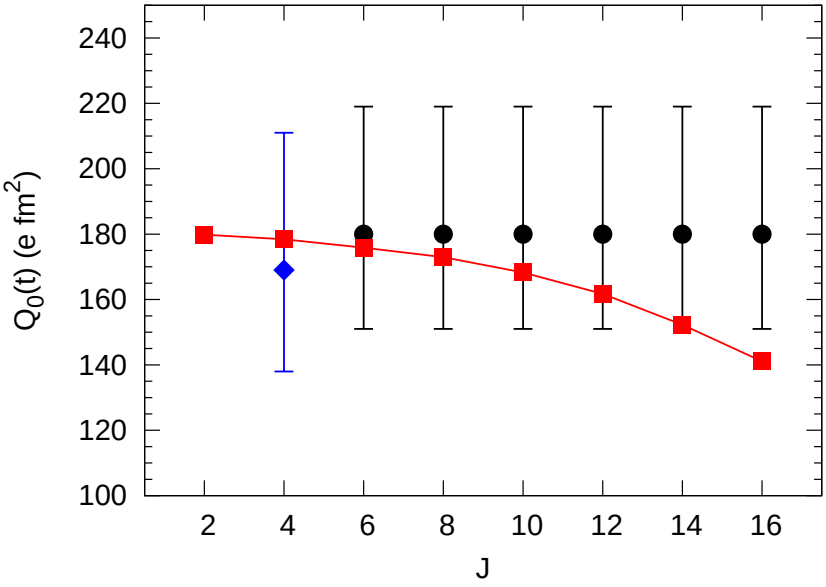

The 2^+ bandhead of the γ band is located 2.05 MeV above the 0^+ bandhead of the ND band. Experimentally the splitting is 1.90 MeV. The transition energies inside the γ-band are compared to the experimental ones —Ref. [110], band 4— in Table 3.2. The calculated values compare reasonably well with the experiment, except for the location of the 13^+ state that appears 1 MeV too low.

The quadrupole properties of the ND band are shown in Table 3.3. In this case, the corresponding deformation parameter is $\beta = 0.3$, a typical value for a normal deformed band. The comparison with the experimental data is postponed until the discussion of the complete calculation, which in this case do not make much difference with respect to the fixed $4\hbar\omega$ calculation.

In summary, ISM calculations in the r_2pf valence space at fixed 8p-8h and 4p-4h configurations give a convincing description of the SD band in ^{40}Ca, and are also able to describe the corresponding ND rotational spectra, which turns out

Figure 3.3: Normal deformed $K = 0$ band in ^{40}Ca. E_γ's, experimental data *vs* fixed $4\hbar\omega$ theoretical results.

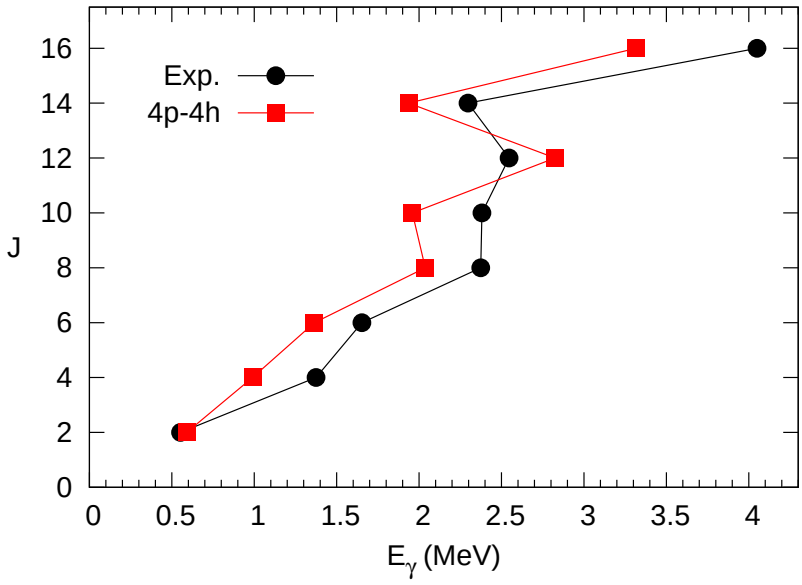

to be that of a triaxial structure developing a $K = 0$ and a $K = 2$ —γ— band, in agreement with the experimental information. Indeed, in the physical states the configurations with different values of $n\hbar\omega$ mix, mainly through the cross shell pairing interactions, and it will be the task of the next sections to understand how this mixing proceeds and to compare the complete results with the experimental data.

3.5 Energies of the $n\hbar\omega$ bandheads relative to the closed shell

Before moving into the full r_2pf space diagonalizations, the information gathered in the fixed $n\hbar\omega$ calculations needs to be explored in more depth. With the SDPF.SM interaction, the $n\hbar\omega$ bandheads lie too high in energy relative to the closed shell. A small part of this missing energy can be due to residual defects of

Table 3.2: Experimental and theoretical energies (in keV) for the deformed γ band in ^{40}Ca. The thoretical results obtained in a fixed 4ħω calculation.

Transition	E_γ(4p-4h)	E_γ(Experiment)
$3^+_\gamma \rightarrow 2^+_\gamma$	819	781
$4^+_\gamma \rightarrow 2^+_\gamma$	1244	1260
$5^+_\gamma \rightarrow 3^+_\gamma$	1187	1369
$7^+_\gamma \rightarrow 5^+_\gamma$	1501	1538
$9^+_\gamma \rightarrow 7^+_\gamma$	2346	2773
$11^+_\gamma \rightarrow 9^+_\gamma$	1518	1827
$13^+_\gamma \rightarrow 11^+_\gamma$	1943	3044

Table 3.3: Quadrupole properties —in e fm^2 and e^2 fm^4— of the $K = 0$ normal deformed band of ^{40}Ca. Fixed 4ħω calculation.

J	$Q_{spectroscopic}$	$B(E2)_{J\rightarrow J-2}$	$Q_0(s)$	$Q_0(t)$
2	-31.0	269	109	116
4	-41.0	364	113	113
6	-48.9	341	120	104
8	-44.0	309	104	97
10	-48.9	237	113	84
12	-38.3	86	86	50
14	-40.9	115	91	58
16	-34.8	47	76	37

the cross-shell monopole terms of the interaction, but the bulk of it is due to the blocking of the $0d_{5/2}$ orbit. This effect can be absorbed via the modification of two global monopole terms:

$$\Delta(n) = \frac{1}{2}n(n-1)\delta_1 + n(12-n)\delta_2, \tag{3.7}$$

where n is the number of particles in the pf-shell, and the δ's are the modifications of the global pf-shell monopole interaction and the r_2–pf monopole interaction, respectively. In a first set of exploratory calculations, it was realized that when the δ's were chosen so as to locate the two excited 0^+ states at about their experimental excitation energies, the percentage of closed shell in the ground state of ^{40}Ca was too low (54%), i.e. the mixing was too strong. In order to diminish this mixing all the cross shell off-diagonal matrix elements were multiplied by a factor 0.8. Now, the values of the δ's that place the 0^+ states correctly are $\delta_1 = -0.27$ MeV and $\delta_2 = -0.13$ MeV. With this choice the closed shell component of the ground state rises to 65%, that can be taken as a reasonable value. A different set of δ's can be used, giving 75% of closed shell, and no dramatic changes are observed in the ensemble of observables. As the 0.8 scaling implies a reduction of the pairing interactions in the space, the isovector pairing matrix elements of the pf-shell part of the SDPF.SM interaction are taken now as 0.8 times the original values. In summary, two global monopoles of the interaction have been loosely fitted to the location of the excited 0^+ states, keeping the core excited components in the 30% range. Actually, the difference in correlation energy between a full sd-shell calculation for the nucleus $N = Z = 20 - \frac{n}{2}$, and the calculation with the orbit $0d_{5/2}$ blocked, accounts for two thirds of the value of $\Delta(n)$. The pairing modifications can be justified with perturbation theory arguments [44]

The energies of the different multiparticle-hole configurations are plotted in Figure 3.4. The squares give the lowest uncorrelated energy in each $n\hbar\omega$ space —to be more precise, the minimum of the expectation value of the SDPF.SM Hamiltonian plus the correction of equation (3.7), calculated for all the Slater Determinants of the m-scheme spherical basis. As anticipated, the uncorrelated excitation energies do not grow linearly with the number of particles excited across the $N = Z = 20$ gap —if it had been so, all the squares would lie in the prolongation of the straight

Figure 3.4: Energies of the lowest states in the different *n*p-*n*h configurations of ^{40}Ca. Lowest Slater Determinant plus the correction of equation (3.7) (squares); Energy of the lowest 0^+ state in the r_2pf space at fixed $n\hbar\omega$ (circles). The lozenges give the energies of the three lowest 0^+'s coming out of the fully mixed calculation in the r_2pf space. The latter are placed in the figure according to their dominant configuration.

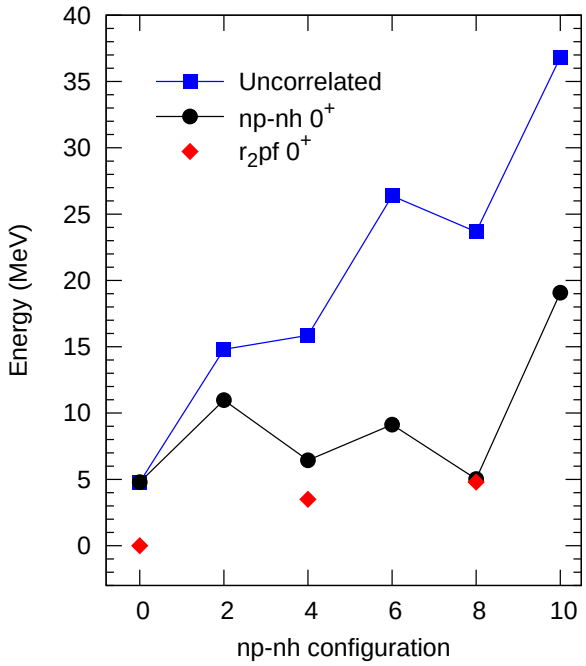

line joining the $n = 0$ and $n = 2$ points. The increase is much slower, with a superimposed odd-even effect in $n/2$. Notice that the energy of the lowest $8\hbar\omega$ Slater Determinant lies ≈ 20 MeV above the closed shell. Finally, explicit diagonalizations are carried out separately for each $n\hbar\omega$. The results plotted as circles. It can be seen that the correlation energies are very large, in particular for the SD bandhead that gains 18.5 MeV and becomes almost degenerated with the closed shell configuration.

A rough analysis of the correlation energies can be performed, in terms of their $T = 0$ and $T = 1$ pairing and multipole-multipole —mainly quadrupole-quadrupole— content. For that, the expectation value of the —monopole free—

Figure 3.5: Energies of the yrast states of ^{40}Ca in the different fixed *n*p-*n*h configurations for even J, from $J = 0$ up to $J = 16$. For $J = 0$, they correspond to the circles in Figure 3.4.

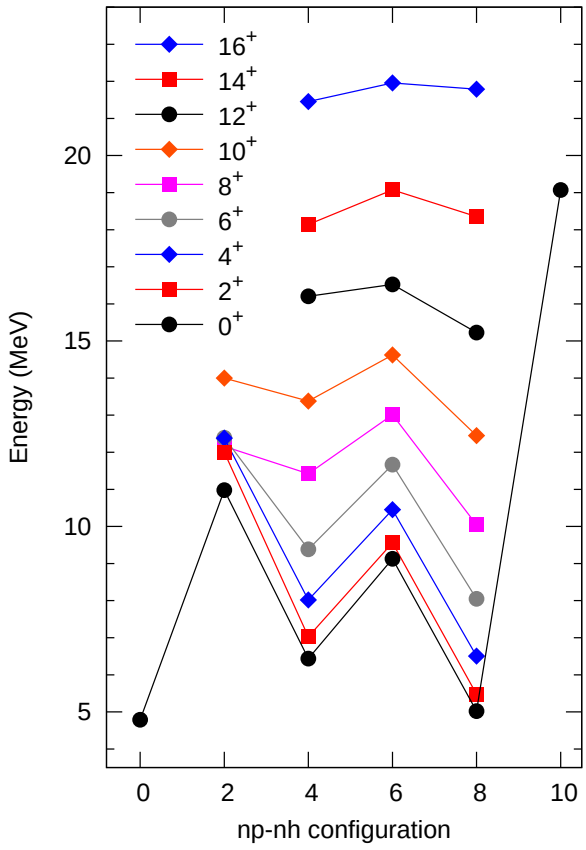

pairing part of the effective interaction is computed in the fixed $n\hbar\omega$ bandheads and subtracted from the total correlation energy. In the $4\hbar\omega$ 0^+ ND state, out of the 9.5 MeV of correlation energy, 5.5 MeV come from $T = 1$ pairing, 0.5 MeV from $T = 0$ pairing and 3.5 MeV from the quadrupole correlations. In the $8\hbar\omega$ 0^+ SD state, the share is 5.5 MeV, 0.5 MeV and 12.5 MeV respectively. Thus, the contribution of the neutron-proton pairing amounts to 2.33 MeV for any of the bands.

The structure of the line joining the black circles in the plot is quite interesting,

because it resembles the energy versus deformation curves typical of constrained Hartree-Fock calculations. The number of particle-hole excitations in the X-axis can be taken as roughly proportional to the deformation. With this perspective, we distinguish three coexisting minima, spherical, $n = 0$, deformed, $n = 4$, and superdeformed, $n = 8$, separated by the $n = 2$ and $n = 6$ maxima. The $n = 10$ bandhead lies very high in energy and it has been verified to play no role at all in this problem. The structure of this "potential energy" curve, consisting of wells and barriers, provides an intuitive picture of how the deformed and superdeformed bands can preserve their identity after mixing.

Keeping on with the Mean Field analogy, it is worth to note that the black circles in Figure 3.4 correspond to $J = 0^+$ states, i.e. they are angular momentum projected solutions —before variation, VAP in the usual jargon. In Figure 3.5 we add the points for all the lowest states of even J that appear in the deformed —$4\hbar\omega$ and $6\hbar\omega$— and superdeformed —$8\hbar\omega$— bands and the corresponding $2\hbar\omega$ and $10\hbar\omega$ states. We can observe that the structure of wells and barriers of the $J = 0$ curve, that protects the deformed and superdeformed bands from strong mixing, is maintained up to $J = 10$. Above, the barriers flatten and we should expect larger mixing. In particular this can lead to the erosion of the collectivity of the SD band at high spin in the theoretical calculation.

3.6 Results of the complete calculations in the r_2pf space

The calculations in the r_2pf space are computationally very demanding. In addition to the very large dimensions involved, the need to compute several states of the same angular momentum increases substantially the number of Lanczos iterations needed to achieve convergence. Hence, as advanced in Chapter 2, the ISM code ANTOINE has been used throughout.

The structure of the first three 0^+ states, the spherical ground state and the excited deformed and superdeformed bandheads is shown in Table 3.4. The two body cross-shell off diagonal matrix elements can connect directly configurations differing only in two particle hole jumps. In can be seen in the Table that, indeed, the ground state 0p-0h leading component is mainly correlated by 2p-2h components. As for the leading 4p-4h component of the normal deformed state it can, in princi-

Table 3.4: Percentage of *n*p-*n*h components and energy of the first three 0^+states —ground state, normal deformed and superdeformed bandheads— of ^{40}Ca. Full r_2pf calculation.

	0p-0h	2p-2h	4p-4h	6p-6h	8p-8h	E(th)	E(exp)
0^+_{GS}	65	29	5	-	-	0	0
0^+_{ND}	1	1	64	25	9	3.49	3.35
0^+_{SD}	-	-	9	4	87	4.80	5.21

ple, mix with 2p-2h and 6p-6h components. Actually the mixing is dominated by the latter, with a non-negligible 8p-8h piece. The leading 8p-8h component of the SD could also mix with 6p-6h and 10p-10h configurations directly, but it chooses none. The SD bandhead is very pure, with only small amounts of 4p-4h and 6p-6h components. Let us mention that the yrast band in the $6\hbar\omega$ space corresponds also to a rotor with deformation slightly larger than the one in the $4\hbar\omega$ space. On the contrary, the deformation and the correlation energy in the $10\hbar\omega$ space are smaller, leading to negligible mixing with the other spaces.

In the process of mixing the winner is, energy wise, the ground state that gains almost 5 MeV, mostly pairing-like. The ND band gains barely 2 MeV and the SD band essentially nothing. That's why, in order to reproduce the experimental situation, the three 0^+ states before mixing must be degenerated or even with their energies inverted. The energies of the three physical 0^+ states after mixing are represented by the lozenges in Figure 3.4.

3.6.1 The superdeformed band

In first place, we discuss the results of the excitation energies of the SD band as produced by the fully mixed calculation. As can be seen in Figure 3.6, the mixing does not modify noticeably the features already present in the fixed 8p-8h calculation. Perhaps some irregularities at the upper part of the band could be detected. The calculated sequence crosses the experimental one at around the rotational fre-

Figure 3.6: E_γ's in the superdeformed band in ^{40}Ca. Experimental data *vs* full r_2pf theoretical calculation.

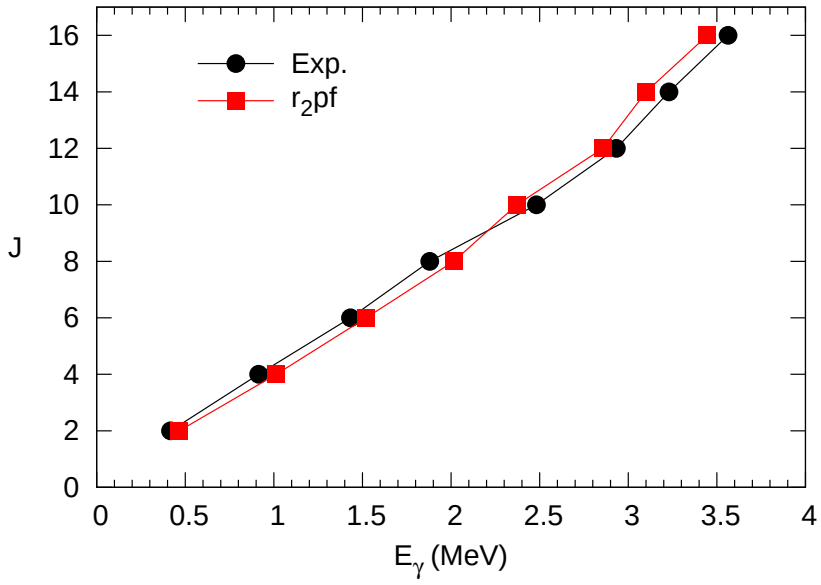

quency where the calculated states start loosing collectivity, but in global terms, the agreement is excellent. The results of the mixed calculation beyond $J = 16$ are equivalent to that of the fixed $8\hbar\omega$ calculation shown in Figure 3.1.

In Table 3.5, the *n*p-*n*h structure of the SD band is given up to $J = 16$. The 8p-8h component is nicely constant up to $J = 10$, as was foreseen from the analysis of the potential energy curves in Figure 3.5. At higher angular momentum, the mixing with $6\hbar\omega$ components becomes stronger, and a less collective behaviour should be expected. It is interesting to follow the evolution of the location of the SD states with increasing angular momentum. The $J = 0$ SD state is the third $J = 0$ state in the spectrum. The $J = 2$, 4, and 6 states are the second of their spins, $J = 8$ and 10, third, $J = 12$, fourth, $J = 14$ sixth, and finally $J = 16$ fourth again.

Now let's examine the quadrupole properties of the superdeformed band in ^{40}Ca as they come out of the full r_2pf calculation. The theoretical spectroscopic quadrupole moments and the $B(E2)$ values are gathered in Table 3.6. The conclu-

Table 3.5: Percentage of *n*p-*n*h components of the superdeformed band of ^{40}Ca. Full r_2pf calculation.

J	0p-0h	2p-2h	4p-4h	6p-6h	8p-8h
0	-	-	9	4	87
2	-	-	11	4	85
4	-	-	8	5	87
6	-	-	3	5	91
8	-	-	2	6	91
10	-	-	1	12	87
12	-	-	2	29	69
14	-	-	11	27	63
16	-	-	0	40	60

sion is that, up to $J = 10 - 12$, the mixing causes just an erosion of the $8\hbar\omega$ values presented in Table 3.1. Beyond, the larger presence of less collective $6\hbar\omega$ components has a much stronger effect, particularly in the $B(E2)$'s. Thus, the values of the transition quadrupole moments diminish rapidly at the end of the band. The static quadrupole moments vary less abruptly.

In Figure 3.7 the theoretical predictions are plotted against the experimental results. Comparing with the fixed $8\hbar\omega$ results, a large reduction of the transition quadrupole moments of the three upper transitions of the band is found. This drop in collectivity could be an artifact of the r_2pf space, but for the moment there is no way to verify it.

The experimental points in the Figure for $J \geq 6$ are those of the first analysis of the Doppler Shift Attenuation data made in Ref. [110]. The $J = 4$ point comes from another, earlier, experiment [129]. The calculated transition quadrupole moments agree with the data for $J \leq 10$, but underestimate them for the three uppermost transitions. In Ref. [130] a reanalysis of the same experimental data was made,

Table 3.6: Quadrupole properties —in e fm^2 and e^{2}fm^4— of the superdeformed band in ^{40}Ca. Full r_2pf calculation.

J	$Q_{spectroscopic}$	$B(E2)_{J\to J-2}$	$Q_0(s)$	$Q_0(t)$
2	-47.7	579	167	171
4	-61.1	813	168	169
6	-66.3	874	166	167
8	-66.5	906	158	166
10	-66.3	844	153	158
12	-71.8	546	162	126
14	-62.1	557	139	127
16	-64.9	429	142	111

and the preferred solution differs from the precedent one. Whereas the former solution was a constant $Q_0(t) = 180^{+0.39}_{-0.29}$ e fm^2 for the six transitions from the states of the SD band with $J = 16$ to $J = 6$, the latter gives $Q_0(t) = 181^{+0.41}_{-0.26} \pm 0.21$ e fm^2 for the $J = 16$ to $J = 12$ states and $Q_0(t) = 118^{+0.06}_{-0.05} \pm 0.13$ e fm^2 for $J = 10$ to $J = 6$. Notice that, compared to Ref. [110] an extra systematic error has been added. In spite of that, the final error bars of the values corresponding to the lower J transitions are largely reduced with respect to those of the upper transitions. Actually, their extracted $Q_0(t)$ values are barely compatible with the value for the $4^+ \to 2^+$ 914 keV transition, $Q_0(t) = 169^{+0.42}_{-0.32}$ e fm^2, obtained in Ref. [129] —the lower and upper tips of one and another error bars just touch at the value 137 e fm^2.

If the results of the analysis of Chiara *et al.* were the only viable interpretation of the data, the comparison with our calculated $Q_0(t)$'s would be rather poor, meaning that something important in missing in our approach. The beautiful agreement we had for $J \leq 10$ will be lost, and the fact that the increase of the experimental error bars for the upper transitions make our results deviate less, is a meager compensation. Different solutions with larger mixing have been tested, through the

Figure 3.7: Transition quadrupole moments in the superdeformed band of ^{40}Ca. Full r_2pf theoretical results (squares) compared to the experimental data from Refs. [129] (lozenges) and [110] (circles).

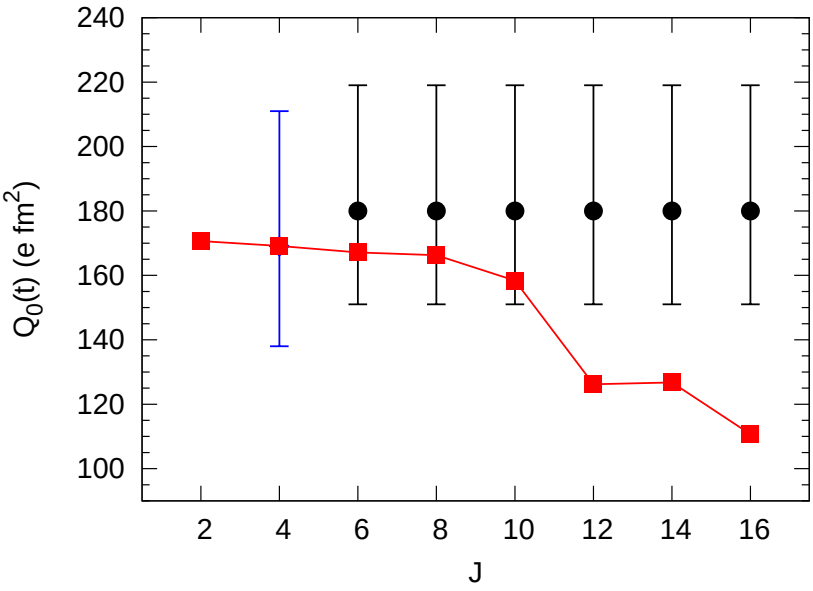

mechanisms discussed in section 3.5, but even going as far as keeping just 50% of closed shell in the ground state, only an extra 10% erosion of the $B(E2)$'s for $J \leq 10$ is obtained. On the contrary, more mixing brings in large reductions of the transitions in the upper part of the SD band. In Section 3.6.3, when dealing with the out-band decay branches a mechanism that conciliates the theoretical picture with the experimental data is proposed. It is based on a detailed analysis of the decay of the $J = 8$ member of the SD band, a decay that may have driven the fit of Ref. [130] into the new set of $Q_0(t)$'s.

3.6.2 The normal deformed triaxial bands

Now let's turn to the full r_2pf space results for the two bands that according to section 3.4 have a dominant 4p-4h structure. It was also shown that they are consistent with the presence of a deformed triaxial intrinsic state. In Table 3.7 we list

Table 3.7: Percentage of *n*p-*n*h components of the $K = 0$ normal deformed band of ^{40}Ca. Full r_2pf calculation.

J	0p-0h	2p-2h	4p-4h	6p-6h	8p-8h
0	1	1	64	25	9
2	-	1	64	24	10
4	-	1	68	23	8
6	-	2	75	20	3
8	-	21	62	15	2
10	-	-	81	17	1
12	-	-	81	18	1
14	-	-	82	17	1
16	-	-	79	19	1

the percentage of the different *n*p-*n*h components in the deformed band of ^{40}Ca based on the first excited 0^+ state. It can be observed that the 4p-4h dominance is less strong than the 8p-8h dominance in the SD band at low spins, and larger at high spins. Another characteristic feature is that the mixing proceeds through the 6p-6h components, with the 2p-2h components completely absent except in the $J = 8$ state, where an accidental degeneracy occurs. There is not a definite explanation for this preference, that can be due to phase space considerations —there are much more 6p-6h states to mix with than 2p-2h states— but more probably to the fact that the collectivity of the 4p-4h and 6p-6h spaces is very similar and much larger than that of the 2p-2h space. That the mixing strength of the 6p-6h space is exhausted by the ND band could explain why the SD band is so pure. As expected in a collective picture, the spread of the wave functions of the states of the γ band among the *n*p-*n*h spaces is very similar to that of the ND band.

The calculated energies of the ND band are plotted in Figure 3.8 compared with the experiment. It can be noticed that the mixing improves clearly the agreement in

Figure 3.8: Normal deformed $K = 0$ band in ^{40}Ca. E_γ's, experimental data *vs* full r_2pf theoretical calculation.

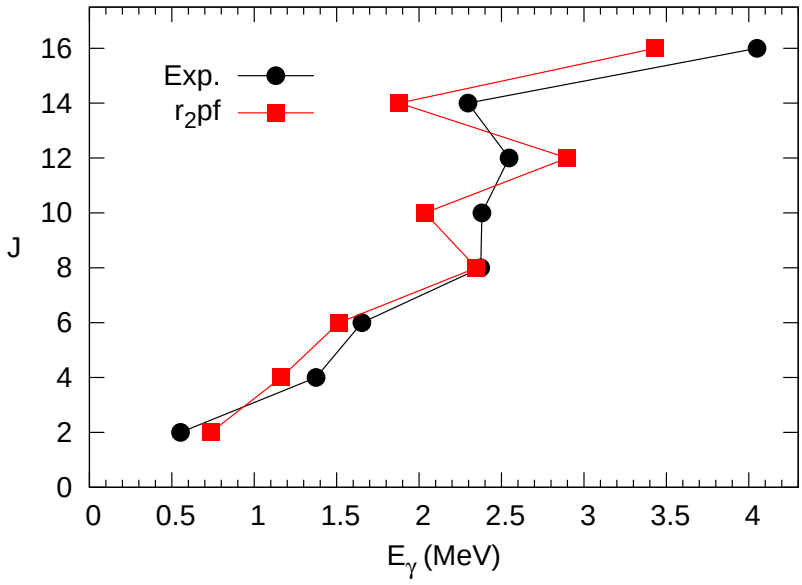

the lower part of the band. The discrepancy at the backbending is the same already present in the $4\hbar\omega$ calculation.

The 2^+ bandhead of the γ band is predicted to lie at 5.88 MeV of excitation energy compared with the experimental value 5.25 MeV. This means that the mixing increases the splitting of the ND and γ bands by 350 keV with respect to the result of the $4\hbar\omega$ calculation. The in-band excitation energies are shown in Table 3.8. They change very little with respect to the $4\hbar\omega$ values gathered in Table 3.2. The percentage of the different *n*p-*n*h components in this band can be seen in Table 3.9, and also shows very similar results to that of the ND deformed band —see Table 3.7.

The quadrupole properties of the ND band, shown in Table 3.10, are very similar to those of the $4\hbar\omega$ calculation. Only at $J = 8$ there is a reduction in collectivity due to the accidental mixing with a nearby 2p-2h state, that has already been commented above. As can be seen in Figure 3.9, where the transition quadrupole

Table 3.8: Experimental and theoretical energies (in keV) for the deformed γ band in ^{40}Ca. Full r_2pf calculation.

Transition	$E_\gamma(r_2pf)$	E_γ(Experiment)
$3^+_\gamma \rightarrow 2^+_\gamma$	720	781
$4^+_\gamma \rightarrow 2^+_\gamma$	1163	1260
$5^+_\gamma \rightarrow 3^+_\gamma$	1172	1369
$7^+_\gamma \rightarrow 5^+_\gamma$	1503	1538
$9^+_\gamma \rightarrow 7^+_\gamma$	2361	2773
$11^+_\gamma \rightarrow 9^+_\gamma$	1519	1827
$13^+_\gamma \rightarrow 11^+_\gamma$	1900	3044

Table 3.9: Percentage of *n*p-*n*h components of the deformed γ band of ^{40}Ca. Full r_2pf calculation.

J	0p-0h	2p-2h	4p-4h	6p-6h	8p-8h
2	-	1	69	24	5
3	-	1	77	22	-
4	-	1	78	21	-
5	-	1	79	20	-
7	-	10	74	17	-
9	-	-	83	17	-
11	-	-	84	16	-
13	-	-	84	16	-

Table 3.10: Quadrupole properties —in e fm^2 and e^2 fm^4— of the $K = 0$ normal deformed band in ^{40}Ca. Full r_2pf calculation.

J	$Q_{spec.}$	$B(E2)_{J\to J-2}$	$Q_0(s)$	$Q_0(t)$
2	-32.2	292	113	121
4	-42.1	397	116	118
6	-47.3	346	118	105
8	-35.5	227	84	83
10	-48.1	161	111	69
12	-37.6	75	85	47
14	-39.1	112	87	57
16	-35.6	49	78	37

moments are plotted, this reduction goes in the direction demanded by the data. Globally the agreement is quite good, the trends are very well reproduced and in most cases the theoretical numbers fall inside the experimental error bars. At the upper part of the band the theoretical values underestimate the experimental ones. The data come from different sources, for $J \geq 8$ they are taken from the Doppler Shift Attenuation analysis of Ref. [110], while for $J = 2$, $J = 4$, and $J = 8$ they come from the lifetimes and branching ratios measured in Refs. [129, 131].

In Table 3.11 the calculated quadrupole properties of the γ band are collected. The intrinsic information has been extracted from the $B(E2)$'s and spectroscopic quadrupole moments assuming $K = 2$. A well defined deformed intrinsic state is again found, with similar static and transition quadrupole moments, both very similar to those of the ND band.

3.6.3 Out-band transitions

The experimental data on out-band transitions are scarce and very often affected by large uncertainties. For the low energy part of the spectrum of ^{40}Ca, lifetimes

Figure 3.9: Transition quadrupole moments in the $K = 0$ normal deformed band in ^{40}Ca. Full r_2pf theoretical results (squares) compared to the experimental data from Refs. [131] (lozenges) and [110] (circles).

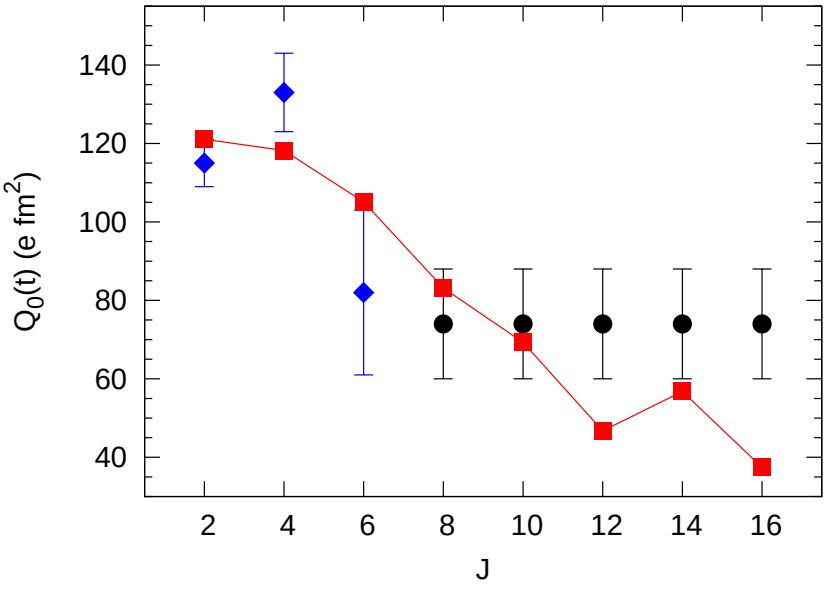

and branching ratios are known for some levels. For $J \geq 6$, the semi quantitative information of Refs. [110] and [130] will be taken as reference. In Table 3.12, the focus is set in the out-band transitions from ND and SD states. The balance is uneven. The transition probabilities of the decays from the 2^+ states in the ND and SD bands to the ground state are largely under-predicted by the calculation. If the mixing is increased, they rise at most by a factor two, very far from what would square with the data. For these small $B(E2)$'s it is possibly not sensible to reason in terms of factors, but instead think that some additive contribution is lacking in our space. It is worth to recall here that the span of $B(E2)$ values to be explained simultaneously is of three orders of magnitude. The decay of the superdeformed 0^+ is well reproduced, and the same applies to the decay of the superdeformed 4^+ to the deformed 2^+. The in-band transition is simultaneously well accounted for —see Figure 3.7—, but the theoretical predictions miss badly the two remaining

Table 3.11: Quadrupole properties —in e fm^2 and e^2 fm^4— of the deformed γ band in ^{40}Ca. Full r_2pf calculation.

J	$Q_{spectroscopic}$	$B(E2)_{J\to J-2}$	$B(E2)_{J\to J-1}$	$Q_0(s)$	$Q_0(t)$
2	28.6			100	
3	-0.24		427	-	
4	-17.7	133	284	122	106
5	-25.7	214		111	106
7	-33.5	211		104	90
9	-35.6	175		96	77
11	-45.9	110		115	59
13	-40.5	80		97	49

transitions known experimentally. In this case, the limitations of the method have to be recognized.

The calculated $B(E2)$'s, E_γ's and the branching ratios are presented in Table 3.13 for the in-band and out-band transitions of the $J \geq 6$ states of the superdeformed band. The experimental information can be found in the article by Chiara *et al.* [130]. The calculated branching ratios for the three uppermost transitions of the SD band are close to 100% in agreement with the experimental observation. For the next transition, the predicted 96% branching ratio looks too large when inspecting the Figure in Ref. [130], but the paper does not give a figure for it. However, it is in the decay of the 8^+ member of the superdeformed band that theoretical calculations depart dramatically from the experimental branching ratio, 93% calculated *vs* 20% experimental. Some space will be devoted to this comparison, mainly because it may be due to this very number that the authors of Ref. [130] obtain a fit to their Doppler Shift Attenuation data in which, for $J \leq 10$, the transition quadrupole moments of the band have values that correspond actually to a normally deformed band. Before that, let's mention that the branching ratios of the 6^+ SD state seem

Table 3.12: Out-band transitions from the superdeformed (SD) and normal deformed (ND) bands of ^{40}Ca. The energies in keV and the $B(E2)$'s in e^2 fm^4.

Transition		E_γ		$B(E2)$	
		Theory	Experiment	Theory	Experiment
$2^+_{ND} \rightarrow$	0^+_{GS}	4232	3904	1.8	18±1
$0^+_{SD} \rightarrow$	2^+_{ND}	565	1307	58	134.8±24.5
$2^+_{SD} \rightarrow$	0^+_{GS}	5263	5629	0.1	1.7±0.4
	0^+_{ND}	1769	2277	3	20.9±5.0
$4^+_{SD} \rightarrow$	2^+_{ND}	2045	2638	19.4	21±4
	4^+_{ND}	882	1264	6.8	116±34
	2^+_3	397	1294	2.7	176±41

also consistent with the data of Chiara *et al.* and with a rather pure superdeformed character. It has already been seen that the calculation also describes correctly the 4^+ SD branching ratios.

The argument goes as follows: Given that the phase space factors favor the out-band transition by a factor 9, and considering that the $B(E2)$'s of the $8^+_{SD} \rightarrow 6^+_{SD}$ and $8^+_{ND} \rightarrow 6^+_{ND}$ in Tables 3.1 and 3.3 are 980 e^2 fm^4 and 309 e^2 fm^4 respectively, it is readily seen that the experimental branching ratio cannot be reproduced unless the 9307 keV and 9856 keV experimental states correspond to a 50% mixing of the pure SD and ND states. Assuming that the $J = 6$ states are pure ND and SD, this leads to BR= 27%, with in-band $B(E2) = 490$ e^2 fm^4 and out-band $B(E2) =$ 150 e^2 fm^4. The in-band transition in the ND band should have also $B(E2) =$ 150 e^2 fm^4. If it is further assumed that the $J = 10$, 12338 keV, state of the SD band is pure, it will decay equally to the 9307 keV and 9856 keV $J = 8$ states, which seems to be the experimental situation. Translating this into transition quadrupole moments, we should have $Q_0(t)(10^+)$=118 e fm^2 and $Q_0(t)(8^+) = 122$ e fm^2 in the superdeformed band and $Q_0(t)(8^+) = 69$ e fm^2 in the normally deformed band, in

Table 3.13: Comparison between the theoretical in-band (SD→SD) and out-band (SD→ND) transition probabilities for the states of the superdeformed band of ^{40}Ca with $J \geq 6$. Full r_2pf calculation. The theoretical branching ratios are also included. The energies are in keV and the $B(E2)$'s in e^2 fm^4.

Transition		E_γ(th)	E_γ	$B(E2)_{J\to J-2}$	BR%
$6^+_{SD} \to$	4^+_{SD}	1521	1432	874	
	4^+_{ND}	2403	2695	43	46
$8^+_{SD} \to$	6^+_{SD}	2015	1880	906	
	6^+_{ND}	2904	2921	7.8	93
$10^+_{SD} \to$	8^+_{SD}	2371	2481	844	
	8^+_{ND}	2929	3030	12	96
$12^+_{SD} \to$	10^+_{SD}	2857	2932	546	
	10^+_{ND}	3750	3590	1.5	100
$14^+_{SD} \to$	12^+_{SD}	3100	3230	557	
	12^+_{ND}	3952	4264	5.0	97
$16^+_{SD} \to$	14^+_{SD}	3333	3563	396	
	14^+_{ND}	5520	5531	0.03	100

excellent agreement with the experimental analysis of Refs. [110, 130]. As a bonus, the low spin part of the band remains truly superdeformed. Actually the band is superdeformed all along except for the 8^+ state, even if the accidental degeneracy of the ND and SD 8^+ states provokes a strong reduction of the $B(E2)$'s of the transitions to and from the latter state. In addition, the lifetime of the 9856 keV, $J = 8$, state is reduced by about a factor two.

Then, why are these features absent in the ISM calculation? It is clear that in order to obtain a 50% mixing of the ND and SD states, they must be degenerate before mixing, their effective splitting being not larger than about 200 keV. To match

Table 3.14: Out-band transitions from the deformed γ band of ^{40}Ca. The energies are in keV and the $B(E2)$'s in e^2 fm^4.

Transition		E_γ		$B(E2)$	
		Theory	Experiment	Theory	Experiment
$2^+_\gamma \rightarrow$	0^+_{GS}	5690	5249	0.20	1.0±0.3
	0^+_{ND}	2277	1896	16	10±3
	2^+_{ND}	1575	1343	91	179±50
$3^+_\gamma \rightarrow$	2^+_{ND}	2295	2125	28	27±5
$4^+_\gamma \rightarrow$	2^+_{ND}	2738	2603	20	32±7
	4^+_{ND}	1632	1229	49	49±34

this requirement is beyond the accuracy of our theoretical description. Paradoxically, the calculated excitation energies of the 9307 keV and 9856 keV $J = 8$ states, 9260 keV and 9820 keV look astonishingly precise. But the first excited 8^+ state, experimentally at 8103 keV does not come at the right energy; it its predicted at 8900 keV. This state has a 2p-2h aligned nature and the fact that it mixes strongly with the ND state, that has already been discussed, means that both are degenerate before mixing at about their mean excitation energy.

In a sense, the character of the SD band is closer to what is suggested by the calculated static quadrupole moments in Table 3.6. The only modification brought in by the 8^+ anomaly would be a reduction of its $Q_0(s)$ from 165 e fm^2 to 135 e fm^2.

Finally, the out band transitions of the low spin states of the γ band are collected in Table 3.14 . The experimental information is taken from Ref. [131]. The first concern is to figure out to which extent our hypothesis of low K-mixing is correct in the ISM calculation. For that purpose, the $2^+_\gamma \rightarrow 0^+_{ND}$ and the $2^+_{ND} \rightarrow 0^+_{ND}$ $B(E2)$'s are compared, the former being twenty times smaller. A similar reduction is found in the $4^+_\gamma \rightarrow 2^+_{ND}$ *vs* $4^+_{ND} \rightarrow 2^+_{ND}$ case, thus confirming the validity of the assumption. According to the Davydov-Filippov model [132], the value of *gamma* obtained by

the ratio of the $2^+_\gamma \rightarrow 2^+_{ND}$ to the $2^+_\gamma \rightarrow 0^+_{ND}$ transitions is about 20 degrees. The γ energies resemble quite well the experimental results. The $B(E2)$'s are in excellent agreement with the experiment in all cases.

The overall agreement between the theoretical and experimental level schemes can be seen in Figure 3.10, where all the results presented above have been gathered. Full r_2pf results compared to the experimental data from Refs. [131] and [110]. The width of the arrows is proportional to the strength of the $B(E2)$ transitions, which is given in each case in e^2 fm^4. The dashed arrows distinguish those transtions whose experimental $B(E2)$ value is not available. It can be observed that almost every feature of the experiment can be reproduced in great detail by the full r_2pf calculation. Only a few minor differences are witnessed, maybe the most eye-catching being the theoretical reduction of the strength of the $B(E2)$ transitions on the top of the SD band. On the whole, the agreement is excellent.

3.7 Summary

In this Chapter we have studied within the ISM the coexistence in ^{40}Ca, of a doubly magic spherical ground state with a normal deformed and superdeformed bands. For that purpose, we have worked in a valence space comprising two major oscillator shells.

In first place, we have discussed the algebraic models on which the ISM description of collective features of nuclei is based on. After that, calculations in fixed *n*-particle *n*-hole configurations are performed, confirming the existence of a spherical ground state and a deformed triaxial and a superdeformed axial intrinsic states. Then, the deformed state produces a γ band.

In order to obtain results in the complete r_2pf space, we have studied the role of the spherical Mean Field and the correlations in bringing the *n*-particle *n*-hole configurations at very low excitation energy.

The mechanisms of mixing between different *n*p-*n*h configurations has been examined, and the structure of the physical states in terms of these configurations has been analyzed. The result is that the normally deformed bands are dominated by 4p-4h configurations with important mixing of 6p-6h components. The superdeformed band is clearly dominated by the 8p-8h configurations with small 6p-6h and

4p-4h contributions. In the ground state, the doubly magic configuration amounts to 65%, mixed mainly with 2p-2h states.

The comparison of the theoretical predictions with the experimental data for the energetics of the three above mentioned bands is excellent. The electromagnetic transition probabilities for in-band and out-band transitions have also been computed, obtaining a very good agreement, specially in the in-band transitions. The out-band transitions are in general also very close to the experimental values, but with a few exceptions.

Figure 3.10: Theoretical *vs* experimental level schemes of ^{40}Ca, see the text for details.

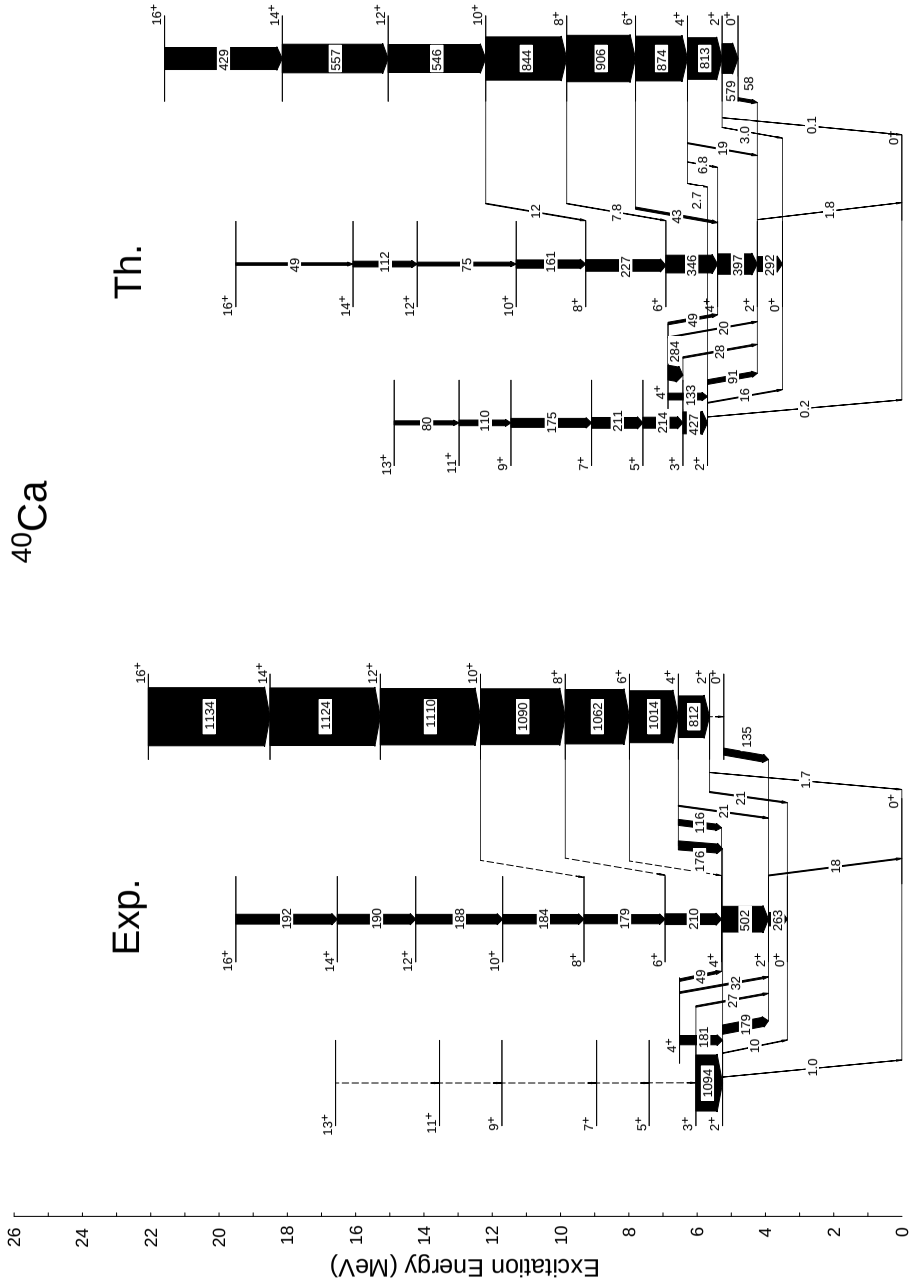

Chapter 4

Study of the Neutrinoless Double Beta Decay: General Considerations

4.1 Introduction

Double beta decay is a very slow weak process. It takes place between two even-even isobars when the single beta decay is energetically forbidden or hindered by large spin difference. A pictorial representation is shown in Figure 4.1 for the $A = 76$ case. This situation is accomplished by around thirty nuclei, even though due to the long lifetimes associated to these decays, only the cases where $Q_{\beta\beta}$ is sufficiently large will be suitable for detection. In addition to this, the parent nuclei must be abundant enough to perform experiment. These two aspects are shown in Table 4.1 below for the transitions considered in this work.

Two different double beta processes can be distinguished. Their Feynman diagrams are pictured in Figure 4.2. The corresponding nuclear reactions are the following:

$$ {}^{A}_{Z}X_{N} \rightarrow {}^{A}_{Z+2}X_{N-2} + 2e^{-} + 2\overline{\nu}_{e}, \tag{4.1} $$

$$ {}^{A}_{Z}X_{N} \rightarrow {}^{A}_{Z+2}X_{N-2} + 2e^{-}. \tag{4.2} $$

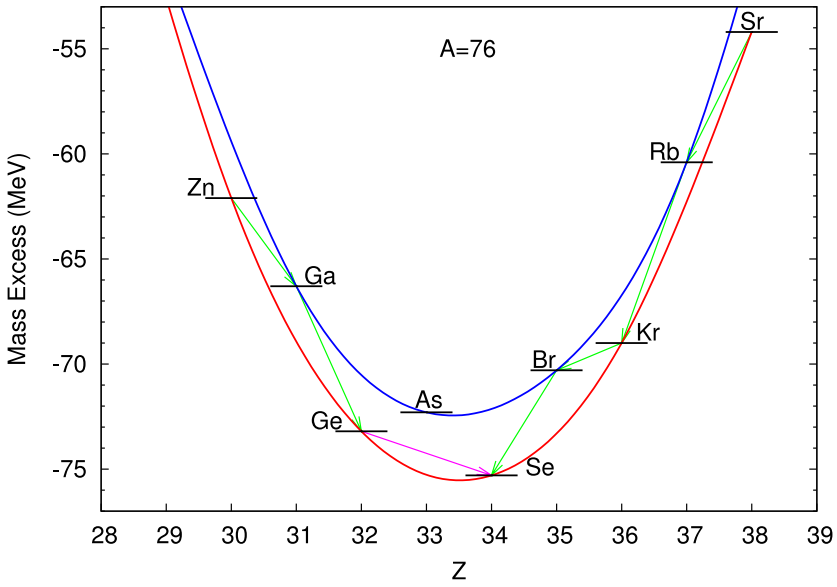

Figure 4.1: Representation of the energies of the $A = 76$ isotones. The single beta decay—green arrows— between ^{76}Ge and ^{76}Se is energetically forbidden, hence leaving $\beta\beta$ —pink arrow— as the only decay channel. The two mass parabolas exist because of the pairing interaction that lowers the energy of even Z–even N nuclei with respect to odd Z–odd N nuclei. For odd A nuclei there is a single mass parabola and all beta transitions are energetically allowed.

Firstly, we have the two neutrinos beta decay ($2\nu\beta\beta$) of Eq. (4.1), originally proposed by Goeppert-Mayer [133]. It is a second order weak process —this is the reason of its low rate—, and the first direct laboratory detection was only achieved as recently as 1987 [134]. Since then, it has been measured for a dozen of nuclei [135].

The alternative is the neutrinoless double beta decay ($0\nu\beta\beta$), proposed by Furry [136] after the Majorana theory of the neutrino [137]. It corresponds to Eq. (4.2). This process is analog to $2\nu\beta\beta$, but only feasible in the case of Majorana type neutrinos, this is, in the case that they are its own antiparticles. For this to be possible, neutrinos would have to be massive, contrary to the Standard Model of electroweak interactions. However, this old conception of neutrinos had to be changed

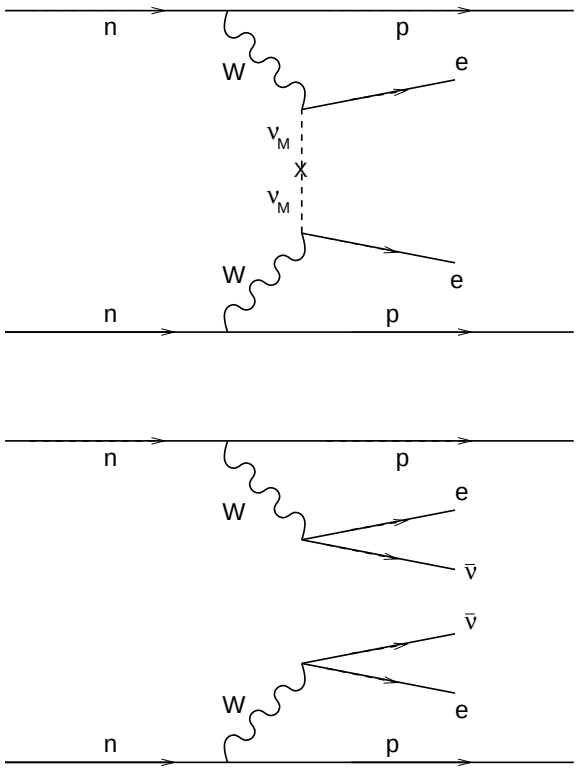

Figure 4.2: Feynman diagrams for the $0\nu\beta\beta$ —above— and $2\nu\beta\beta$ decays.

at the end of the last decade, when the discovery of neutrino oscillations at Super-Kamiokande [138], SNO [139] and KamLAND [140] proved that they have indeed non-zero mass.

Hence, according to the origin of this mass, neutrinos can be either Dirac —as all other leptons in the Standard Model— or Majorana type particles. A Majorana neutrino scenario is particularly interesting from the theoretical point of view, since it would have profound consequences in particle physics. For instance, it would imply the violation of lepton number conservation, so far a good symmetry of the Standard Model.

The $0\nu\beta\beta$ decay happens to be the best way to detect one of these lepton number violating processes[1] and consequently to establish the Majorana character of

[1]Other possibilities are muon conversion in nuclei: $\mu^- + (Z,N) \rightarrow^+ + (Z-2,N)$ and anomalous

the neutrinos. Besides, $0\nu\beta\beta$ is also sensitive to the neutrino mass hierarchy and its absolute mass scale, both still to be determined since from neutrino oscillation experiments only the mass differences are known.

With the exception of one unconfirmed claim [141, 142], $0\nu\beta\beta$ has never been observed, and currently there is a number of experiments either taking place [143, 144] or expected for the near future —see e.g. Ref. [145]— devoted to detect these processes.

Even though a mere positive $0\nu\beta\beta$ signal would imply that neutrinos are of Majorana type, in order to obtain information about the neutrino mass Nuclear Structure plays a key role. The rate of the process is given by [146, 147]:

$$\left(T_{1/2}^{0\nu\beta\beta}\left(0^+ \to 0^+\right)\right)^{-1} = G_{01}\left|M^{0\nu\beta\beta}\right|^2\left(\frac{\langle m_\nu\rangle}{m_e}\right)^2, \tag{4.3}$$

where $\langle m_\nu\rangle$ is the so called effective Majorana neutrino mass. $M^{0\nu\beta\beta}$ represents the nuclear matrix element (NME), this is, the matrix element of the $0\nu\beta\beta$ decay operator between the initial and final nuclei.

Further details will be given along the present Chapter, but directly from Eq. (4.3) it follows that the NME is required to extract information about the neutrino mass from a measured half-life. Even more important is the fact that the theoretical NME's will give indications about for which nuclei the value of the half-life is expected to be the lowest, which is very valuable information for experimental proposals.

The ISM is one of the two leading methods that are able to calculate reliable NME's for most of the possible $0\nu\beta\beta$ emitters. The other is the family of the quasiparticle random-phase approximation (QRPA) [148]. It is a method based on Hartree-Fock plus BCS pairing in which some correlations —namely of RPA type— are incorporated. Calculations within this method have been performed by different groups and a variety of techniques is employed. Their results will be compared with those obtained in this work in the following Sections. Due to the relevance of the issue, other sucessful Nuclear Structure methods are focusing on this double beta decay problem. In particular, results from the Interacting Boson

kaon decays: $K^+ \to \pi^-\mu^+\mu^+$, whose branching ratios are known be $< 10^{-12}$ and $< 10^{-9}$ respectively. The sensitivity of $0\nu\beta\beta$, $T_{1/2} > 10^{25}$ y, is much higher.

Model will become available shortly [149].

In this Chapter, a study of the $0\nu\beta\beta$ NME's will be performed. Previous works within the ISM have been carried out with results for all the nuclei that will be considered here [150, 151, 152]. A more modern calculation can be found in Ref [153].

Many improvements have been made to these results. For instance, the mentioned calculations lack the contribution of the higher order current components of the decay operator (HOC), which have been shown to be necessary to obtain accurate values for the NME's. UCOM type short range correlations (SRC) had not been considered either. In addition to that, the contribution of the different components of the $0\nu\beta\beta$ decay operator is covered in the present work in a much deeper and systematic way than had been previously done. Neither the radial dependence of the NME nor the transitions to excited states had been studied before in the ISM context.

Most of the results that are presented here can be found in Refs. [154] and [155].

4.2 Theoretical framework

The starting point for $0\nu\beta\beta$ decay is the weak Hamiltonian:

$$H_W = \frac{G}{\sqrt{2}}\left(j_{L\mu}J_L^{\mu\dagger}\right) + h.c., \tag{4.4}$$

where $j_{L\mu}$ is the leptonic current. It consists on the electron and left handed light neutrino:

$$j_{L\mu} = \overline{e}\gamma_\mu(1-\gamma_5)\nu_{eL}. \tag{4.5}$$

Neutrino mass eigenstates are not interaction eigenstates, so there is a mixing ruled by the neutrino mixing matrix U:

$$\nu_{eL} = \sum_k U_{ek}\chi_{kL}. \tag{4.6}$$

On the other hand, the hadronic —nuclear— counterpart is given in the impulse approximation by:

$$J_L^{\mu\dagger} = \overline{\Psi}\tau^+ \left(g_V\left(q^2\right)\gamma^\mu - ig_M\left(q^2\right)\frac{\sigma^{\mu\nu}}{2M_p} - g_A\left(q^2\right)\gamma^\mu\gamma_5 + g_P\left(q^2\right)q^\mu\gamma_5 \right)\Psi, \quad (4.7)$$

with q^μ the momentum transferred from hadrons to leptons, this is, $q^\mu = p^\mu_{neutron} - p^\mu_{proton}$.

In the non relativistic case, and discarding energy transfers between nucleons, we have:

$$J_L^{\mu\dagger}(\mathbf{x}) = \sum_{n=1}^{A} \tau_n^- \left(g^{\mu 0} J^0\left(q^2\right) + g^{\mu k} J_n^k\left(q^2\right) \right) \delta\left(\mathbf{x} - \mathbf{r_n}\right), \quad (4.8)$$

where:

$$\begin{aligned} J^0\left(q^2\right) &= g_V\left(q^2\right), \\ \mathbf{J}_n\left(q^2\right) &= ig_M\left(q^2\right)\frac{\sigma_n \times \mathbf{q}}{2M_p} + g_A\left(q^2\right)\sigma_n - g_P\left(q^2\right)\frac{\mathbf{q}\left(\mathbf{q}\sigma_\mathbf{n}\right)}{2M_p}. \end{aligned} \quad (4.9)$$

The couplings are parametrized by the standard dipolar form [156], reflecting the fact that nucleons are not point particles but finite size bodies. This will be referred to as the finite nuclear size effect (FNS). Assuming the conserved vector current (CVC) and the partially conserved axial current (PCAC) hypotheses for the magnetic —g_M— and pseudoscalar —g_P— couplings [157], they read:

$$\begin{aligned} g_V\left(q^2\right) &= \frac{g_V(0)}{\left(1+\frac{q^2}{\Lambda_V^2}\right)^2}, \\ g_A\left(q^2\right) &= \frac{g_A(0)}{\left(1+\frac{q^2}{\Lambda_A^2}\right)^2}, \\ g_M\left(q^2\right) &= \left(\mu_p - \mu_n\right) g_V\left(q^2\right) = \frac{\left(\mu_p - \mu_n\right) g_V(0)}{\left(1+\frac{q^2}{\Lambda_V^2}\right)^2}, \end{aligned}$$

$$g_P\left(q^2\right) = \frac{2M_p g_A\left(q^2\right)}{\left(q^2+m_\pi^2\right)}\left(1-\frac{m_\pi^2}{\Lambda^2}\right) = \frac{2M_p g_A\left(0\right)}{\left(q^2+m_\pi^2\right)\left(1+\frac{q^2}{\Lambda_A^2}\right)^2}\left(1-\frac{m_\pi^2}{\Lambda_A^2}\right) \quad (4.10)$$

where the following values of the bare couplings and constants have been used:

$$\begin{aligned} g_V\left(0\right) &= 1, \\ g_A\left(0\right) &= 1.25, \\ \left(\mu_p-\mu_n\right) &= 3.70, \\ \Lambda_V &= 0.85\,\mathrm{GeV}, \\ \Lambda_A &= 1.09\,\mathrm{GeV}. \end{aligned} \quad (4.11)$$

With this Hamiltonian the rate of the $0\nu\beta\beta$ decay can be calculated:

$$d\Gamma_{0\nu\beta\beta} = 2\pi\sum_{spin}\left|R_{0\nu\beta\beta}\right|^2\delta\left(\varepsilon_1+\varepsilon_2+E_f-E_i\right)d\Omega_{e_1}d\Omega_{e_2}, \quad (4.12)$$

where the reaction matrix element is given by:

$$\begin{aligned} R_{0\nu\beta\beta} = {} & \frac{1}{\sqrt{2}}\left(\frac{G_F}{\sqrt{2}}\right)^2\sum_k\int d\mathbf{x}\int d\mathbf{y}\int\frac{d\mathbf{q}}{\left(2\pi\right)^3\omega}e^{i\mathbf{q}(\mathbf{x}-\mathbf{y})} \\ & \times\sum_a m_k U_{ek}^2\left\langle N_f\right|J_L^\mu\left(\mathbf{x}\right)\left|N_a\right\rangle\left\langle N_a\right|J_L^\nu\left(\mathbf{y}\right)\left|N_i\right\rangle S_{L\mu\nu}\left(\mathbf{x},\mathbf{y},a\right), \end{aligned} \quad (4.13)$$

with m_k the neutrino mass.

The leptonic part, after neutrino contraction takes the form:

$$S_{L\mu\nu}\left(\mathbf{x},\mathbf{y},a\right) = \left(1-P_{12}\right)\frac{\overline{e}\left(\varepsilon_1,\mathbf{x}\right)\gamma_\mu\left(1-\gamma_5\right)\gamma_\nu e^C\left(\varepsilon_2,\mathbf{y}\right)}{\omega+\mu_a-\frac{1}{2}\left(\varepsilon_1-\varepsilon_2\right)}, \quad (4.14)$$

where:

$$\mu_a \equiv \left(E_a^m - \frac{1}{2}\left(E_i + E_f\right) \right). \tag{4.15}$$

This parameter μ_a gives the relative energy of the —virtual— state of the intermediate nucleus with respect to the mean energy of the initial and final states.

In the following, a number of assumptions will be made.

Firstly, we can take advantage of the high momentum of the light neutrino —$\approx$100 MeV. This permits to replace the neutrino energy ω by its momentum q. Moreover, the intermediate states energy E_a^m, which can differ between one another in a few MeV, can also be replaced by an average value $\langle E^m \rangle$. This is, only a common μ_a parameter is required:

$$\mu_a \simeq \mu \equiv \left(\langle E^m \rangle - \frac{1}{2}\left(E_i + E_f\right) \right). \tag{4.16}$$

From here it follows that the intermediate states are no longer needed in the calculation, since the closure relation can be applied:

$$\sum_a \left\langle N_f \right| J_L^\mu(\mathbf{x}) \left| N_a \right\rangle \left\langle N_a \right| J_L^\nu(\mathbf{y}) \left| N_i \right\rangle S_{L\mu\nu}(\mathbf{x},\mathbf{y},a) = \left\langle N_f \right| J_L^\mu(\mathbf{x}) J_L^\nu(\mathbf{y}) \left| N_i \right\rangle S_{L\mu\nu}(\mathbf{x},\mathbf{y}). \tag{4.17}$$

This approximation is correct to more than 90% [158].

On the other hand, we also limit our study to transitions to 0^+ final states, and to cases where electrons are emitted in s wave. Corrections to these approximations are of the order of 1% at most, due to the fact that in other situations —p wave electrons or 2^+ final states— the effective nuclear operators required to couple the initial and final states are very much suppressed compared to the dominant ones that will be considered here.

With these considerations, the expression for the half-life of the $0\nu\beta\beta$ decay reads, as previously advanced:

$$\left(T_{1/2}^{0\nu\beta\beta}\left(0^+ \to 0^+\right) \right)^{-1} = G_{01} \left| M^{0\nu\beta\beta} \right|^2 \left(\frac{\langle m_\nu \rangle}{m_e} \right)^2. \tag{4.1}$$

The specific form of the effective Majorana neutrino mass is $\langle m_\nu \rangle = |\sum_k U_{ek}^2 m_k|$.

Table 4.1: Available energy, $E_f - E_i = Q_{\beta\beta} + 2m_e$, abundancies and kinematic factor G_{01} for the different $0\nu\beta\beta$ transitions studied. The abundancies are shown in percentage, normalized so that ^{232}Th=100. The kinematic factors have been obtained with $g_A(0) = 1.25$.

Transition	$E_f - E_i$ (MeV)	Abundancies (%)	G_{01} (y^{-1})
^{48}Ca $\rightarrow$ ^{48}Ti	5.296	0.2	6.52×10^{-14}
^{76}Ge $\rightarrow$ ^{76}Se	3.061	8	6.41×10^{-15}
^{82}Se $\rightarrow$ ^{82}Kr	4.018	9	2.58×10^{-15}
^{124}Sn $\rightarrow$ ^{124}Te	3.310	6	2.78×10^{-14}
^{128}Te $\rightarrow$ ^{128}Xe	1.890	32	1.80×10^{-15}
^{130}Te $\rightarrow$ ^{130}Xe	3.552	34	4.49×10^{-14}
^{136}Xe $\rightarrow$ ^{136}Ba	3.484	9	4.68×10^{-14}

The neutrino mixing matrix elements U_{ek} may show complex phases, and accordingly the effective mass could be smaller than the actual neutrino masses.

G_{01} is a kinematic factor —dependent on the charge, mass and available energy of the process. Its explicit form is:

$$G_{01} = \frac{(Gg_A(0))^4 m_e^2}{64\pi^5 \ln 2} \int F_0(Z,\varepsilon_1) F_0(Z,\varepsilon_2) \times p_1 p_2 \varepsilon_1 \varepsilon_2 \delta(\varepsilon_1 + \varepsilon_2 + E_f - E_i)\, d\varepsilon_1 d\varepsilon_2 d(\hat{\mathbf{p}}_1 \cdot \hat{\mathbf{p}}_2). \quad (4.18)$$

The Fermi functions $F_0(Z,\varepsilon)$ have also a small dependence on the nuclear radius R, and hence on A. The adopted values of G_{01} used in this work are found in Table 4.1.

It is seen in Eq. (4.18) that the kinematic factor depends on the value of the bare coupling constant $g_A(0)$. Therefore the NME's obtained with different $g_A(0)$ values cannot be directly compared. If we redefine the NME as:

$$M'^{0\nu\beta\beta} = \left(\frac{g_A(0)}{1.25}\right)^2 M^{0\nu\beta\beta}, \tag{4.19}$$

these $M'^{0\nu\beta\beta}$'s are directly comparable no matter which was the value of g_A employed in their calculation, since they share a common G_{01} factor —that of $g_A(0) = 1.25$. In this sense, the translation of $M'^{0\nu\beta\beta}$'s into half-lives is transparent. This change into $M'^{0\nu\beta\beta}$ will be performed whenever comparing to QRPA results calculated with a quenched value of $g_A(0)$.

The NME is obtained from the effective transition operator resultant from the product of the nuclear currents:

$$\Omega(q) = -h^F(q) + h^{GT}(q)\,\boldsymbol{\sigma}_{\mathbf{n}}\boldsymbol{\sigma}_{\mathbf{m}} - h^T(q)\,\mathbf{S}^q_{nm}, \tag{4.20}$$

where $\mathbf{S}^q_{nm} = 3(\hat{\mathbf{q}}\boldsymbol{\sigma}_{\mathbf{n}}\hat{\mathbf{q}}\boldsymbol{\sigma}_{\mathbf{m}}) - \boldsymbol{\sigma}_{\mathbf{n}}\boldsymbol{\sigma}_{\mathbf{m}}$ is the tensor operator. It appears in the $0\nu\beta\beta$ decay in addition to the usual Fermi and Gamow-Teller counterparts. The functions $h(q)$ can be labeled according to the current terms from which they come from:

$$\begin{aligned} h^F(q) &= h^F_{vv}(q), \\ h^{GT}(q) &= h^{GT}_{aa}(q) + h^{GT}_{ap}(q) + h^{GT}_{pp}(q) + h^{GT}_{mm}(q), \\ h^T(q) &= h^T_{ap}(q) + h^T_{pp}(q) + h^T_{mm}(q), \end{aligned} \tag{4.21}$$

whose explicit form can be found in Appendix C. The two most important terms in $0\nu\beta\beta$ decay are h^{GT}_{aa} and h^F_{vv}, respectively. The importance of the rest of the terms in Eq. (4.21) was overlooked until the work of Šimkovic *et al* [159]. They will be referred as higher order components of the nuclear current (HOC)[2].

Integrating over $\mathbf{q}$ we get the corresponding operators in position space, which are called the neutrino potentials. Before radial integration they look like:

[2]The name comes from the fact that, when obtaining the transition operator from the contraction of the hadronic current, they appear at higher order in the transferred momentum q than the two leading terms —which appear at zero order.

$$V_x^{F/GT}(r) = \frac{2}{\pi}\frac{R}{g_A^2(0)}\int_0^\infty j_0(qr)\,\frac{h_x^{F/GT}(q)}{(q+\mu)}q\,dq,$$
$$V_x^{T}(r) = \frac{2}{\pi}\frac{R}{g_A^2(0)}\int_0^\infty -j_2(qr)\,\frac{h_x^{T}(q)}{(q+\mu)}q\,dq, \tag{4.22}$$

where $j_n(x)$ are the spherical Bessel functions, r is the distance between nucleons and R, which makes the result dimensionless is taken as $R = r_0 A^{1/3}$, with $r_0 =$ 1.2 fm. The integrated analytical form of the above potential can be also found in Appendix C.

Finally, the NME reads:

$$\begin{aligned} M^{0\nu\beta\beta} &= -\left(\frac{g_V(0)}{g_A(0)}\right)^2 M^F + M^{GT} - M^T \\ &= \left\langle 0_f^+ \middle| \sum_{n,m} \tau_n^- \tau_m^- \left(-V^F(r) + V^{GT}(r)\,\boldsymbol{\sigma}_\mathbf{n}\boldsymbol{\sigma}_\mathbf{m} - V^T(r)\,\mathbf{S}_\mathbf{nm}^\mathbf{r}\right) \middle| 0_i^+ \right\rangle. \end{aligned} \tag{4.23}$$

4.2.1 Short range correlations

In the calculation of the NME it is also necessary to take into account the short range correlations (SRC) considered either in the transition operator or in the nuclear wave functions.

A fully consistent treatment of the SRC's would demand regularizing the $0\nu\beta\beta$ operator using the same prescription than for the bare interaction. However, this approach is beyond present ISM —or QRPA— capabilities. Hence, general prescriptions, that also come from the regularization of bare interactions into the nuclear medium, are used instead.

A standard method to include SRC's is via a Jastrow type function [160, 161]. This is, the NME is modified as:

$$\langle 0_f^+ | V(r) | 0_i^+ \rangle_{src} = \langle 0_f^+ f(r) | V(r) | f(r)\, 0_i^+ \rangle = \langle 0_f^+ | f(r)^2 V(r) | 0_i^+ \rangle \tag{4.24}$$

with $f(r) = 1 - e^{-ar^2}\left(1 - br^2\right)$ and $a = 1.1$ fm^{-2}, $b = 0.68$fm^{-2}.

Other authors [162] have recently argued that this correction is somewhat too aggressive, and have proposed another method —namely the Unitary Correlation Operator Method (UCOM) [163]— to estimate the SRC's, which leads to a much smoother correction.

We have estimated the value of our ISM results taking an UCOM type SRC's by simulating the correlator as that of the $ST = 01$ channel [164], common throughout the calculation. The correlator of the other important —even— channel is very similar to this one, and the difference should not change our estimated results.

In this case the NME is modified as:

$$\left\langle 0_f^+ \middle| V(r) \middle| 0_i^+ \right\rangle_{SRC} = \left\langle 0_f^+ \middle| V(\widetilde{r}) \middle| 0_i^+ \right\rangle, \tag{4.25}$$

where:

$$\widetilde{r} = r\left(1 + e^{-e^{\left(\frac{r}{\beta}\right)}} \frac{\alpha}{r}\left(\frac{r}{\beta}\right)^{\eta}\right), \tag{4.26}$$

with α=1.3793 fm, $\beta = 0.8853$ fm and $\eta = 0.3724$.

Whether the UCOM or Jastrow method is more appropriate to treat the $0\nu\beta\beta$ SRC's is still an open question. Therefore, taking into account the limitations of our method regarding the SRC's, the different results obtained by both prescriptions may be considered as an estimation of the range of the effect of these SRC's.

Unless otherwise stated, the ISM results shown in the following Sections have been calculated using the Jastrow prescription.

4.3 Results of NME's of $0\nu\beta\beta$ decays

Following the considerations of the previous Section, we have performed calculations for the $0\nu\beta\beta$ decays of the emitters ^{48}Ca, ^{76}Ge, ^{82}Se, ^{124}Sn, ^{128}Te, ^{130}Te and ^{136}Xe, using the ISM coupled code NATHAN, ideally adapted for the calculation of 0^+ states. Full diagonalizations are accomplished within different valence spaces and effective interactions. For instance, the decay of ^{48}Ca is studied in the pf major shell, and the KB3 interaction is employed. For the case of ^{76}Ge and ^{82}Se, the

valence space consisting on $1p_{3/2}$, $0f_{5/2}$, $1p_{1/2}$ and $0g_{9/2}$ is diagonalized using the GCN28.50 interaction. Finally the $0g_{7/2}$, $1d_{3/2}$, $1d_{5/2}$, $2s_{1/2}$ and $0h_{11/2}$ valence space and the GCN50.82 interaction are used in the decays of ^{124}Sn, ^{128}Te, ^{130}Te and ^{136}Xe. The latter spaces and interactions will be discussed in detail elsewhere [45].

Apart from obtaining the value of the NME's for each of the nuclei outlined above, it is the aim of this work to explore in depth the structure of these NME's, in order to gain insight into the details of the calculation and recognise possible uncertainties.

In particular, the importance of the higher order currents (HOC), finite nuclear size effects (FNS) and short range correlations (SRC) —either of Jastrow or UCOM type— will be studied. The relative role of the Fermi, Gamow-Teller and Tensor components of the operator will also be explored. The results obtained will be compared to those of state-of-the-art QRPA calculations.

The disassembled results for the NME in the $^{76}\text{Ge} \rightarrow {}^{76}\text{Se}$ transition are shown in Tables 4.2-4.5. The evolution of the NME as different terms are included in the calculation is also presented. On the one hand we see the effect of taking into account SRC and FNS terms. On the other, we can study the relevance of the

Table 4.2: Evolution of the Fermi component of the $0\nu\beta\beta$ NME for $A = 76$. M_{hoc} denotes the NME without finite size effects or short range correlations. The result with the FNS are included is labeled by $M_{hoc+fns}$. When it is SRC's that are included the result is denoted by $M_{hoc+src}$. The final value, this is, with both FNS and SRC effects, is simply called M.

	$\nu\nu$
$-M^F_{hoc}/g_A^2$	0.49
$-M^F_{hoc+fns}/g_A^2$	0.35
$-M^F_{hoc+src}/g_A^2$	0.28
$-M^F/g_A^2$	0.24

Table 4.3: Evolution of the Gamow-Teller component of the $0\nu\beta\beta$ NME for $A = 76$. The contribution of each component of the decay operator is given, with the labels for each column referring to the operator components as defined in Eq. (4.21). The rest of the labels, as in Table 4.2.

	aa	$+ap$	$+pp$	$+mm$
M^{GT}_{hoc}	3.54	2.35	2.81	2.81
$M^{GT}_{hoc+fns}$	3.10	2.15	2.45	2.61
$M^{GT}_{hoc+src}$	2.56	1.85	2.09	2.09
M^{GT}	2.46	1.78	1.98	2.06

Table 4.4: Evolution of the Tensor component of the $0\nu\beta\beta$ NME for $A = 76$. Labels as in Tables 4.2 and 4.3.

	$+ap$	$+pp$	$+mm$
M^{T}_{hoc}	0.014	0.011	0.013
$M^{T}_{hoc+fns}$	0.011	0.008	0.009
$M^{T}_{hoc+src}$	0.014	0.011	0.012
M^{T}	0.010	0.008	0.009

different components of the transition operator, in particular that of the different HOC terms. The label M_{hoc} means that no FNS or SRC's were taken into account. The full NME, with these two effects included, is denoted simply by M. The Fermi, Gamow-Teller and Tensor parts of the operator are displayed separately. Finally, the full results are shown.

Table 4.5: Evolution of the full NME for $A = 76$. Labels as in Figures 4.2 and 4.3.

	$aa+vv$	$+ap$	$+pp$	$+mm$
M_{hoc}	4.04	2.82	3.29	3.29
$M_{hoc+fns}$	3.45	2.49	2.79	2.96
$M_{hoc+src}$	2.85	2.12	2.36	2.36
M	2.70	2.01	2.21	2.30
ΔM		-25%	+7%	+3%

4.3.1 Gamow-Teller, Fermi and Tensor components

The first thing that can be noticed is that the value of the Fermi component of the NME is much smaller than that of the Gamow-Teller one, which is therefore the leading component. Although this hierarchy is also observed in QRPA calculations, the Fermi part is not that much suppressed. In Chapter 5, where we will try to account for the differences between ISM and QRPA results, we will come back to this matter.

More shocking is the fact that the role of the Tensor component is negligible within the NME's. If this behaviour is compared with QRPA calculations, a disagreement is found. While for some QRPA authors their contribution is, as in our case, negligible [165], others claim that it amounts to 5% for $A = 76$ and 8% for $A = 130$ prior to SRC's [159]; after that their influence is necessarily larger since Tensor type contributions, contrary to Fermi and Gamow-Teller parts, are not reduced by SRC's. We will also return to this issue in Chapter 5.

4.3.2 HOC, FNS and SRC contributions

We can also look at the relative value of the different components of the transition operator, this is, the different terms appearing in Eq. (4.21), and in particular the overall HOC contribution. This is explicitly written in Table 4.5, while the evolution can be traced back to Tables 4.2-4.4. The results should be compared with the

rough estimates that can be obtained with the help of Equation (C.1) in Appendix C assuming $q \approx 100$ MeV. With this surmise, we obtain: $h_{aa} \approx h_{vv} \approx 1$, $h_{ap} \approx 0.20$, $h_{pp} \approx 0.04$ and $h_{mm} \approx 0.02$.

Our ISM results show that the HOC terms contribute to reduce the bare matrix element in approximately 20%. However the effect of the HOC contributions in the full NME —FNS and SRC's taken into account— is a bit smaller, 15%, which only means that HOC contributions are slightly more regularized by FNS and SRC effects than the lower order —*aa* and *vv*— terms. In addition to that, the *mm* contribution to HOC, which increases the NME and hence reduces the net HOC effect, vanishes in the bare case. Hence, we conclude that the overall HOC contribution is of the expected relative value, and, moreover, the individual terms are also very close to their estimate. They are found only a bit larger, but with the correct relative figures.

Therefore, according to these results, certainly h_{ap} cannot be neglected. Since the Gamow-Teller contribution will be the dominant one, and both the h_{pp} and h_{mm} have the same sign and opposite to h_{ap}, it seems sensible to keep all these terms in the calculation.

In Table 4.6 we can see the overall HOC contribution for all the transitions studied. As was pointed out above, the numbers are very similar for all the decays. An exception in perhaps the case of the decay of the doubly magic ^{48}Ca, whose NME is very much suppressed. In the next Chapter we will try to understand this rather peculiar case.

We can also observe in Table 4.6 the importance of the FNS and SRC's —for the moment, only or the Jastrow type. Again a common pattern is followed. It is seen that, once HOC are included in our calculation, FNS amounts to 10% and Jastrow SRC's reduce the NME in another 25%.

A comparison with the QRPA calculations can be done, for $A = 76$, observing Table 4.7. If we focus in the relative importance of the different approximations, we can see that all three calculations show the same trend, though the details may change a bit from one another. Hence we can conclude that HOC contributions reduce the NME in about 10-20%, taking into account FNS effects produces an additional 10-20% decrease and finally Jastrow type SRC's reduce the NME another 20-25%. The overall effect from the original bare NME adds up to 35-45%.

Table 4.6: [Evolution of the $0\nu\beta\beta$ NME's for the different decays studied.] Evolution of the $0\nu\beta\beta$ NME's for the different decays studied. The reduction due to HOC —both before and after FNS—, FNS and SRC's with respect to the previous result are shown, in percentage.

Transition	M_{bare}	M_{fns}	M_{hoc}	$M_{h.+fns}$	$M^{0\nu\beta\beta}$	$\%_{hoc}^{b/fns}$	$\%_{fns}$	$\%_{src}$
$^{48}Ca \rightarrow {}^{48}Ti$	1.42	1.15	1.04	0.93	0.61	26/19	11	34
$^{76}Ge \rightarrow {}^{76}Se$	4.04	3.45	3.29	2.96	2.30	19/14	10	22
$^{82}Se \rightarrow {}^{82}Kr$	3.79	3.24	3.09	2.79	2.18	18/14	10	22
$^{124}Sn \rightarrow {}^{124}Te$	3.82	3.22	3.11	2.77	2.10	19/14	11	24
$^{128}Te \rightarrow {}^{128}Xe$	4.20	3.56	3.37	3.05	2.34	20/14	9	23
$^{130}Te \rightarrow {}^{130}Xe$	3.90	3.27	3.17	2.81	2.12	19/14	11	25
$^{136}Xe \rightarrow {}^{136}Ba$	3.20	2.70	2.61	2.32	1.76	19/14	11	24

Table 4.7: Comparison of the NME for the $^{76}Ge \rightarrow {}^{76}Se$ $0\nu\beta\beta$ decay for this work (ISM) and the Jyväskylä (JY07) and Tübingen (TU99) groups. The values of TU99 were originally calculated with $r_0 = 1.1$ fm, and have been corrected to be directly comparable with the others. This remark applies whenever results from this group are used in the following.

	M_{bare}	M_{fns}	M_{hoc}	$M_{h.+fns}$	$M^{0\nu\beta\beta}$	$\%_{hoc}^{b/fns}$	$\%_{fns}$	$\%_{src}$
ISM	4.04	3.45	3.29	2.96	2.30	19/14	10	22
JY07 [165]	8.53	-	7.72	6.36	4.72	9/–	18	26
TU99 [159]	-	7.03	-	5.63	-	–/20	≈ 10	≈ 20

Table 4.8: Contributions of the Jastrow and UCOM type short range correlations to the NME for the different decays studied.

$0\nu\beta\beta$ Transition	$M_{no\,SRC}$	$M^{0\nu\beta\beta}_{UCOM}$	$M^{0\nu\beta\beta}_{Jastrow}$	$\Delta M_{UCOM}(\%)$	$\Delta M_{Jastrow}(\%)$
$^{48}Ca \rightarrow {}^{48}Ti$	0.92	0.85	0.61	8	34
$^{76}Ge \rightarrow {}^{76}Se$	2.96	2.81	2.30	5	22
$^{82}Se \rightarrow {}^{82}Kr$	2.79	2.64	2.18	5	22
$^{124}Sn \rightarrow {}^{124}Te$	2.77	2.62	2.10	5	24
$^{128}Te \rightarrow {}^{128}Xe$	3.05	2.88	2.34	6	23
$^{130}Te \rightarrow {}^{130}Xe$	2.81	2.65	2.12	6	25
$^{136}Xe \rightarrow {}^{136}Ba$	2.32	2.19	1.76	6	24

In our ISM calculations, these three contributions when applied to the bare NME, give reductions of 20%, 15% and 30%, respectively —$M_{src} = 2.85$, not included in Table 4.6, but shown in Table 4.5. Therefore, these effects do not pile up, the total reduction amounting to roughly 70% of the sum of the individual contributions.

As was mentioned in Section 4.2.1 the SRC's can also be parametrized with an UCOM type function. Our results when employing this method are shown, together with those obtained within the Jastrow prescription, in Table 4.8. A 5% reduction of the NME is found with the UCOM SRC ansatz, number which is in agreement with the QRPA calculations. Thus, treating the SRC's with a softer prescription of this type increases our Jastrow correlated final results by some 20%, leaving the full reduction of the NME due to all contributions at around 25-35%.

Since the Jastrow prescription gives a relatively large reduction of the NME and the UCOM approach is quite soft, these two numbers could be considered as two limiting cases of the actual effect of SRC's. In this sense, they remark the uncertainty on the NME due to the treatment of the SRC's in our calculations.

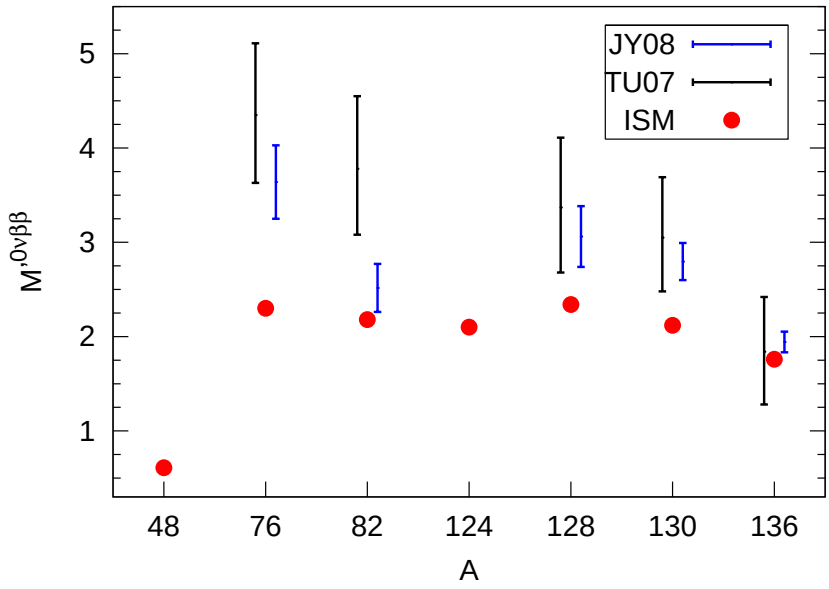

Figure 4.3: The neutrinoless double beta decay $M'^{0\nu\beta\beta}$'s for ISM and QRPA calculations treating the SRC's with the Jastrow approach. Tu07 QRPA results from Ref. [166] and Jy08 results from Ref. [167].

4.3.3 Final value of the NME's

So far we have studied the different contributions that build the final NME value. These full results have already been presented, for instance in Table 4.6, for Jastrow type SRC's, and in Table4.8 for both Jastrow and UCOM type. We find that, except in the special case of ^{48}Ca, the NME's have a fairly constant value, around 2.2 in the case of Jastrow or 2.7 if we use the UCOM.

Finally, we can compare the overall results for the ISM and QRPA in these two cases. This is done in Figures 4.3 and 4.4 for the Jastrow and UCOM type SRC's, respectively. In order to compare with QRPA calculations that used a quenched value of $g_A(0)$, the NME represented is $M'^{0\nu\beta\beta}$, as defined in Eq. (4.19).

Both Figures show the same pattern. Then it is confirmed that the net effect of treating SRC's with the Jastrow or UCOM methods, both in ISM and QRPA, only consist in an overall displacement of the results.

In the nuclear physics community, there is work in progress in order to deter-

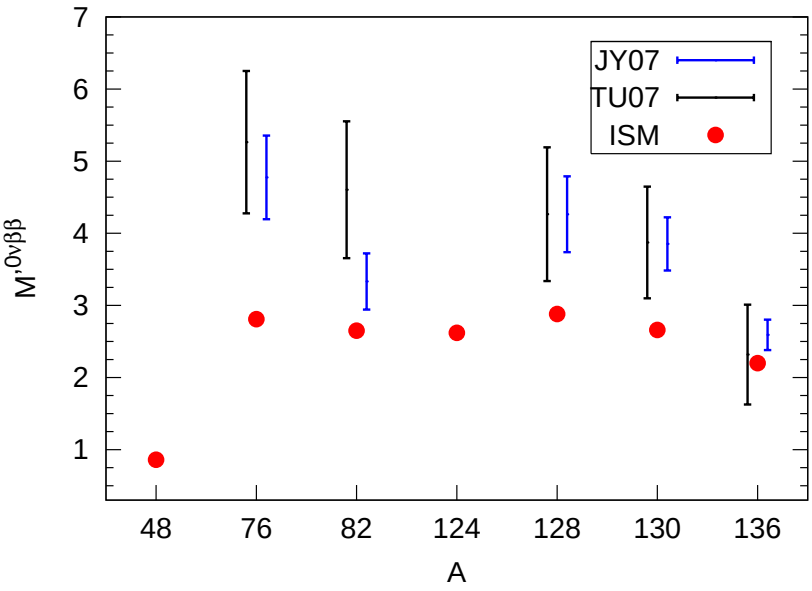

Figure 4.4: Same as fig.4.3 but with UCOM type SRC's. Tu07 QRPA results from Ref. [168] and Jy07 results from Refs. [165, 169].

mine whether the Jastrow or UCOM prescriptions is more appropriate to estimate the SRC's. Preliminary results have been obtained by Engel *et al.* [170], calculated within an ISM context and performing a proper renormalization of the $0\nu\beta\beta$ operator, similar to that of the effective Hamiltonian. Perturbation theory is employed in the process. This renormalization can be performed in such a way that different contributions can be considered separately. One of these are the short range —high momentum— correlations. Their results point in the direction of a rather small reduction of the NME's due to these SRC's, hence vindicating the use of the UCOM prescription. When the full renormalization process is considered, the final NME is found to be very similar to that obtained with the initial bare operator. Once this issue is settled, the NME's will be predicted with considerably higher accuracy, and the dominant uncertainties will be coming from the method used to obtain the wave functions —interaction, valence space, correlations. We comment more on these effects below.

The reason why the QRPA NME's show large error bars is mainly due to the use of quenched and not quenched values for $g_A(0)$ —1.0 and 1.25, respectively.

In our ISM results only $g_A(0) = 1.25$ is considered. This choice, instead of the quenched value needed for pure Gamow-Teller processes in nuclei, is consistent with the use of the closure approximation, in which the multipole decomposition of the decay plays no role at all. In a calculation without closure —as these of the QRPA— the use of the quenched $g_A(0)$ can be justified only in the $J = 1^+$ channel, which is not the dominant one in the $0\nu\beta\beta$ decay. Hence, its effects in the NME's are bound to be small and, depending on the phase of its contribution relative to those of the other multipolarities, this will be either to increase or to decrease the NME's. Furthermore, even for this particular channel, the reasons to choose a quenched $g_A(0)$ are not compelling because the $J = 1^+$ operator of the $0\nu\beta\beta$ decay may not resemble the pure Gamow-Teller operator of the $2\nu\beta\beta$ decay. On the QRPA results, the non quenched results correspond to the upper part of the error bars.

The QRPA results agree well between them, but lie systematically above our ISM NME's, particularly if we compare the ISM, non quenched, with the corresponding QRPA NME's —upper part of the result bars. The only exception to this rule, in the transitions for whom there are results for both methods, appears in the $A = 136$ decay.

This discrepancy between ISM and QRPA results is very unsatisfying in order to get reliable and precise values of the NME's, as is demanded by experimentalists and particle physicists. In the following Chapter, much work will be devoted to explore different possible sources of uncertainty that may reduce this disagreement.

Other effects that may modify our ISM results have already been studied in the past. For instance, the effect of different effective interactions was considered in Ref. [153]. The effect was found to be small —10%-20% either increasing or lowering the ISM value.

It was also studied in this Reference the effect on the NME's that would have an enlargement of the valence space. Then, small components of the nuclear wave functions will appear in the extra orbits. This is quite relevant since QRPA calculations, not including full configurations within a given valence space, are performed in valence spaces which are substantially larger than these of the ISM calculations. For instance, calculations for $A = 76, 82$ comprise at least two major oscillator shells, and these of $A = 128, 130, 136$ can reach up to four major shells. The de-

cays of nuclei ^{82}Se and ^{136}Xe were studied, and moderate increases on the NME's, of 20% and 15% were found, respectively. These estimates are conservative, so much larger corrections are not expected. Moreover, the effect of the orbits missing in our ISM valence spaces has been very recently quantified in $\approx 15\%$ for the $A = 76$ transition [171]. More explorations about this issue are required, but the preliminary conclusion is that ISM results seem to be robust against the enlargement of the valence space.

4.4 Radial dependence of the NME

Very recently the radial evolution of the NME has been studied in Ref. [168], in order to see for what internucleonic distances r the NME gets the major contribution. This is done by representing the operator $C(r)$ defined as:

$$M^{0\nu\beta\beta} = \int_0^\infty C(r)dr \tag{4.27}$$

The form of this operator is shown in Figure 4.5 for all the transitions studied. As can be seen, there is a common trend for all decays. The separate behaviour of Gamow-Teller and Fermi contributions is represented in Figure 4.6 for the ^{136}Xe $\rightarrow$ ^{136}Ba decay. The rest of the transitions follow the same pattern.

These results are in full agreement with the QRPA, confirming the findings of Ref. [168]. This is, beyond $r = 3$ fm there is no overall contribution to the NME, while the maximum value of $C(r)$ occurs around $r = 1$ fm. This means that almost the complete value of the NME comes from the contribution of decaying nucleons which are close to each other. This distance corresponds to a momentum of $q \approx$ 200 MeV, twice the expected value estimated in Section 4.2. Such a small distance is partly due to the cancellation that happens between the contribution of decaying pairs coupled to $J = 0$ and $J > 0$, as can be seen for the dominant GT component of the ^{82}Se $\rightarrow$ ^{82}Kr $0\nu\beta\beta$ decay in Figure 4.7 —for all the other transitions the same tendency is reproduced.

That the NME's radial shape of the QRPA and ISM calculations be identical is quite intriguing and perhaps points to a hidden simplicity in their physics. In fact,

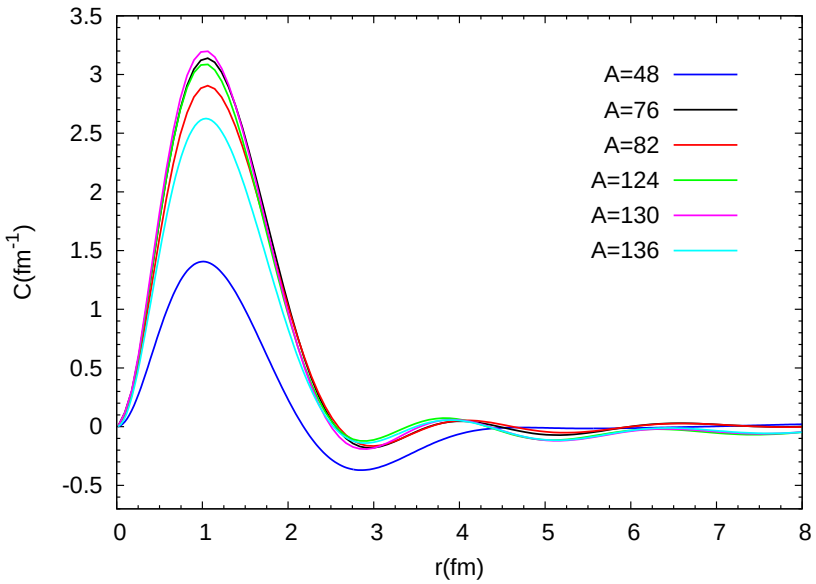

Figure 4.5: Evolution of $C(r)$ for the ^{48}Ca $\rightarrow$ ^{48}Ti, ^{82}Se $\rightarrow$ ^{82}Kr, ^{124}Sn $\rightarrow$ ^{124}Te, ^{130}Te $\rightarrow$ ^{130}Xe and ^{136}Xe $\rightarrow$ ^{136}Ba transitions. The SRC's are not included in the calculation.

one can argue that QRPA and ISM NME's, radial dependence included, differ only by a scaling factor, which can be expressed as the ratio of the average number of pairs in both calculations, in accordance to what will be studied in Chapter 5.

4.5 Transitions to excited final states

When considering the $0\nu\beta\beta$ process, the most favourable decay channel is, due to phase space considerations, the 0^+ ground state to ground state one, which is the case of all transitions so far presented in this work. However, for experimental reasons, it would be very interesting to have a decay to an excited state if it is not too much suppressed compared to the decay to the 0^+_{gs}, because the background reduction, coming from the simultaneous detection of the electrons from the $0\nu\beta\beta$ decay and the photon(s) from the decay of the final nucleus excited state, might make up for the longer lifetime.

In order to find a candidate for this final excited state, higher spins have to be

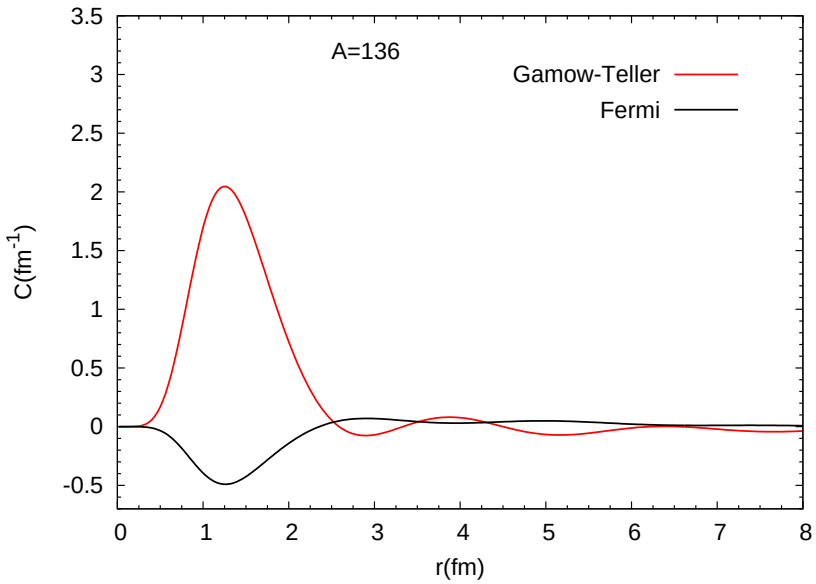

Figure 4.6: Evolution of the Fermi and Gamow-Teller parts of $C(r)$ for the ^{136}Xe $\rightarrow$ ^{136}Ba transitions. The SRC's are not included in the calculation.

discarded since these decays are disfavored not only by the phase space but also by the transition operator, which in order to couple different spin states is necessarily of higher order in the current —and hence much smaller in magnitude. However, excited 0^+_1 states could have a chance, as they share the transition operator with the decays to the ground state. In this new case the phase factor would disfavour the decay but, if the NME pushed in the opposite direction and increased it enough, then the lifetime of the process would not be much larger than the corresponding to the 0^+_{gs}. To explore this possibility, we have computed the NME's of the $0\nu\beta\beta$ decays to excited 0^+_1 states.

The results are gathered in Table 4.9. The first 0^+ excited state in ^{128}Xe lies at higher energy than the ^{128}Te ground state, so there is no possible transition in this case. With the only exception of the relatively small increase of our result for $A = 48$, not really significant because of its huge space factor suppression, we see that a common feature of all calculations is that the NME's for the decays to 0^+_1 states are smaller than the decays to the ground state. This has been the case also in previous QRPA calculations. However, since these results have been

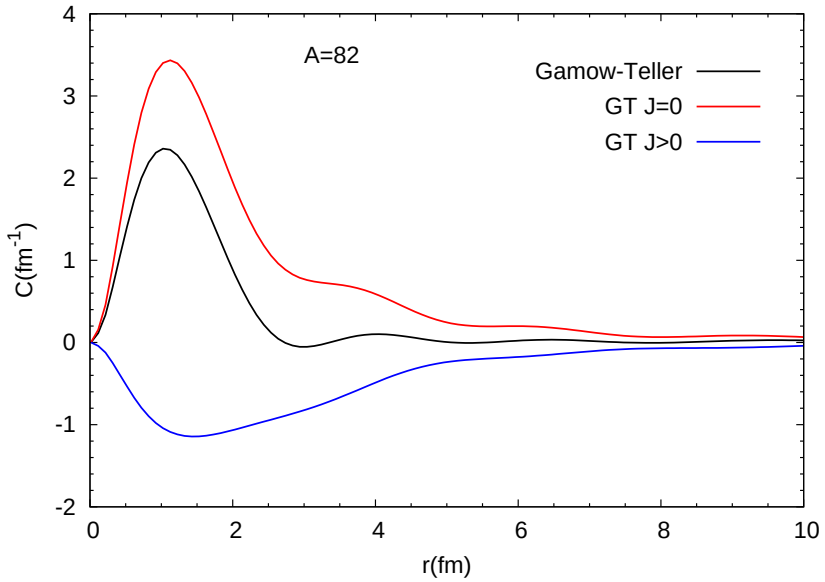

Figure 4.7: Evolution of the Gamow-Teller part of $C(r)$ for the ^{82}Se $\rightarrow$ ^{82}Kr transition. The contribution of decaying pairs coupled to $J = 0$ and $J > 0$ is also shown. The SRC's are not included in the calculation.

Table 4.9: NME's for the $0\nu\beta\beta$ decays to the excited 0_1^+ states, for all the transitions studied. The ground states are denoted by *gs*. Half-lives are calculated for $\langle m_\nu \rangle = 1$ eV.

	$A = 48$	$A = 76$	$A = 82$	$A = 124$	$A = 130$	$A = 136$
$M^{0\nu\beta\beta}_{gs\rightarrow gs}$	0.61	2.30	2.18	2.10	2.12	1.77
$M^{0\nu\beta\beta}_{gs\rightarrow 0_1^+}$	0.68	1.49	0.28	0.80	0.19	0.49
$\frac{G_{01}(gs\rightarrow gs)}{G_{01}(gs\rightarrow 0_1^+)}$	85	12	11	40	38	22
$T^{gs\rightarrow gs}_{1/2}$ (10^{24} y)	10.8	7.70	1.94	2.13	1.29	1.78
$T^{gs\rightarrow 0_1^+}_{1/2}$ (10^{26} y)	7.35	2.28	12.9	5.82	61.2	5.00

superseeded by more recent ones for the initial and final ground states —the case of Refs. [172, 173, 174, 175], which do not consider the HOC relevant terms— or do not treat SRC's properly —as happens in Ref. [176]—, new calculations for the transitions to final 0_1^+ states are required to be comparable to our numbers.

Table 4.9 also includes the predicted half-lives for the transitions. We see that our results are typically two orders of magnitude longer for the decays to excited states. The least disfavored $gs \rightarrow 0_1^+$ transition would be that of ^{76}Ge, which is hindered by a factor 2.4 from the NME times 12, the reduction factor coming from the phase space. This is, in that case the $gs \rightarrow 0_1^+$ transition is suppressed by a factor $25-30$ compared to the $gs \rightarrow gs$, which is probably too large to be compensated by the experimental gain via background reduction. Nevertheless, it corresponds to experimentalists to evaluate the practical interest of the decay to the excited 0^+ in view of such a suppressed rate.

4.6 Summary

In this Chapter we have studied several aspects of the neutrinoless double beta decay. After the theoretical introduction in which we discuss the form of the decay operator and the assumptions present in our calculations, we have obtained results for the nuclear matrix elements of seven different transitions.

The contribution of different parts of the decay operator to the NME have been studied as well. The behaviour is very similar for all the transitions. Both the finite size effects and the higher order currents have been found to play an important role to obtain an accurate value of the NME. We have also studied the role of the short range correlations of the wave functions into the final value of the NME, by studying two possible type of correlations, that of the Jastrow and UCOM types. The results obtained using each method differ in about 20%, which is a measure in the uncertainty, due to the SRC's, that we have in our NME's.

The NME results as well as the partial contribution of each component have been compared with the values obtained by the alternative QRPA calculations. We find that the relative contributions to the NME are similar in both methods. In addition to that, the radial behaviour of the NME is also shared by the ISM and the QRPA. The Tensor component of the NME has been found to be negligible, in

agreement with one of the two leading QRPA groups. However, the NME in our ISM calculations is systematically found smaller than QRPA values.

Finally, we have also studied transitions to first excited 0_1^+ states, with the result that they are very much suppressed compared to the standard decays to the ground states of the final nuclei. The least hindered case would be the $A = 76$ transition, whose decay to the excited state is predicted to be 25 times less probable than the one to the ground state.

Chapter 5

Study of the Neutrinoless Double Beta Decay: Nuclear Structure Aspects

5.1 Introduction

We have just seen in Chapter 4 that a discrepancy is found when comparing ISM and QRPA results for the NME of $0\nu\beta\beta$ decays. In the present Chapter, in order to try to find the origin of this disagreement, we will analyze the NME in more detail.

In particular, we will study the influence of the pairing content of the wave functions of the initial and final nuclei in the NME. This task will be performed with the help of seniority truncations, which will give us the effect of breaking pairs coupled to $J = 0$ in the wave functions.

In addition to that, the role of deformation of the nuclei involved in the $0\nu\beta\beta$ decay will be explored. This is, in a sense, a complementary study to that of the pairing content. Its importance is also given by the existence of a possible $0\nu\beta\beta$ emitter, ^{150}Nd, well deformed, which would decay into ^{150}Sm, nearly spherical.

Finally, we will make a study of the particular $A = 76$ case in the light of the new experimental of neutron and proton occupancies that have been recently published [177, 178].

Most of the results that are presented here can be found in Refs. [154], [155]

and [179].

5.2 Pairing and the $0\nu\beta\beta$ decay

Pairing is the ultimate responsible that double beta decay exists at all. Indeed, it is the pairing interaction that lowers the energies of the even-even nuclei, that will become mother and granddaughter in the double beta process, with respect to the odd-odd nucleus whose single beta decay is energetically forbidden for the mother nucleus. The situation was sketched in Figure 4.1.

5.2.1 Pairing and the full NME

Firstly, we can study the relation between pairing and the $0\nu\beta\beta$ decay by looking at the dependence of the NME on the angular momentum of the decaying pair. For that purpose, the two body decay operator can be written in the form:

$$\hat{M}^{0\nu\beta\beta} = \sum_{J} \left(\sum_{ijkl} M^{J}_{ijkl} \left[\left(a^{\dagger}_{i} a^{\dagger}_{j} \right)^{J} \left(a_{k} a_{l} \right)^{J} \right]^{0} \right), \tag{5.1}$$

where the indices i, j, k, l run over the single particle orbits of the spherical nuclear Mean Field. With the aid of the techniques of Ref. [78], these operators can be factorized as:

$$\hat{M}^{0\nu\beta\beta} = \sum_{J^{\pi}} \hat{P}^{\dagger}_{J^{\pi}} \hat{P}_{J^{\pi}}. \tag{5.2}$$

The operators $\hat{P}_{J^{\pi}}$ annihilate pairs of neutrons coupled to J^{π} in the mother nucleus, while the operators $\hat{P}^{\dagger}_{J^{\pi}}$ substitute them by pairs of protons coupled to the same J^{π}. The overlap of the resulting state with the ground state of the granddaughter nucleus gives the J^{π}-contribution to the NME. The internal structure of these exchanged pairs is dictated by the $0\nu\beta\beta$ operator.

The results for the Gamow-Teller component of $A = 82$ can be found in Figure 5.1. The graph is very suggestive, because it is seen very clearly that the dominant contribution corresponds to the decay of the $J = 0$ pairs, whereas the contributions of the pairs with $J > 0$ are either negligible or have opposite sign to the

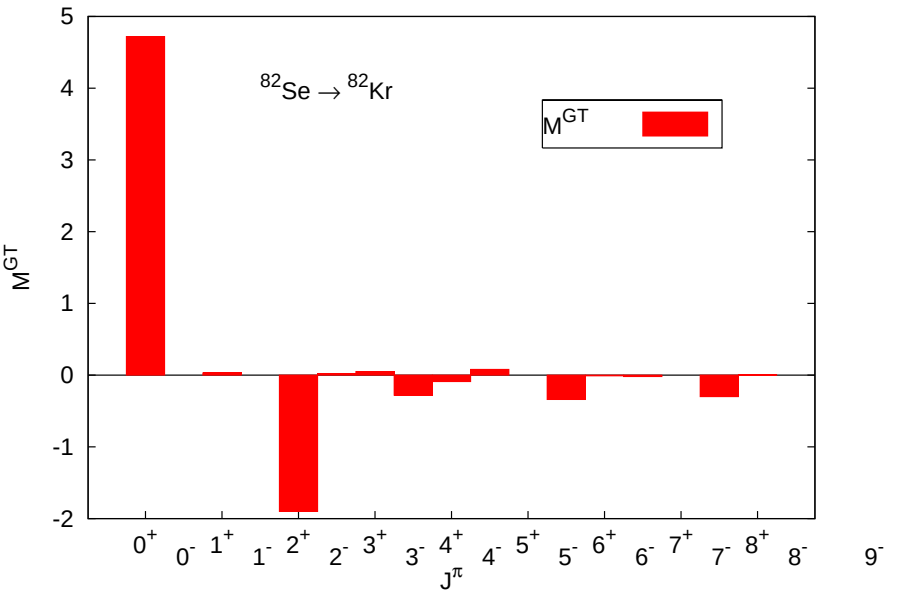

Figure 5.1: Contributions to the Gamow-Teller component of the NME as a function of the J^{π} of the transformed pair for the ^{82}Se → ^{82}Kr transition.

leading one. Moreover, the cancellations between these two parts are substantial. These features are also present in the QRPA calculations. The values of the $J = 0$ and $J > 0$ components can be found in Table 5.1. It is clearly seen that all the cases behave similarly. In the very suppressed case of the ^{48}Ca decay, it can be seen that the 0^{+} contribution is much smaller than that of the rest of the cases, causing the low value of its NME.

To better grasp this mechanism, we can express the NME in a basis of generalized seniority s. This is, s counts the number of unpaired nucleons in the nucleons. Hence, we can write the initial and final states as:

$$\left|0_i^+\right\rangle = \sum_s \alpha_s \left|s\right\rangle_i \qquad \left|0_f^+\right\rangle = \sum_s \beta_s \left|s\right\rangle_f , \tag{5.3}$$

The decomposition of the wave functions will be displayed in Table 5.3. It will be discussed below.

From that decomposition, we obtain that the $J = 0$ terms provide almost all the

Table 5.1: Contributions to the Gamow-Teller part of the NME from the decaying pairs coupled to $J = 0$ and $J > 0$.

	M^{GT}	$M^{GT}(J=0)$	$M^{GT}(J>0)$
^{48}Ca $\rightarrow$ ^{48}Ti	0.57	2.88	-2.71
^{76}Ge $\rightarrow$ ^{76}Se	2.06	5.11	-3.05
^{82}Se $\rightarrow$ ^{82}Kr	1.96	4.72	-2.76
^{124}Sn $\rightarrow$ ^{124}Te	1.82	5.13	-3.31
^{128}Te $\rightarrow$ ^{128}Xe	2.04	6.33	-4.29
^{130}Te $\rightarrow$ ^{130}Xe	1.83	5.92	-4.09
^{136}Xe $\rightarrow$ ^{136}Ba	1.52	5.07	-3.55

contribution to the NME which is diagonal in s. The cancelling parts with $J > 0$ comes mostly from $\Delta s = 4$. The matrix elements of the form ${}_f\langle s|\hat{M}|s\rangle_i$ get smaller as s grows and can be considered roughly proportional to $s_m - s$. On the other hand, the cross terms ${}_f\langle s+4|\hat{M}|s\rangle_i$ are roughly constant. In Table 5.2 we show the decomposition of the NME, according to Eq. (5.3). for the $A = 82$ transition.

If we look into detail to the two body matrix elements of the operator $\hat{M}$, we find that the $J = 0$ components resemble to those of the isovector pairing or the realistic nuclear effective interactions. This explains that the $0\nu\beta\beta$ decay acts as a pair-counter. At present we do not have a similarly simple explanation for the behaviour of the $J > 0$ terms.

In view of these results, the maximum value of the NME, corresponding to the most favourable $0\nu\beta\beta$ transition would be that of a pure superfluid nucleus, whose wave function is purely $s = 0$, into another superfluid one. In this case, the $J = 0$ contribution would be maximized, vanishing the cancelling terms.

Therefore, the results highlight the role of the seniority structure of the nuclear wave functions in the buildup of the $0\nu\beta\beta$ NME. We can see more clearly this fact in Figure 5.2, where we have plotted the value of the NME as a function of the

Table 5.2: Decomposition of the $0\nu\beta\beta$ NME as a function of the seniority components of the initial, s_i, and final, s_f, wave functions. Results for the $A = 82$ decay. The coefficients in parenthesis indicate the percentage of the wave function that belongs to this particular seniority.

	$s_f = 0$ (44)	$s_f = 4$ (41)	$s_f = 6$ (6)	$s_f = 8$ (8)	$s_f = 10$ (1)	$s_f = 12$ (0.1)
$s_i = 0$ (50)	8.8	-5.6	-	-	-	-
$s_i = 4$ (39)	-0.3	4.9	-1.2	-6.2	-	-
$s_i = 6$ (10)	-	-0.2	2.2	-0.3	-3.0	-
$s_i = 8$ (1)	-	-0.02	-0.07	0.6	-0.08	-4.3

maximum value of the seniority, s_m, allowed in the wave functions. The values with maximum seniority provide the exact ISM result in the corresponding valence spaces, already presented in Chapter 4.

We can draw several conclusions from this Figure. Firstly, as was pointed out by the analysis of the decomposition of the value of NME as a function of the decaying pair, we see that the NME value is strongly reduced as the maximun allowed seniority increases.

More importantly, we see that, at the $s_m = 4$ level, two different behaviours appear. On the one hand, for $A = 76$, 82, 128 and 130 the value of the NME is still far from converged, missing a factor 2-3. On the other hand, the convergence of $A = 48$, 124 and 136 is almost achieved. The reason why this happens like this is very illuminating. The nucleus ^{124}Sn has only neutrons in the valence space. Hence, its wave function is dominated by low seniority components and consequently at $s_m = 4$ the NME is quite close to the exact result. In $A = 136$, the calculation for ^{136}Xe with $s_m = 4$ is exact. This is the reason for its nearly converged value at this level. Finally, in the case of $A = 48$, the $s > 4$ components of the wave function are negligible in doubly magic ^{48}Ca, —also very small in ^{48}Ti, specially those with $s = 8$— therefore entailing a NME at $s_m = 4$ which is almost

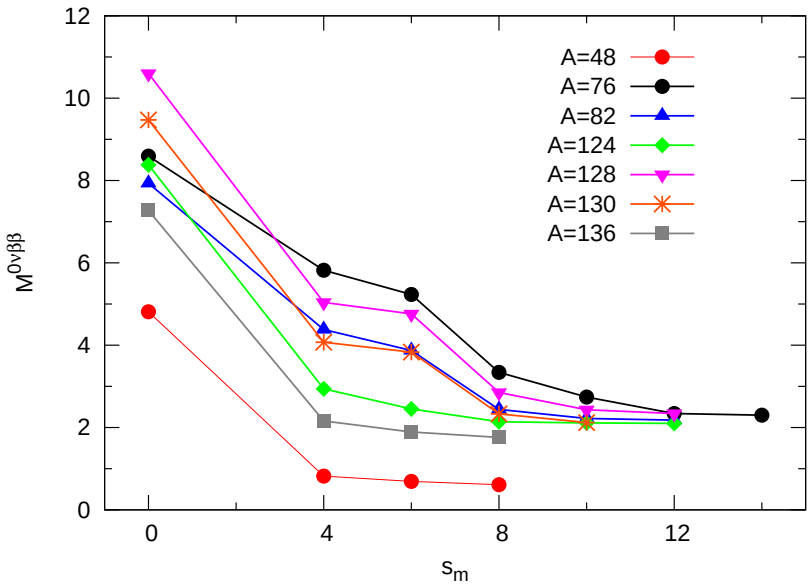

Figure 5.2: Evolution of the NME of the 0νββ decay with the maximum seniority allowed in the wave functions

converged.

This is, wee see that whenever high seniority components of the wave functions are important, the NME is sensitive to the maximum allowed seniority in the wave functions. In Chapter 4 we saw that there were substantial differences between ISM and QRPA NME results. We may wonder to which point QRPA wave functions, being built on top of a purely BCS solution, include these high seniority components, and whether this may be relevant to their evaluation of the NME. To study this point, in Figures 5.3 and 5.4 we plot again, for the case of Jastrow and UCOM type SRC's, the ISM and the QRPA values but, this time, we include the ISM values at the $s_m = 4$ level.

From both figures the same conclusion can be achieved. The $s_m = 4$ results are in general larger than the QRPA final values, but in any case quite close to the corresponding $g_A(0) = 1.25$ figures —top of the QRPA bars. The exception to this rule is the $A = 136$ case, which is one the examples mentioned above for which the high seniority components for the NME where small. In addition to this, the $A = 124$ number obtained in a preliminary calculation with the Jastrow

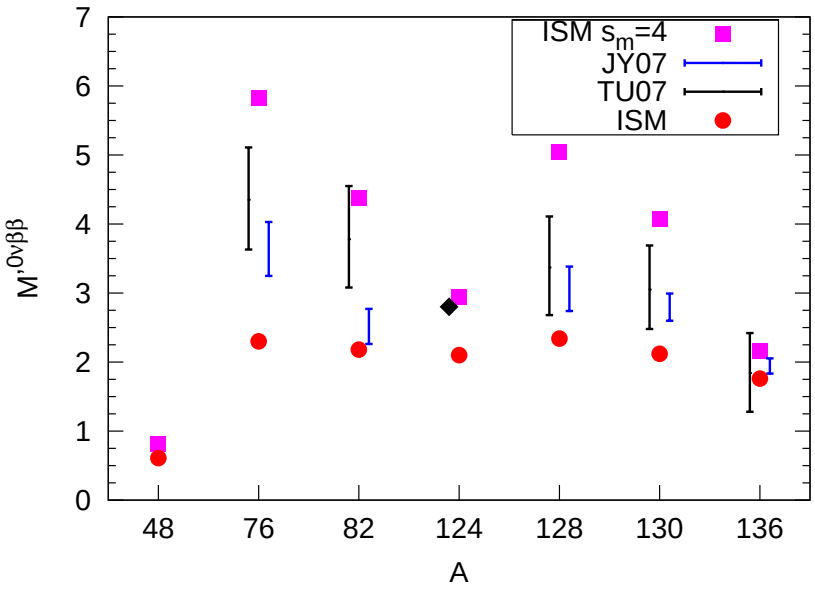

Figure 5.3: The neutrinoless double beta decay $M'^{0\nu\beta\beta}$'s for ISM, ISM with truncated maximum seniority $s_m = 4$, and QRPA calculations, treating the SRC's with the Jastrow approach. Tu07 QRPA results from Ref. [166] and Jy08 results from Ref. [167]. The $A = 124$ QRPA result from Ref. [180].

prescription, also points out in this direction.

This suggests that, somehow, there is an implicit seniority truncation inherent to QRPA calculations. In other words, it seems that QRPA may not take completely into account high seniority components of the wave functions. This view is supported by the structure of the QRPA solutions, whose correlated ground state can be written as:

$$|QRPA\rangle = N_0 e^S |BCS\rangle \,, \tag{5.4}$$

where,

$$S = \sum_{abcd} C_{abcd} A^\dagger_{ab} \widetilde{A}^\dagger_{cd}, \tag{5.5}$$

with $A^\dagger$ two quasiparticle creation operators and C's certain coefficients depending

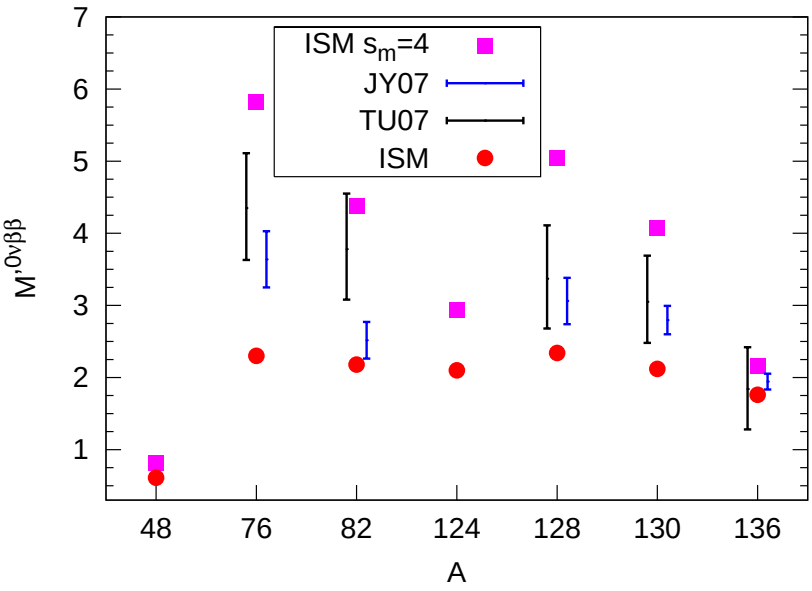

Figure 5.4: Same as Figure 5.3 but with UCOM type SRC's. Tu07 QRPA results from Ref. [168] and Jy07 results from Refs. [165, 169].

on the QRPA equations.

As can be seen from Eq. (5.4), the expansion of the $|QRPA\rangle$ ground state includes on top of the $|BCS\rangle$ vacuum $4n$ quasiparticle excitations, which means seniority components up to $4n$, with $n = 1, 2...$

However, in order for the QRPA to make sense, the C coefficients must be small and therefore higher seniority components will be suppressed. This is, the leading correction to $|BCS\rangle$ has only up to s =4 components, and the contributions of $s = 6, 8$ are corrections to next order of this result.

As a result, we surmise that the QRPA results overestimate the contribution of $s = 0$ components of the wave functions by underestimating those of high seniority components. Hence a too large NME value may be obtained. The extent of this overestimation depends on the degree of validity of a low seniority approximation in each transition. In Table 5.3 we have shown the seniority structure of the wave functions relevant to the decays studied. We can see that in the $A = 48$, 124 and 136 cases this approximation takes into account almost the complete wave functions. However, in the other cases high seniority component are required to obtain

Table 5.3: Decomposition of the wave functions in function of the seniority components for the nuclei studied. Results in percentage.

	$s=0$	$s=4$	$s=6$	$s=8$	$s=10$	$s=12$	$s=14$
^{48}Ca	97	3	-	-	-	-	-
^{48}Ti	59	36	4	1	-	-	-
^{76}Ge	43	41	7	8	1	-	-
^{76}Se	26	41	11	16	4	1	-
^{82}Se	50	39	10	1	-	-	-
^{82}Kr	44	41	6	8	1	-	-
^{124}Sn	95	5	-	-	-	-	-
^{124}Te	60	33	6	2	-	-	-
^{128}Te	70	26	3	1	-	-	-
^{128}Xe	37	41	9	10	2	-	-
^{130}Te	79	20	1	-	-	-	-
^{130}Xe	46	39	7	7	1	-	-
^{136}Xe	97	3	-	-	-	-	-
^{136}Ba	72	25	2	1	-	-	-

a detailed description of the wave functions. For instance, $s=4$ components are comparable and can be even larger than $s=0$ one —namely in ^{76}Se and ^{128}Xe—, while $s>4$ components amount up to 15-30% of the full wave function.

5.2.2 Pairing and the Fermi and Tensor components

Another aspect of the NME that could be sensitive to the amount of pairing like correlations in the wave functions is the ratio of Fermi to Gamow-Teller terms. In Chapter 4 it was already noticed that the contribution of the Fermi part was over-

Table 5.4: Evolution of $-\chi^F$ as a function of the maximum seniority allowed in the wave functions, s_m, for all the studied $0\nu\beta\beta$ decays.

s_m	$A=48$	$A=76$	$A=82$	$A=124$	$A=128$	$A=130$	$A=136$
0	0.33	0.31	0.30	0.27	0.27	0.27	0.26
4	0.19	0.23	0.21	0.15	0.20	0.19	0.15
6	0.17	0.22	0.20	0.16	0.20	0.19	0.16
8	0.16	0.16	0.13	0.15	0.16	0.15	0.15
10		0.14	0.12	0.15	0.15	0.15	
12		0.12	0.11	0.15	0.15		
14		0.12					

estimated in QRPA calculations in comparison to ISM results. We can study this relation by means of the coefficient $\chi^F = \left(\frac{g_V(0)}{g_A(0)}\right)^2 M^F/M^{GT}$, represented in Table 5.4 for all the studied nuclei as a function of the seniority. Like in the precedent case, here we see that correlations affect in a different manner to these contributions, in such a way that the ratio χ^F decreases as we allow higher seniority components in the wave functions. This trend is not seen, however, in the $A=48$, $A=124$ and $A=136$ cases. But these are precisely the nuclei for which the low seniority truncation works better [154], being emitters which, in their natural valence spaces, only consist on neutrons —^{48}Ca and ^{124}Sn— or protons —^{136}Xe—, leading to wave functions dominated by low seniority components. We compare our full results and those truncated in seniority with the QRPA figures in Table 5.5, observing that ISM χ^F values are smaller than QRPA's, but the truncated $s_m=4$ results are always closer to them. This is to say, one may attribute, at least partially, the discrepancy in χ^F between ISM and QRPA to the seniority truncations, as was the case for the complete NME.

On the other hand there is also the role of tensor part of the NME, which we can quantify similarly to the Fermi case by the ratio to the Gamow-Teller contribution,

Table 5.5: Comparison of the values of χ^F of this work (ISM), this work with truncated seniority $s_m = 4$ and the QRPA results of the Jyväskylä (JY07) [165, 169] and Tübingen (TU07) groups [159]. The TU07 result is taken prior to SRC's, see Ref. [166].

$-\chi^F$	ISM	ISM ($s_m = 4$)	JY07	TU07
$^{76}\mathrm{Ge} \rightarrow {}^{76}\mathrm{Se}$	0.12	0.23	0.27	0.32
$^{82}\mathrm{Se} \rightarrow {}^{82}\mathrm{Kr}$	0.11	0.21	0.26	-
$^{128}\mathrm{Te} \rightarrow {}^{130}\mathrm{Xe}$	0.15	0.20	0.31	-
$^{130}\mathrm{Te} \rightarrow {}^{130}\mathrm{Xe}$	0.15	0.19	0.31	0.36
$^{136}\mathrm{Xe} \rightarrow {}^{136}\mathrm{Ba}$	0.15	0.15	0.27	-

$\chi^T = M^T/M^{GT}$. In Section 4.3.1 it was noted that the relevance of this term was controversial, being negligible for the ISM and Jyväskylä groups but important for the Tübingen collaboration. We can study the evolution of the above quantity with the seniority in order to try to shed some light into this issue.

The results are shown in Table 5.6, collected again as a function of the maximum seniority allowed in the wave functions. We can see that, except in the special case of $A = 48$, which shows a quite large ratio, all the other numbers are far from these found in Ref. [159], and could be considered negligible as in Ref. [165]. This remains true although to a slightly lesser extent if we keep only the $s_m = 4$ figures, which are larger than the corresponding complete space values —thus pointing to a similar dependence on the seniority truncation to that of the Fermi component— but still very minor to be significant in the final result.

5.2.3 Pairing and the HOC, FNS and SRC contributions

In Chapter 4 we saw that the relative contributions of HOC, FNS or SRC's are similar for ISM and QRPA calculations. This seems to point out that their contribution to the full NME is not affected by truncations in the seniority of the wave functions.

Table 5.7 confirms this point. On it, partial contributions of HOC, FNS or

Table 5.6: Evolution of χ^T (%) as a function of the maximum seniority permitted in the wave functions, s_m, for all the studied $0\nu\beta\beta$ decays.

s_m	$A=48$	$A=76$	$A=82$	$A=124$	$A=128$	$A=130$	$A=136$
0	3.2	1.6	1.3	0.5	0.6	0.5	0.4
4	9.0	1.0	0.8	0.1	0.0	-0.2	-0.7
6	9.4	0.9	0.9	0.1	0.1	-0.1	-0.6
8	9.9	0.6	0.3	0.1	-0.3	-0.5	-0.6
10		0.6	0.2	0.1	-0.3	-0.5	
12		0.4	0.2	0.1	-0.3		
14		0.4					

SRC's in the NME are shown as a function of the maximum seniority allowed in the wave functions. The ^{76}Ge $\rightarrow$ ^{76}Se $0\nu\beta\beta$ decay is chosen, but the same conclusion is obtained for all other transitions. Even though a small decrease of all the contributions is seen, at the $s_m = 4$ level —which is the leading order in QRPA— the relative values of HOC, FNS and SRC's are essentially that of the full calculation.

5.3 Deformation and the $0\nu\beta\beta$ decay

Deformation is known to play an important role in $2\nu\beta\beta$ decay. The transition is suppressed when the initial and final nuclei show a different deformation [181]. Results pointing in the same direction for $0\nu\beta\beta$ decay have appeared very recently in calculations within the projected Hartree-Fock-Bogolyubov method using a schematic pairing plus quadrupole interaction [182]. The same tendency was found in prior ISM works [153]. Here we will take up again this task and study systematically the effects of deformation of the initial and/or final states in the NME's of the $0\nu\beta\beta$ transitions. There is an extra motivation to pursue this study:

Table 5.7: Evolution of the NME with the maximum seniority (s_m) permitted in the wave functions of ^{76}Ge and ^{76}Se, including different contributions to the full operator.

s_m	M_{bare}	M_{fns}	M_{hoc}	$M_{h.+fns}$	$M^{0\nu\beta\beta}$	$\%_{hoc}^{b/fns}$	$\%_{fns}$	$\%_{src}$
0	12.31	11.16	10.49	9.83	8.59	15/12	6	13
4	8.84	7.87	7.44	6.89	5.82	16/12	7	16
6	8.01	7.11	6.73	6.22	5.23	16/13	8	16
8	5.63	4.90	4.66	4.25	3.34	17/13	9	21
10	4.64	4.00	3.81	3.45	2.74	18/14	9	21
12	4.10	3.50	3.34	3.01	2.34	19/14	10	22
14	4.04	3.45	3.29	2.96	2.30	19/14	10	22

the experimental interest —mainly due to its large $Q_{\beta\beta}$ value— of performing an experiment with ^{150}Nd, a well deformed nuclei that decays into ^{150}Sm, which is barely deformed.

We will study deformation via quadrupole correlations. We need first to decide how to measure the quadrupole correlations of the ground state. Our choice is to refer to the non energy-weighted sum rule:

$$\langle Q^2 \rangle = \sum_i \left| \langle 2_i^+ | Q | 0^+ \rangle \right|^2 \tag{5.6}$$

The operator Q represents the mass quadrupole. "Effective charges" are included in order to obtain the adequate mass quadrupole numbers, this is, those that give the same deformation as the charge quadrupole.

5.3.1 Unphysical mirror $\beta\beta$ decays

We have studied non realistic transitions between mirror nuclei in order to have a clearer view of the role of deformation in the NME's. These transitions have the

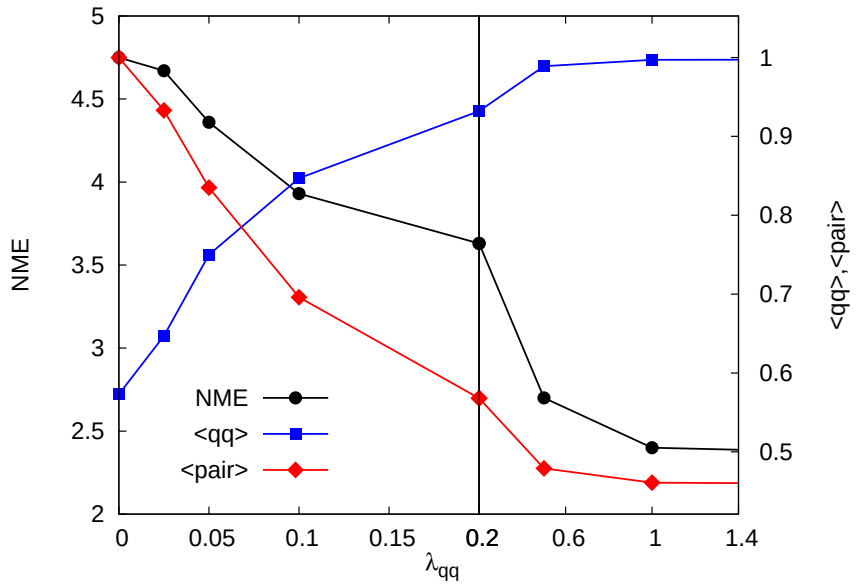

Figure 5.5: Equally deformed ^{66}Ge $\rightarrow$ ^{66}Se NME as a function of the strength of the extra quadrupole-quadrupole interaction. On the right hand y axis the pairing and quadrupole sum rules are represented, normalized so that their maximum value is 1. Note the change of scale in the x axis at $\lambda = 0.2$.

peculiarity that the wave functions of initial and final nuclei are the same and, consequently, the roles of the $0\nu\beta\beta$ operator and of the wave functions in the NME's can be disentangled.

This study has been carried for the 6 valence neutrons and 4 valence protons emitters ^{26}Mg, ^{50}Cr, ^{66}Ge and ^{110}Xe, decaying into the 4 valence neutrons and 6 valence protons nuclei ^{26}Si, ^{50}Fe, ^{66}Se and ^{110}Ba. The valence spaces considered are the *sd* shell, the *pf* shell, the r_3g and the r_4h, respectively, diagonalized —when no additional quadrupole interaction is considered— with the USD, KB3, GCN28.50 and GCN50.82 interactions. Extra quadrupole correlations are enforced into these by the addition to the reference effective Hamiltonians of a quadrupole-quadrupole term $\lambda_{qq}\, Q\cdot Q$, whose effect will be gauged by its influence in the sum rule of Eq. (5.6). Calculations have been done from the initial case $\lambda_{qq} = 0$ up to the limit of pure quadrupole-quadrupole interaction —$\lambda_{qq} \rightarrow \infty$.

The results for $A = 66$, in which the deformations of initial and final nuclei

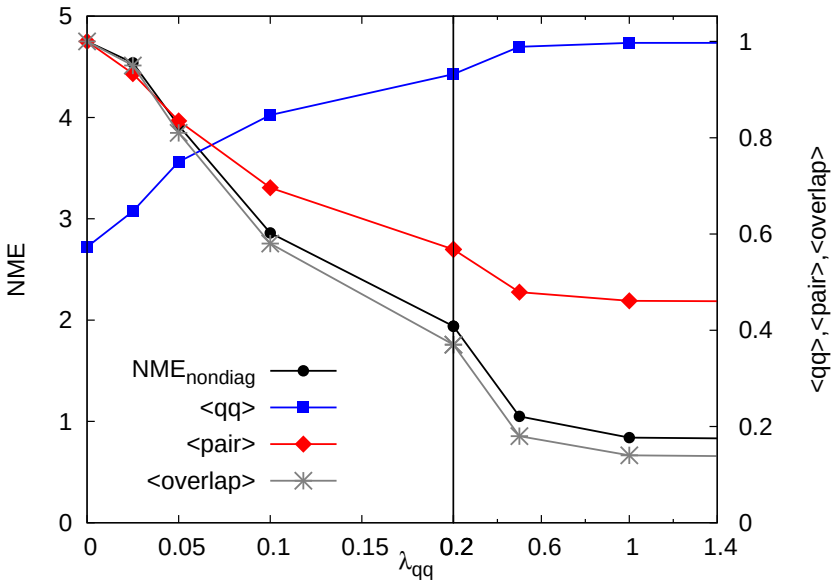

Figure 5.6: Same as Figure 5.5, but now the only nucleus calculated with additional quadrupole interaction is ^{66}Se. The normalized overlap between initial and final states is also included.

are the same, are shown on Figure 5.5. There we see that, as nuclei become more deformed, the NME and the pairing content of the wave function get smaller, while the quadrupole sum rule grows. All these changes are nearly linear for reasonable deformations and then a saturation result is approached more smoothly. Note that the purely quadrupole interaction gives a NME which is about a half of the value obtained with no additional quadrupole.

Figure 5.6 shows the same as Figure 5.5 but now only the final nucleus has been artificially deformed by adding an extra quadrupole-quadrupole term. In addition, the overlap between initial and final wave functions has been included. We see that now the reduction of the NME is more pronounced and, more interesting, that it follows closely the overlap between wave functions. This means that, taking the folowing composition of the final wave function: $|\Psi\rangle = a|\Psi_0\rangle + b|\Psi_{qq}\rangle$, when considering the 0νββ operator and hence the NME, only the first part contributes.

The behaviour of the NME's with respect to the difference of deformation between parent and granddaughter is common to all the other transitions between

mirror nuclei that we have studied. Therefore, this can be submitted as a robust result. However, when considering the transitions between equally deformed nuclei, the evolution of the NME's with the deformation found in the $A = 66$ case is only shared by $A = 110$. When the valence space is a full major oscillator shell —$A = 26$ and $A = 50$— the situation is quite different. Indeed, what is observed is that the NME does not decrease for moderate values of λ_{qq} but remains rather constant until a point —with large deformation— where its value increases significantly —up to 50%. This is due to the fact that, at this point, the major contribution to the NME ceases to come only from the decay of pairs coupled to $J = 0$ —which is the usual case, studied in Section 5.2.1— since other values like $J = 2, 4, 6$, which usually have a contribution to the NME contrary to that of $J = 0$, reverse sign and grow until being comparable with this contribution, thus resulting in this notorious rise of the NME. In the *sd* and *pf* major shells, the $\lambda_{qq} \to \infty$ limit is equivalent to Elliott's SU(3) limit, and the fact that both the initial and final nuclei should belong to the same irrep of SU(3) may be the reason of the increase of the NME. In any case, for the moment we have not found a formal explanation.

We have plotted the evolution of the J^π components of the Gamow-Teller part of the $0\nu\beta\beta$ decay NME as a function of the amount of quadrupole-quadrupole interaction added to the interaction. In Figure 5.7 we have the standard case represented by $A = 66$. The dominant 0^+ component of the transition is strongly reduced when the quadrupole-quadrupole interaction is increased. In Figure 5.8 the situation for $A = 50$ is represented. We can observe the change of sign of the $J > 0$ contributions, that overcome the reduction of the 0^+ component and make M^{GT} larger.

Very similar conclusions may be reached for the effect of deformation in $2\nu\beta\beta$ decay. For instance, the mirror nuclei diagonal and non-diagonal NME's are represented as in the $0\nu\beta\beta$ case in Figures 5.9 and 5.10 for the $A = 66$ transition. We see that the figures resemble very much that of the $0\nu\beta\beta$, with the only exception that, in the equally deformed case, the lowering of the NME due to deformation is more pronounced. In this sense, deformation seems to affect similarly to $0\nu\beta\beta$ and $2\nu\beta\beta$ decays.

A much more complete study of the effect of deformation on the $0\nu\beta\beta$ decay NME of these mirror nuclei can be performed, considering at the same time extra

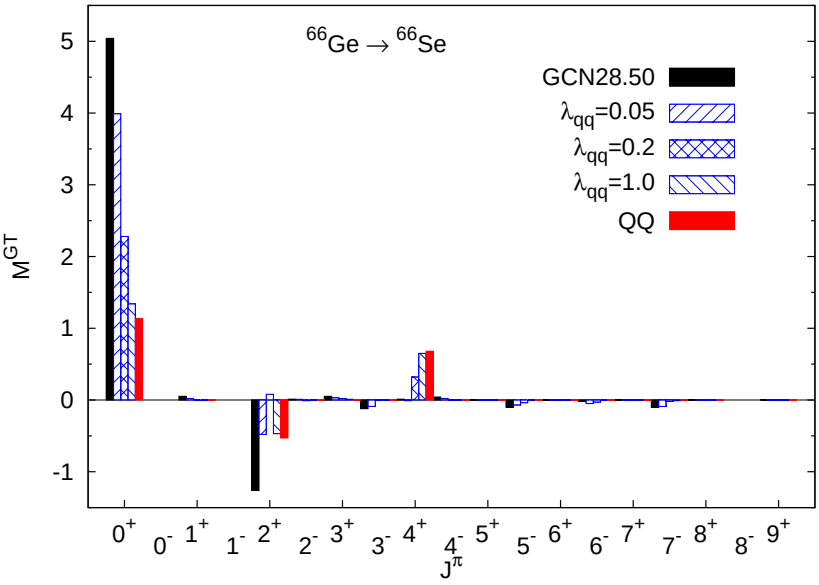

Figure 5.7: Contributions to the Gamow-Teller component of the NME as a function of the J^π of the transformed pair for the fictitious mirror ^{66}Ge → ^{66}Se transition. Evolution of each component as extra quadrupole-quadrupole interaction is added to the Hamiltonian, from the original interaction (black) to full quadrupole-quadrupole interaction (red).

quadrupole-quadrupole correlations, of equal or different strength, in the initial or final nuclei. In Figure 5.11 we have represented the variation of the value of the NME with the quadrupole-quadrupole correlations of the initial and final nuclei.

In this case, we have tried not only to enhance but also to reduce the value of the quadrupole correlations of the wave functions. This was done, in analogy with the previous experience, by adding to the Hamiltonian a term of the form $\lambda_{pp}\, P \cdot P$, where $P \cdot P$ is the pairing interaction. As has been shown, the effect of these two type of correlations on the NME is opposite, pairing like correlations giving larger NME values and quadrupole correlations suppressing them. Hence, for reasonable values of λ_{pp} pairing correlations compete with quadrupole ones, reducing the quadrupole content of the wave functions.

Since both wave functions are the same, the Figure is symmetric. The green

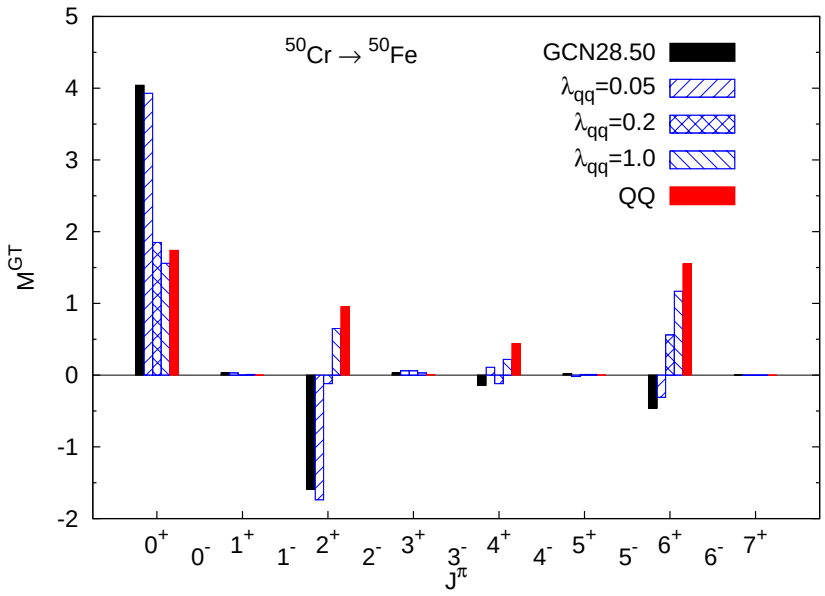

Figure 5.8: Same as Figure 5.7 but for the $^{50}Cr \rightarrow {}^{50}Fe$ transition.

points represent the actual calculated points for which the interaction is the same for the initial and final points. From these and the non-diagonal results the rest of the graphic is extrapolated. The original value of the quadrupole-quadrupole correlations is $\langle Q^2 \rangle = 5500$ fm^4.

We see that, as was already noted in Figure 5.5, the diagonal value of the NME is reduced as the quadrupole-quadrupole correlations are increased. In addition, it is seen now that the same effect happens if these correlations are reduced.

Another point that is confirmed is that of Figure 5.6, where it was pointed out that the NME is suppressed when there is different quadrupole deformation in the final and initial nuclei. Again, the reduction of the NME follows very well the pattern of the overlap of the wave functions. This can be more clearly observed with the help of Figures 5.12 and 5.13. The normalized NME and the overlap are represented, respectively. As expected, both figures are very similar, showing maximum value of the NME where that appear where the overlap between wave functions is also maximum. This establishes the robustness of the fact that only

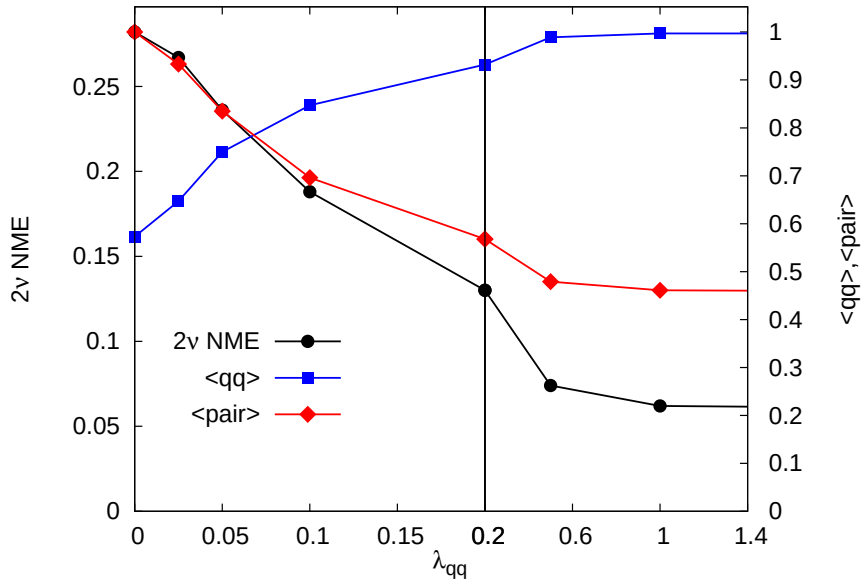

Figure 5.9: Equally deformed ^{66}Ge $\rightarrow$ ^{66}Se 2νββ NME as a function of the strength of the extra quadrupole-quadrupole interaction.

the components of the wave function with the same deformation contribute to the NME.

5.3.2 Real 0νββ decays

In the same fashion we can now study the effect of deformation in the actual 0νββ decays. With the same definitions as before, the evolution of the NME's as a function of the quadrupole-quadrupole correlations inherent to the initial and final wave functions is shown, in Figures 5.14, 5.15 and 5.16, for the ^{76}Ge $\rightarrow$ ^{76}Se, ^{82}Se $\rightarrow$ ^{82}Kr and ^{136}Xe $\rightarrow$ ^{136}Ba decays, respectively.

A number of differences appear in comparison with the $A = 66$ case. First of all, the symmetry of the picture is lost, since now the proton and neutron spaces are not symmetric. For the same reason in this realistic cases it is not possible to calculate the overlap between the initial and final nuclei[1].

[1] Strictly speaking, what was calculated was not the overlap between initial and final wave functions, but that of, say, the initial wave function and the one correspondent, for the initial nucleus, to

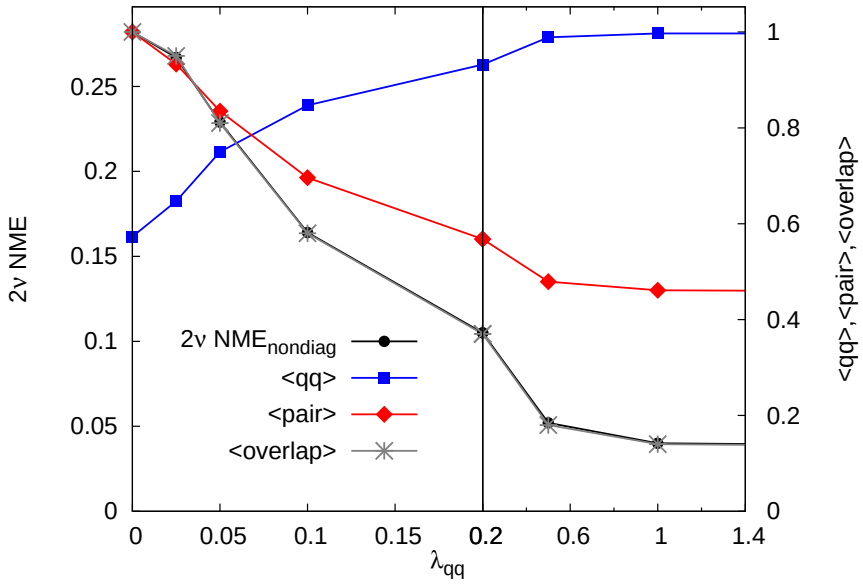

Figure 5.10: Same as Figure 5.9, but now the only nucleus calculated with additional quadrupole interaction is ^{66}Se. The normalized overlap between initial and final states is also included.

As a consequence, one of the two nuclei has initially more quadrupole-quadrupole correlations than the other. Moreover, one of them will also accept correlations more easily —as a rule, this nucleus is, in both cases, the final one. The $A = 82$ and $A = 136$ decays are very representative, since relatively moderate values of λ_{qq} enhance significantly the deformation of the final nuclei while leaving nearly constant the initial nucleus counterpart. When this is the case, it is seen that the NME is drastically reduced: large differences of "deformation" entail a suppression of the NME.

For instance, for $A = 136$, a 50% increase in the quadrupole correlations in ^{136}Ba nearly halves the value NME, almost regardless of small quadrupole-quadrupole enhancement in ^{136}Xe. On the contrary, a 50% increase in ^{136}Xe, coming closer to the ^{136}Ba $\langle Q^2 \rangle$ value, does not lower the NME, with the condition that the enhance-

the λ_{qq} parameter used to obtain the final one. Since initial and final nuclei were mirrors, their wave functions, for the same value of λ_{qq} are identical, except for the proton-neutron asymmetry. Hence, this overlap could be safely interpreted as the overlap between initial and final wave functions.

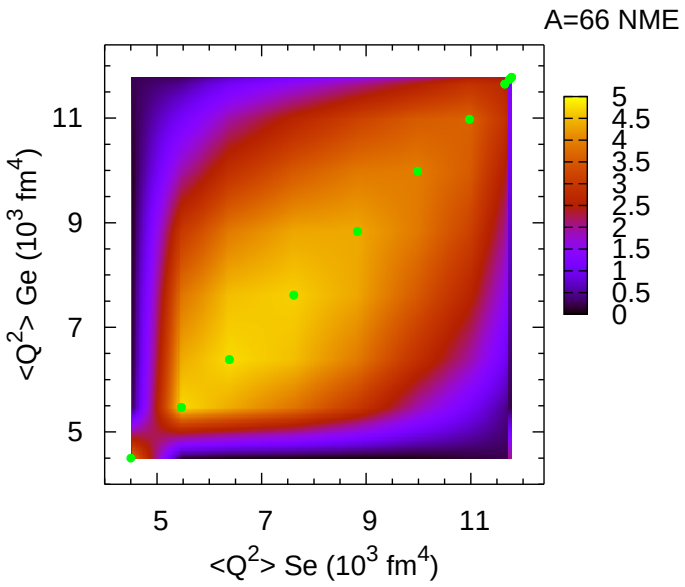

Figure 5.11: Evolution of the 0νββ NME of the ^{66}Ge $\rightarrow$ ^{66}Se transition with the quadrupole-quadrupole correlations of ^{66}Ge and ^{66}Se. The units of $\langle Q^2 \rangle$ are fm^4. Explanation in the text.

ment keeps reasonable. For $A = 82$ the situation is similar but not so transparent in the picture due to the not so different initial quadrupole correlations of the two nuclei involved.

However, the difference in quadrupole-quadrupole correlations does not directly determine the value of the NME. In Figure 5.14 we see that, for $A = 76$, there is a clear tendency in the NME to be maximized when the initial and final nuclei have been calculated with the same interaction. For instance, originally $\langle Q^2 \rangle = 10100$ fm^4 for ^{76}Se. and $\langle Q^2 \rangle = 7300$ fm^4 for ^{76}Ge. If the latter is risen up to the ^{76}Se value, the NME is not increased, but is slightly reduced. This points to a conclusion similar to that the previous Section, where we saw that the NME followed closely the behaviour of the overlap between the initial and final wave functions —which, of course, was maximized when both were calculated with the same interaction. An extreme case correspond to the almost zero value of the NME that is found in the cases when one nucleus is dominated by the pairing Hamiltonian and the other by the quadrupole one. In this cases, with wave functions of

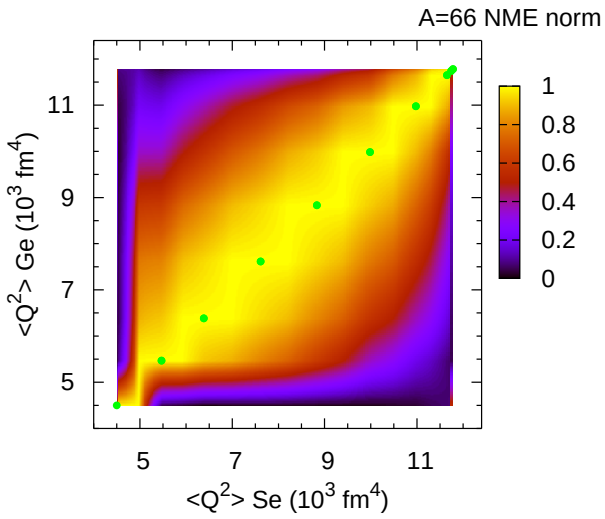

Figure 5.12: Evolution of the normalized $0\nu\beta\beta$ NME of the ^{66}Ge $\rightarrow$ ^{66}Se transition with the quadrupole-quadrupole correlations of ^{66}Ge and ^{66}Se. The units of $\langle Q^2 \rangle$ are fm^4.

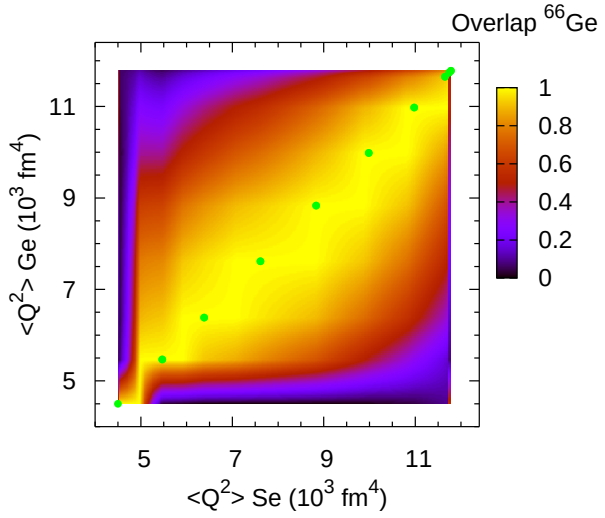

Figure 5.13: Evolution of the overlap of the wave functions in the ^{66}Ge $\rightarrow$ ^{66}Se transition with the quadrupole-quadrupole correlations of ^{66}Ge and ^{66}Se. The units of $\langle Q^2 \rangle$ are fm^4. Explanation in the text.

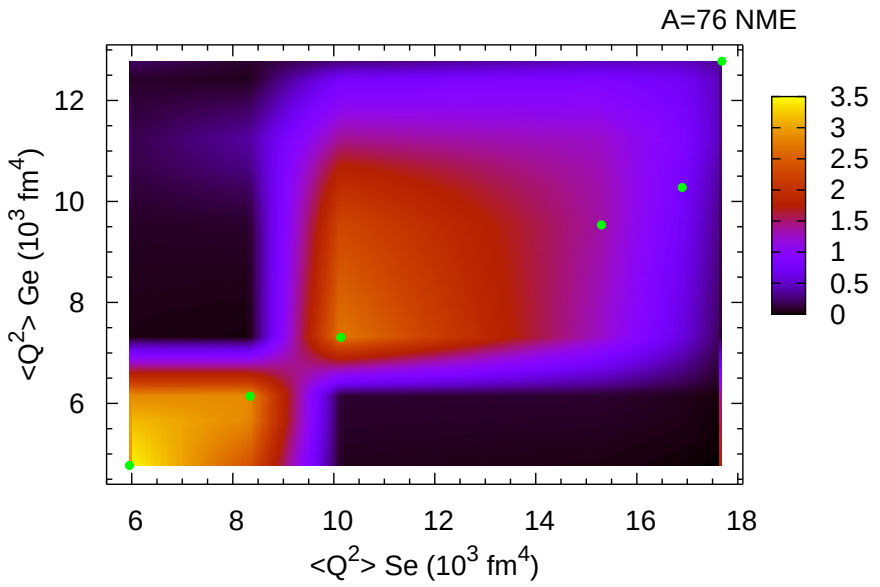

Figure 5.14: Evolution of the ^{76}Ge $\rightarrow$ ^{76}Se 0νββ NME with the quadrupole-quadrupole correlations of ^{76}Ge and ^{76}Se. The units of $\langle Q^2 \rangle$ are fm^4. The true values correspond to $\langle Q^2 \rangle = 7300$ fm^4 and $\langle Q^2 \rangle = 10100$ fm^4 for ^{76}Ge and ^{76}Se, respectively.

completely opposite nature, the NME can not but vanish.

Finally, we also observe in Figures 5.14, 5.15 and 5.16 that, as a general rule, the NME is suppressed as we increase the value of the quadrupole-quadrupole correlations, thus confirming the findings of the previous Sections. Furthermore, for $A = 76$, for which the original quadrupole correlations can be reduced more efficiently, we see that the NME is definitely enhanced when the main component of both wave functions is pairing, in concordance with Section 5.2.

5.3.3 Pairing and deformation

Another relevant issue is the combined role of pairing and deformation. It has already been discussed in Section 5.2 that the pairing interaction favours the 0νββ decay in the sense that pairs coupled to $J = 0$ give the main contribution to the transition. Consequently, truncations in seniority, not including the cancellation caused

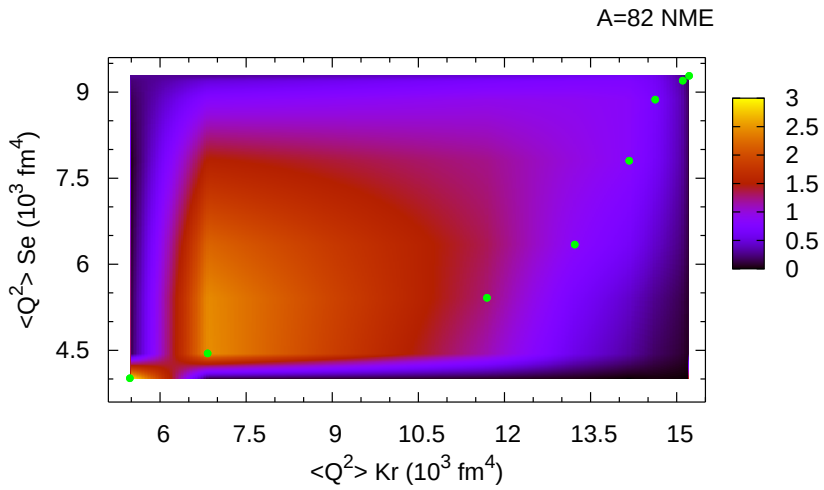

Figure 5.15: Evolution of the $0\nu\beta\beta$ NME of the ^{82}Se $\rightarrow$ ^{82}Kr decay with the quadrupole-quadrupole correlations of ^{82}Se and ^{82}Kr. The units of $\langle Q^2 \rangle$ are fm^4. The true values correspond to $\langle Q^2 \rangle = 4500$ fm^4 and $\langle Q^2 \rangle = 6800$ fm^4 for ^{82}Se and ^{82}Kr, respectively.

by the missing uncoupled pairs, tend to overestimate the value of the NME's.

When studying the unphysical decay of mirror nuclei in Figures 5.5 and 5.6 the pairing content —essentially, the number of pairs— of the wave functions was also represented, showing a reduction, in the same direction as the NME, when the wave functions gained quadrupole correlations. It is easy to understand this fact, since well deformed wave functions will be composed mainly of high seniority components which, as we studied in Section 5.2.1, tend to reduce the value of the NME. Hence, the number of pairs —represented by the $s = 0$ component of the wave functions— are also decreased as we add deformation to our system.

We can now study in further detail the interplay between both pairing and deformation, this is, to which extent a wave function in the laboratory frame, truncated in seniority, can capture the correlations induced by the quadrupole-quadrupole part of the nuclear interaction, and its eventual influence in $0\nu\beta\beta$ NME's.

Using ^{82}Kr as our test bench, we proceed to compute $\langle Q^2 \rangle$, first with our standing effective interaction and different seniority truncations. The results are drawn in Figure 5.17 as the black circles labeled $\lambda_{qq} = 0$. We can see that at $s_m = 4$ —the

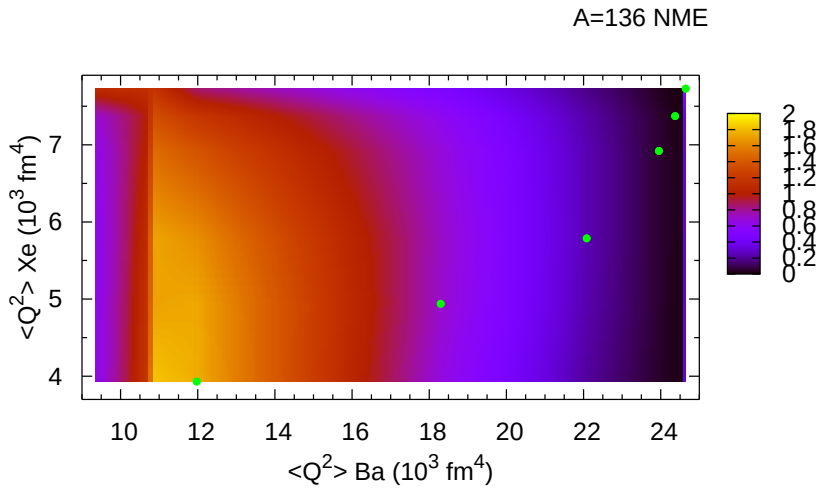

Figure 5.16: Evolution of the 0νββ NME of the ^{136}Xe $\rightarrow$ ^{136}Ba decay with the quadrupole-quadrupole correlations of ^{136}Xe and ^{136}Ba. The units of $\langle Q^2 \rangle$ are fm^4. The true values correspond to $\langle Q^2 \rangle = 3900$ fm^4 and $\langle Q^2 \rangle = 12000$ fm^4 for ^{136}Xe and ^{136}Ba, respectively.

QRPA leading order— some 70% of the full quadrupole correlations are incorporated in the wave function. We would like to know how this behaviour evolves when more quadrupole correlations are enforced in the system, so we again add a quadrupole-quadrupole term to the interaction. To have an idea of the relevant range of values of $\langle Q^2 \rangle$ in this nucleus and valence space, we can see that the limit of pure quadrupole-quadrupole interaction with degenerate single particle energies is $\langle Q^2 \rangle \approx 15200$ fm^4, according to Figure 5.15. The results for $\lambda_{qq} = 0.025$ and $\lambda_{qq} = 0.05$ are also shown in Figure 5.17. It is evident in the figure that, as we try to increase the correlations, the $s_m = 4$ truncation becomes more and more ineffective. For $\lambda_{qq} = 0.025$, only 57% of the exact correlations are present, and for $\lambda_{qq} = 0.05$ only 50%. The situation is different for ^{82}Se: while for $\lambda_{qq} = 0$ the values of $\langle Q^2 \rangle$ as a function of seniority are similar, albeit a bit smaller than the ^{82}Kr ones, for $\lambda_{qq} = 0.025$ and $\lambda_{qq} = 0.05$ there is scarcely any increase of the ground state correlations, as can be seen in Figure 5.15. This means also that, as we increase λ_{qq}, the "deformation" of ^{82}Kr grows, whereas that of ^{82}Se remains constant.

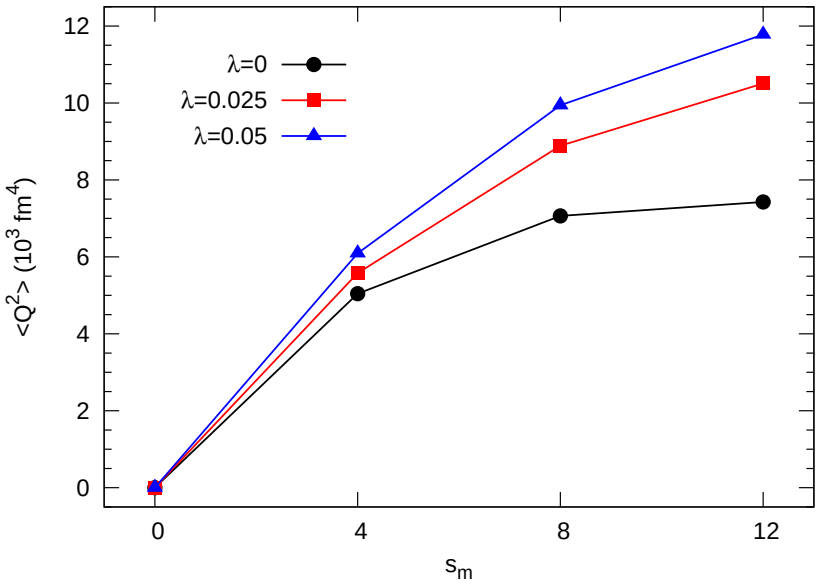

Figure 5.17: Quadrupole correlations in the ground state of ^{82}Kr as a function of the amount of quadrupole-quadrupole interaction $\lambda_{qq}\, Q\cdot Q$ added to the Hamiltonian, for different values of the maximum seniority s_m permitted in the wave functions.

This behaviour offers us the opportunity of exploring the effect of difference in deformation between father and granddaughter in the $0\nu\beta\beta$ NME's and its interplay with seniority truncations of the wave functions. To this goal, we compute the Gamow-Teller matrix element for different values of λ_{qq} —the amount of extra quadrupole-quadrupole interaction— and s_m —the maximum seniority permitted in the wave functions. The results are gathered in Figure 5.18. For $s_m = 0$, we observe that the Gamow-Teller matrix element grows as a function of λ_{qq}. This is because, at this seniority truncation, the only effect of adding quadrupole-quadrupole interaction is to augment the pairing content of the wave functions, thus increasing M^{GT}. At $s_m = 4$, M^{GT} remains constant as a function of λ_{qq}, meaning that the minor increase of the correlations of ^{82}Kr, that we have shown in Figure 5.17, is barely enough to compensate the increase of M^{GT} at $s_m = 0$. On the contrary, as we have already remarked, the full space results are sensitive to the difference in deformation —or, to be more precise, to the difference in the level of quadrupole correlations in the ground state— between father and granddaughter, reducing the

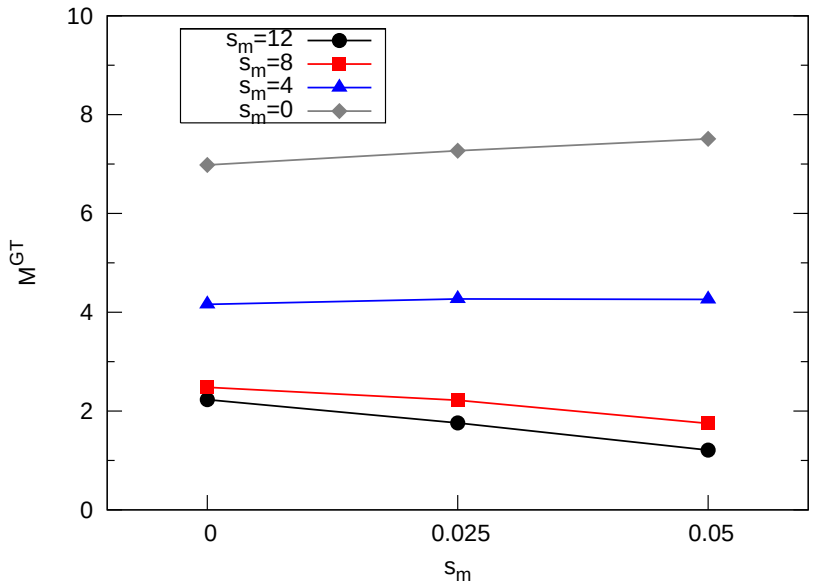

Figure 5.18: ^{82}Se $\rightarrow$ ^{82}Kr Gamow-Teller matrix element, M^{GT}, as a function of the maximum seniority permitted in the wave functions, calculated for different values of the strength of the extra quadrupole-quadrupole interaction.

value of M^{GT} in the case of different deformations.

5.4 Occupancies on the $A = 76$ 0νββ decay

So far, we have studied the possible role of pairing —seniority structure of the wave functions—, and deformation —quadrupole content— into the 0νββ decay. Another way to test whether the nuclear wave functions that we are using to calculate the NME are appropriate or not would be to compare with some experimental observable. One of the most evident choices to test the validity of the wave functions are the nucleon occupancies.

Very recently, some experimental effort has been devoted to explore this important information for 0νββ decays, and accurate measurements of one nucleon transfer reactions have been performed in order to determine the occupation numbers in valence orbits of the nuclei ^{76}Ge and ^{76}Se [177, 178]. Both neutron and proton occupancies were studied. Therefore, we have the chance to compare these

experimental results with the ISM occupations and, if necessary, detect which modifications would be required in the effective interaction to obtain improved agreement with the experiment.

Indeed, there is another interaction more accurate than the one used so far throughout this work, GCN28.50, for the $A = 76$ region. This is due to the fact that, with this interaction, the nucleus ^{76}Se exhibits a slightly oblate deformation, contrary to the experimental situation, which shows also a small deformation but of prolate nature. With the purpose in mind to cure this discrepancy a new interaction was built, namely the RG.PROLATE interaction [183]. The GCN28.50 interaction was obtained by a global fit to the region comprised by the r_3g valence space. The RG.PROLATE interaction is to be understood as a refinement which is more adequate near the $A = 76$ region. It is based on the GCN28.50 interaction, with minor monopole modifications. To obtain an interaction which is more accurate in a certain region of the valence space is justified in order to get more precision in the value of the resulting NME for the $0\nu\beta\beta$ decay, whose accuracy is of great interest, as has been stressed along Chapters 4 and 5.

In Table 5.8 we compare the experimental occupancies along with the theoretical ones obtained with both the GCN28.50 and RG.PROLATE interactions. The occupancies obtained with the former are quite close to the experiment, specially in the case of ^{76}Ge. However, for ^{76}Se are somewhat further from experiment. These defects are corrected by the RG.PROLATE interaction, whose occupancies for ^{76}Se are almost perfect. The only drawback of this interaction is found on the proton occupancies in ^{76}Ge that slightly overfills the $0g_{9/2}$ orbit against the filling of the *p* orbits. In any case, both interactions compare reasonably well with the experiment, while the RG.PROLATE interaction can be said to fit quite successfully the experimental numbers.

QRPA occupancies deviate more from experiment than our ISM values. In order to cure this discrepancies with the measured occupations, Suhonen *et al.* have artificially modified the single particle energies of their interaction in order to make the neutron occupancies exactly reproduce the experimental values, in both ^{76}Ge and ^{76}Se [184]. After this adjustment they also get very good agreement for the proton occupancies. We stress that the occupancies reported are taken at the BCS level, before the QRPA correlations are included into the calculation.

Table 5.8: Proton and neutron occupation numbers of nuclei ^{76}Ge and ^{76}Se. Experiment from Ref. [177, 178] *vs* theoretical results, obtained for the GCN28.50 and RG.PROLATE interactions.

	$1p_{1/2}$+$1p_{3/2}$	$0f_{5/2}$	$0g_{9/2}$
	Neutrons		
^{76}Ge (exp)	4.87±0.20	4.56±0.40	6.48±0.30
^{76}Ge (GCN28.50)	5.19	5.02	5.79
^{76}Ge (RG.PROLATE)	4.83	4.78	6.39
^{76}Se (exp)	4.41±0.20	3.83±0.40	5.80±0.30
^{76}Se (GCN28.50)	4.86	4.54	4.60
^{76}Se (RG.PROLATE)	4.08	4.06	5.86
	Protons		
^{76}Ge (exp)	1.77±0.15	2.04±0.25	0.23±0.25
^{76}Ge (GCN28.50)	1.70	1.90	0.40
^{76}Ge (RG.PROLATE)	1.34	2.00	0.66
^{76}Se (exp)	2.08±0.15	3.16±0.25	0.84±0.25
^{76}Se (GCN28.50)	2.74	2.27	0.99
^{76}Se (RG.PROLATE)	2.12	2.79	1.08

On the other hand, Šimkovic *et al.* perform an equivalent modification of their single particle energies. However, they do it in such a way that it is not at BCS level that their occupation numbers are adjusted to experiment, but at QRPA level [171]. This is, they find different occupations —which can differ as much as half a particle— for the BCS and QRPA calculations.

In Figure 5.19 we have plotted the experimental occupancies compared to the theoretical ISM —GCN28.50 and RG.PROLATE— and QRPA values —both original and adjusted interactions for the Tübingen and Jyväskylä groups. We can ob-

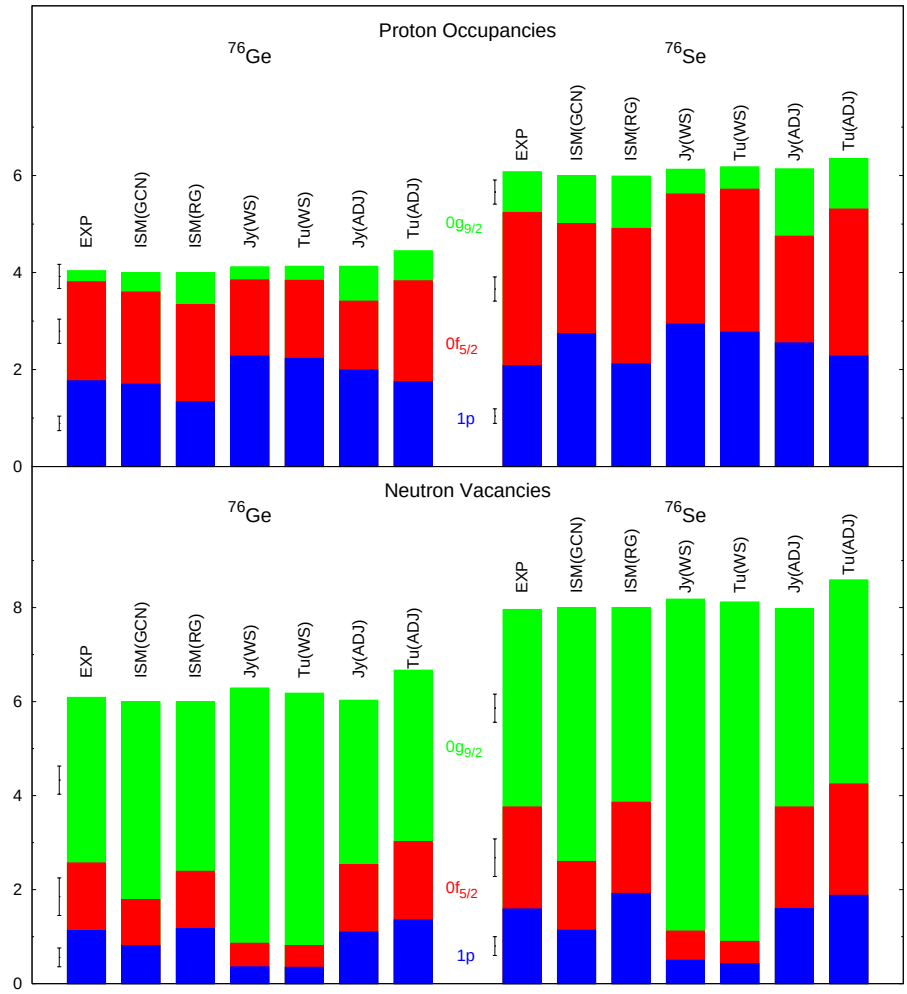

Figure 5.19: Comparison between experimental and theoretical occupation numbers for $A = 76$. Experimental values from Refs. [177, 178]. The ISM values correspond to the GCN28.50 and RG.PROLATE interactions. The QRPA standard numbers, Tu(WS) and Jy(WS) give the occupancies at BCS level. The QRPA occupancies with adjusted single particle energies are given at BCS level in the case of Jy(ADJ) and at QRPA level for Tu(ADJ). Jy(WS) and Jy(ADJ) results from Ref [184], Tu(WS) and Tu(ADJ) values from Ref [171]. The experimental error bars are also shown.

serve that the amount of change in occupancies required to match the experiment is quite large in the case of the QRPA calculations, specially for neutrons. The effect of the new ISM interaction RG.PROLATE is much milder. For each group, their best interaction is able to reproduce the experimental occupations fairly well, with similar accuracies.

Once the interactions have been settled to give results as close as possible to experiment, we can look at the values of the NME's. In Table 5.9 we have collected their values for the ISM and QRPA with the six interactions considered in this Section.

In the case of the Jyväskylä group, the NME suffers a substantial reduction of around 30% when calculated with the adjusted interaction. There is an effect in the same direction, whereas more moderate, present in the Tübingen's results. In this case, the reduction is closer to 20%. These modifications can be traced back to the new values of the QRPA parameters g_{pp} obtained with the modified single particle energies, which are significatively different from those obtained with the Woods-Saxon.

As for the ISM, the NME obtained with the RG.PROLATE interaction is enhanced with respect to the standard one result obtained with GCN28.50. The increase is of some 15%.

Hence, when adjusting the interactions to agree with the measured occupancies in ^{76}Ge and ^{76}Se, the different ISM and QRPA NME values converge. It must be stressed that the Jyväskylä and ISM results are now virtually the same, which is a bit surprising. It may be possible that the fact of adjusting the occupancies at BCS and not QRPA level could be reducing too much the NME, since the decrease found in the case of the Tübingen group is not as marked. This result is still larger than the ISM, but now the gap between QRPA and ISM values is very much reduced. The effects pointed out in previous sections —namely the effect of missing correlations due to lack of high seniority components in the wave functions, for the QRPA, and the truncation of the valence space, for the ISM— may well be responsible for the remaining difference between these NME's.

In summary, even though the ISM occupancies obtained by the GCN28.50 interaction compare reasonably well with experiment, the agreement can be very much improved by use of the RG.PROLATE interaction, which can be considered

Table 5.9: Values of $M'^{0\nu\beta\beta}$ for the ^{76}Ge $\rightarrow$ ^{76}Se decay for ISM and QRPA interactions. Jy (WS) and Tu (WS) are the original QRPA calculations from Refs. [167] (Jastrow), [165] (UCOM), [166] (Jastrow) and [168] (UCOM), while Jy (ADJ) and Tu (ADJ) represent the adjusted interaction to the experimental occupancies, obtained from Refs. [184] and [171]. The non quenched value of the axial coupling, $g_A(0) = 1.25$, is employed. Jastrow and UCOM type SRC's are considered

	$M'^{0\nu\beta\beta}(J)$	$M'^{0\nu\beta\beta}(UCOM)$
ISM (GCN28.50)	2.30	2.81
ISM (RG.PROLATE)	2.70	3.26
Jy (WS)	4.03	5.36
Jy (ADJ)	2.78	4.11
Tu (WS)	4.15-5.11	5.07-6.25
Tu (ADJ)	3.56-4.06	4.59-5.44

as a local modification of the global GCN.28.50 interaction better adjusted to the $A = 76$ region. When calculated, the NME is found to be reasonably stable with respect to this moderate change in the interaction, growing around 15%. On the other hand, the QRPA occupancies lie far from the experimental numbers unless the single particle energies are severely corrected. However, when this is done, the NME is significantly reduced, very much approaching the ISM values. This is, by fitting the interaction in order to improve the agreement with the experimental occupancies in ^{76}Ge and ^{76}Se, a convergence in the NME values is found.

In any case, it needs to be explored to which extent the artificial modification of the single particle energies in the QRPA context, modifying the Mean Field, is appropriate or not, and which is the physical meaning of this modification.

5.5 Summary

In the present Chapter we have continued the thorough study of the Neutrinoless double beta decay started in Chapter 4. In particular, we have studied the effect on the NME's of the pairing and deformation contents of the mother and granddaughter nuclei, by means of the seniority structure and the amount of quadrupole correlations found in their wave functions.

With respect to the first one, it is found that the main contribution to the decay comes from neutrons that are coupled to $J = 0$, being the $J > 0$ contributions in the opposite direction. This leads to the conclusion that the ideal transition will take place between two superfluid nuclei, for which all particles are coupled to $J = 0$. This extreme is confirmed by the calculations performed limiting the number of particles non-coupled to $J = 0$, this is, calculations with truncations in seniority. We see that, as the maximum seniority allowed in the wave functions is increased, the nuclear matrix elements decreases, due to the fact that the wave functions lose part of their coupled-to-$J = 0$ components.

Then, we surmise that QRPA results might be larger than ISM ones because they may not be taking into account completely the high seniority components of the nuclei involved. This hypothesis is supported by the form of the QRPA wave functions altogether with the fact that, for those transitions where the nuclei involved are dominated by low seniority components, the ISM and QRPA results agree.

On the other hand, the effect of deformation on the NME is to reduce its value whenever the deformation of mother and granddaughter nuclei is different. However, to artificially increase the deformation of one of them to match that of the other, is not enough to obtain an increase in the NME. In general, if the two nuclei have different structures coming from different interactions, the NME will also decrease.

Finally we have tested our results with the recent experimental information of occupancies in the case of $A = 76$. In general we find a good agreement to experiment, but we can improve it by designing an specific interaction better adapted to this particular nuclear region. In any case, we end with an NME only 15% larger than that of the original interaction, which stresses the stability of our ISM results.

At the same time, QRPA calculations are considerably reduced when an interaction adjusted to reproduce the experimental occupancies is employed, so in the end the difference between ISM and QRPA NME's is reduced to half the original gap.

Chapter 6

Conclusions and perspectives

In the present work we have seen that, within the Interacting Shell Model framework, we have been able to handle two different Nuclear Structure phenomena: on the one hand, we have explored the shape coexistence of spherical, deformed and superdeformed states in ^{40}Ca; on the other, a thorough analysis of the neutrinoless double beta decay has been performed.

Consequently, the versatility and broad applicability of the method has been illustrated. Actually, it has been equally successfull in giving an excellent description of no less than over 25 states in ^{40}Ca as well as, on the other hand, accurate enough wave functions of the mother and granddaughter nuclei of seven $0\nu\beta\beta$ transitions —namely, the emitters ^{48}Ca, ^{76}Ge, ^{82}Se, ^{124}Sn, ^{128}Te, ^{130}Te and ^{136}Xe, and the final states ^{48}Ti, ^{76}Se, ^{82}Kr, ^{124}Te, ^{128}Xe, ^{130}Xe and ^{136}Ba. Additionally, since the decay to final 0_1^+ states has also been considered, the wave functions of six excited states were obtained as well.

These calculations have been accomplished in different valences spaces —namely, the r_2pf, pf, r_3g and r_4h spaces have been employed— with appropriate effective interactions adapted to each of them. Therefore, a variety of regions in the nuclear chart have been explored. Of course, the limitations of the ISM have constrained the size of the available valence spaces. For instance in the case of ^{40}Ca the natural configuration space would have been the $sd-pf$ space, but we had to model the effects of the $d_{5/2}$ orbit, which is part of the inert core in our calculations, with pairing and monopole modifications on the two body matrix elements

of the r_2pf space. As a drawback, in that case the Center of Mass would have to be treated more carefully, since the two body matrix elements involving the $d_{5/2}$ orbit are quite important. Concerning the $0\nu\beta\beta$ decay, the use of the r_4h space for neutrons and the gr_4 space —*sdg* shell— for protons, still not available for ISM calculations, would permit the study of the transitions for the emitters ^{96}Zr, ^{100}Mo, ^{110}Pd and ^{116}Cd.

In the case of the shape coexistence in ^{40}Ca, we have produced an excellent agreement with experimental data referred to the spherical ground state, the deformed $K = 0$ and γ bands and the superdeformed axial band. Besides, the interband decays have been also very well described in general. In short, we have given a very satisfactory explanation of the nature of these states and the electromagnetic transitions between them, which are usually of the $E2$ type —they are dominant with respect to the $M1$ ones.

Therefore, a possible extension to this work would be to explore other spectroscopic properties of ^{40}Ca. Good candidates for that could be the spectroscopic factors or the Gamow-Teller and magnetic dipole strengths, all the them experimentally known quantities. But probably the most appealing challenge would be the study of the $E0$ transitions between the three 0^+ states, which in addition are directly related to the different sizes —related to the different deformations— of the coexisting configurations. Therefore, additional information about the actual mixing of the three 0^+ states may be obtained, which would very very valuable since, as we remarked, the results presented in Chapter 3 are virtually unchanged with respect to reasonable modifications of the mixing.

As for the the $0\nu\beta\beta$ decay, we have obtained the nuclear matrix elements for the seven transitions enumerated above, and, furthermore, we have studied in detail the relevance of the different terms of the transition operator and the different components of the wave functions.

As a result, we have seen that the ISM predictions for the NME's lie systematically below the QRPA values. After studying the effect of the pair content of the wave functions and of seniority truncations, we have surmised that this disagreement may be caused, at least partially, by the lack, in QRPA calculations, of the complete high seniority components in their wave functions. This point is supported by the fact that for the selected cases that high seniority components or the

wave functions are not relevant, both ISM and QRPA values agree. To clarify this disagreement is of the maximum importance, since a positive $0\nu\beta\beta$ decay signal would require a precise NME in order to obtain valuable information about the mass and hierarchy of the neutrinos.

In the same line, the ISM efforts should be placed in obtaining NME in larger valence spaces, closer to those used in QRPA calculations, in order to estimate the effect of the truncations that are currently required. Some steps have been given in this direction, but much work remains to be done. Additionally, if the decay of ^{96}Zr or ^{100}Mo was calculated, its value could be compared to that of the QRPA. The same can be said for this latter method referred to the decays of ^{48}Ca and ^{124}Sn —up to now only preliminary results for the latter exist.

Another extreme that could be improved in ISM calculations in order to obtain a clearer comparison to the QRPA results would be to go further than the closure approximation. This would allow to obtain the multipole decomposition of the transition, in function of the J^{π} of the virtual intermediate state, which would be directly comparable to the QRPA counterpart.

On the other hand, the recent interest generated by the decay of ^{150}Nd, a well deformed nucleus, into the much less deformed ^{150}Sm, has highlighted the importance of a good description of the role of deformation on the $0\nu\beta\beta$ decay. In the present work we have seen that the transition between differently deformed nuclei is suppressed in comparison to the one between equally deformed one, but also that, in general, a transition between two well deformed nuclei is to be expected less probable than another one involving two spherical nuclei. In any case, further work on this subject remains to be done in order to obtain a precise comprehension of this phenomenon.

In addition to that, an adequate treatment of the short range correlations would be required in order to reduce the uncertainties inherent to the present treatment of the SRC by two alternative methods, the Jastrow or the UCOM prescriptions. As already mentioned in the text, this is a difficult task that would demand the renormalization of the transition operator in the same foot as the Hamiltonian. Work is in progress within the community in oder to clarify this fundamental issue.

Finally, the specialization in certain nuclear regions in order to obtain more precise values for the NME's, as we did in the $A = 76$ case, could also be an inter-

esting possibility, at least in some cases. In particular, for $A = 136$, the $2\nu\beta\beta$ decay has exceptionally large lifetime, and has not been detected yet. It is a challenge to be able to explain such a suppressed value. Since we have learned that deformation hinders the $\beta\beta$ transitions, there might be a connection with the $A = 136$ case.

More complete studies would imply systematic calculation of a wide rank of spectroscopic properties of the nuclei relevant for the $0\nu\beta\beta$ decays —like the one already started for $A = 76$. These will include the occupancies, Gamow-Teller strength distributions, the single beta decays, or the $2\nu\beta\beta$ transition, when available. All these data should give us an idea of the degree of adequacy of a given interaction to a particular decay.

In summary, both the shape coexistence or spherical, deformed and superdeformed states in ^{40}Ca, and the $0\nu\beta\beta$ decay nuclear matrix elements for seven different transitions have been successfully calculated within the ISM framework. Nevertheless, some open questions and improvements remain. As for ^{40}Ca, other properties such as Gamow-Teller and dipole distributions or the $E0$ transitions between the 0^+ states could be explored. Regarding the $0\nu\beta\beta$ decay, the priority is to reconcile ISM and QRPA values for the NME. Performing calculations in larger valence spaces and obtaining the multipole decomposition of the transition would be very helpful in solving these discrepancies. In addition to that, the role of deformation on the NME must be further clarified. Finally, a proper treatment of SRC's or the development of interactions specially devised for certain transitions would reduce the uncertainties of the NME values.

Conclusiones y perspectivas

A lo largo de este trabajo hemos visto cómo, dentro del marco del Modelo de Capas Interactuante, hemos sido capaces de tratar dos fenómenos de Estructura Nuclear muy diferentes: por un lado, hemos explorado la coexistencia de forma entre estados esféricos, deformados y superdeformados en el núcleo ^{40}Ca; por otro, hemos llevado a cabo un detallado análisis de la desintegración doble beta sin neutrinos.

Por tanto, la versatilidad y el amplio campo de aplicación del método han sido puestos de manifiesto. De hecho, hemos visto cómo se ha conseguido una descripción igualmente satisfactoria de, por un lado, nada menos que más de 25 estados del ^{40}Ca y, por otro, una descripción suficientemente precisa de las funciones de onda de los núcleos padre y nieto de siete transiciones $0\nu\beta\beta$ —a saber, las de los emisores ^{48}Ca, ^{76}Ge, ^{82}Se, ^{124}Sn, ^{128}Te, ^{130}Te y ^{136}Xe, más las de los estados finales ^{48}Ti, ^{76}Se, ^{82}Kr, ^{124}Te, ^{128}Xe, ^{130}Xe y ^{136}Ba. Además, como también hemos estudiado las desintegraciones hasta los estados excitados finales 0^+_1, las funciones de onda de seis estados excitados también han sido calculadas.

Estos cálculos han sido realizados en distintos espacios de valencia —en concreto, hemos utilizado los espacios r_2pf, pf, r_3g y r_4h— con interacciones adaptadas a cada espacio. Por tanto, hemos explorado varias regiones de la tabla de núcleos. Por supuesto, las limitaciones del Modelo de Capas han restringido el tamaño de los espacios utilizados en los cálculos. Por ejemplo, en el caso del ^{40}Ca, la configuración natural para abordar el problema habría sido el espacio $sd-pf$, pero durante los cálculos hubo que modelizar el efecto de la órbita $d_{5/2}$, que tenemos que dejar siempre llena, mediante modificaciones en los monopolos y el apareamiento de los elementos de matriz del espacio r_2pf. Como contrapartida, en caso de incluir dicha órbita en los cálculos habría que haber tratado aún con

más cuidado el efecto del centro de masas, ya que los elementos de matriz que incluyen a la órbita $d_{5/2}$ son bastante importantes. En cuanto a la desintegración $0\nu\beta\beta$, el uso del espacio r_4h para neutrones y del gr_4 —capa sdg del oscilador— para protones, de momento demasiado grandes para efectuar cálculos de Modelo de Capas, habría permitido el estudio de las transiciones asociadas a los emisores ^{96}Zr, ^{100}Mo, ^{110}Pd y ^{116}Cd.

En el caso de la coexistencia de forma en el ^{40}Ca, hemos conseguido un excelente acuerdo con los datos experimentales en la descripción del estado fundamental esférico, las bandas deformadas $K = 0$ y γ así como la banda axial superdeformada. Además los resultados obtenidos para las transiciones entre bandas también son bastante buenos en general. Es decir, hemos dado una explicación muy satisfactoria de la naturaleza de estos estados así como de las transiciones electromagnéticas entre ellos, que son de tipo $E2$ —las cuales dominan a las de tipo $M1$.

Por tanto, una posible extensión de este trabajo sería explorar otras propiedades espectroscópicas del núcleo ^{40}Ca. Buenos candidatos serían los factores espectroscópicos o las distribuciones de estructura dipolar magnética o de Gamow-Teller, todas ellas medidas experimentalmente. Sin embargo, probablemente el mayor reto sería dar cuenta de las transiciones de tipo $E0$ producidas entre los tres estados 0^+, las cuales, además, están directamente relacionadas con los diferentes tamaños —que están relacionados con las diferentes deformaciones— de dichos estados coexistentes. Por tanto, así se podría conseguir información adicional sobre la mezcla que hay entre los estados 0^+ de distinta naturaleza. Esta información sería valiosa ya que, como se comentó en el Capítulo 3, los resultados obtenidos quedan prácticamente iguales cuando se varía la mezcla entre dichos estados, siempre y cuando sean variaciones razonables.

En cuanto a las desintegraciones $0\nu\beta\beta$, hemos obtenido los elementos de matriz nucleares para las siete transiciones mencionadas arriba y, además, hemos estudiado en detalle el papel de los diferentes términos del operador de transición y las distintas componentes de las funciones de onda.

Como resultado, hemos visto que los valores del elemento de matriz nuclear obtenidos por el Modelo de Capas son sistemáticamente menores que aquéllos dados por el método de la QRPA. Tras estudiar el efecto del contenido de pares de

las funciones de onda y las truncaciones en “seniority” en dicho elemento de matriz nuclear, hemos propuesto que esta discrepancia podría deberse, al menos en parte, a que, en los cálculos de la QRPA, las componentes de alta “seniority” podrían no estar completamente incluidas. Esta hipótesis está reforzada por el hecho de que, en aquellos casos en que las componentes de alta “seniority” de las funciones de onda no son importantes, los resultados obtenidos mediante en Modelo de Capas y la QRPA coinciden. Aclarar esta discrepancia es de la máxima importancia, ya que una señal positiva de una desintegración $0\nu\beta\beta$ requeriría, para obtener información acerca de la masa de los neutrinos y de su jerarquía, de un elemento de matriz nuclear que se conociese con la mayor precisión posible.

En esta misma línea, los esfuerzos del Modelo de Capas deberían dedicarse a la obtención de elementos de matriz nucleares en espacios de valencia mayores, cercanos a aquéllos que se utilizan en los cálculos QRPA. Así, se estimaría el efecto de las truncaciones en el espacio de valencia exigidas por los cálculos actuales. En esta dirección ya se han dado algunos pasos, pero mucho trabajo queda todavía por hacer. Además, si se calculasen, dentro del Modelo de Capas, las transiciones de los núcleos ^{96}Zr o ^{100}Mo, el resultado se podría comparar con el de la QRPA. Lo mismo se puede decir referido a este método, con respecto a las desintegraciones de los núcleos ^{48}Ca y ^{124}Sn —por el momento, tan sólo existen resultados preliminares para esta última.

Otro punto que podría ser mejorado en los cálculos de Modelo de Capas para obtener una comparación más directa con los resultados QRPA sería ir más allá de la aproximación de cierre. En este caso se podría obtener la descomposición multipolar de la transición, en función del J^π del estado virtual intermedio, y compararlo con el resultado obtenido por la QRPA.

Por otra parte, el reciente interés que suscita la desintegración del núcleo ^{150}Nd, bien deformado, en ^{150}Sm, con una deformación mucho menor, ha puesto de manifiesto la importancia de conseguir una buena descripción del papel que juega la deformación en la desintegración $0\nu\beta\beta$. En este trabajo hemos visto que dichas desintegraciones están desfavorecidas en el caso de producirse entre núcleos con diferente deformación; es más, hemos visto que incluso en el caso de transiciones entre dos núcleos igualmente deformados el elemento de matriz nuclear será menor que en el caso de una transición entre dos núcleos esféricos. En cualquier caso,

aún queda trabajo que realizar sobre este aspecto de la desintegración hasta llegar a tener una comprensión definitiva sobre la relevancia de la deformación en este proceso.

Además, un tratamiento adecuado de las correlaciones de corto alcance seria necesario para reducir la incertidumbre inherente a la situación actual en que dichas correlaciones se incluyen mediando dos métodos alternativos, el de Jastrow y el UCOM. Como ya se mencionó en el texto, esta tarea es complicada, ya que requiere que la renormalización del operador de transición sea de la misma naturaleza que aquélla que sufre la interacción. En todo caso, actualmente hay grupos trabajando en este problema.

Por último, la especialización en determinazas zonas o transiciones para obtener resultados más precisos de los elementos de matriz nucleares podría ser también una opción interesante, al menos en algunos casos. Por ejemplo, para $A = 136$, la desintegración $2\nu\beta\beta$ tiene una vida media excepcionarmente grande, y aún no ha sido determinada experimentalmente. Es un reto explicar este valor tan pequeño de la probabilidad de transición. Dado que sabemos que la deformación dificulta la desintegración $\beta\beta$, podría haber una conexión entre esto y el caso de $A = 136$.

Unos estudios más completos implicarían un cálculo sistemático de un amplio rango de propiedades espectroscópicas de los núcleos relevantes para cada transición —como la que ya hemos comenzado a hacer en el caso de $A = 76$. Así, se estudiarían las ocupaciones, las funciones de estructura de Gamow-Teller y dipolar, las desintegraciones beta simples o las $2\nu\beta\beta$, cuando sean conocidas experimentalmente. Todos estos datos deberían darnos una idea bastante precisa sobre si una interacción es adecuada o no para estudiar una desintegración en concreto.

En resumen, tanto la coexistencia de estados esféricos, deformados y superdeformados en el ^{40}Ca como los elementos de matriz nucleares de las desintegraciones $0\nu\beta\beta$ han sido estudiadas con magnífico resultado dentro del Modelo de Capas. Sin embargo, algunas cuestiones y mejoras quedan pendientes. En cuanto al ^{40}Ca, se podrían explorar algunas propiedades más, tales como las distribuciones dipolar y de Gamow-Teller o las transiciones $E0$ entre los estados 0^+. Con respecto a las desintegraciones $0\nu\beta\beta$, la prioridad reside en reconciliar los valores obtenidos por el Modelo de Capas y la QRPA para los elementos de matriz nucleares. Para ello, sería importante realizar cálculos en espacios de valencia mayores y obtener la

descomposición multipolar de la transición. Por otra parte, el papel de la deformación en el elemento de matriz nuclear debería ser clarificado aún más. Finalmente, un estudio adecuado de las correlaciones de corto alcance o el desarrollo de interacciones adaptadas a regiones o transiciones concretas contribuiría a reducir la incertidumbre asociada a los valores del elemento de matriz nuclear.

Appendix A

Algebraic models and nuclear deformation

In the ISM context algebraic models constitute the origin of a collective behaviour of nuclei such as deformation. Besides, they permit to predict the deformation associated with different configurations of the nuclei at hand. The common origin of these models is the SU(3) symmetry of the harmonic oscillator as first pointed out by Elliott [99, 100]. Then, variations around this idea try to adapt it to other more general situations.

A.1 The Elliott SU(3) model

The SU(3) symmetry appears as a symmetry of the isotropic three dimensional harmonic oscillator Hamiltonian:

$$H_0 = \frac{1}{2}\hbar\omega\left(\mathbf{p}^2+\mathbf{r}^2\right) \tag{A.1}$$

$$= \frac{1}{2}\hbar\omega\left(a^\dagger a+\frac{3}{2}\right), \tag{A.2}$$

with the creation and annihilation operators defined as:

$$a^\dagger = \frac{1}{\sqrt{2}}(\mathbf{p} - i\mathbf{r}),$$
$$a = \frac{1}{\sqrt{2}}(\mathbf{p} + i\mathbf{r}). \tag{A.3}$$

Therefore, the Hamiltonian of Eq. (A.1) is invariant under such transformations that preserve the product $a^\dagger a$. In general, these transformations form the group $\mathrm{U}\left(\frac{(p+1)(p+2)}{2}\right)$ for a certain major shell p, which gives the spatial symmetry of the Hamiltonian. Along with the spin-isospin symmetry, manifested by the group U(4), they constitute the symmetries of the nuclear problem.

Since the atomic nucleus is a fermionic system, the full wave function must be antisymmetric. In terms of the representations of the groups mentioned above, this means that every state must belong to the $[1^m]$ irreductible representation (irrep) of $\mathrm{U}\left(4\frac{(p+1)(p+2)}{2}\right)$, where m is the number of particles of the problem considered. This is obtained when to a spatial component belonging to the $[f]$ irrep, corresponds a $[f^c]$ state in spin-isospin counterpart.

In the present case it is enough to consider the subgroup U(3) of $\mathrm{U}\left(\frac{(p+1)(p+2)}{2}\right)$, which can be seen as the unitary transformations of the complex vector $a^\dagger$. The particularity of this group is that its generators happen to be:

$$H_0 = \frac{1}{2}(\mathbf{p}\cdot\mathbf{p} + \mathbf{r}\cdot\mathbf{r}),$$
$$\mathbf{L}_\mu = -i(\mathbf{r}\times\mathbf{p})_\mu,$$
$$\mathbf{Q}_\mu = \frac{\sqrt{6}}{2}\left((\mathbf{r}\times\mathbf{r})^{(2)}_\mu + (\mathbf{p}\times\mathbf{p})^{(2)}_\mu\right), \tag{A.4}$$

where **L** and **Q** are the angular momentum and the algebraic quadrupole operator, respectively. The latter is defined in function of the spherical harmonics as:

$$\mathbf{Q}_\mu = \sqrt{\frac{4\pi}{5}}\left(r^2\mathbf{Y}^{(2)}_\mu(r) + p^2\mathbf{Y}^{(2)}_\mu(p)\right). \tag{A.5}$$

As H_0 conmutes with the rest of the generators, these eight form a subgroup of U(3). This is indeed the physically interesting group since the transformations generated by H_0 represent mere changes of phase. This resulting group is SU(3).

To label the irreps of the group SU(3) we need a Casimir operator that conmutes with all the group generators. In the present case, it has the form:

$$C_{SU(3)} = \frac{1}{4}\left(\mathbf{Q}\cdot\mathbf{Q} + 3\mathbf{L}\cdot\mathbf{L}\right), \tag{A.6}$$

and the expected values of the different irreps of SU(3) are, in terms of the two labels λ and μ that identify each irrep:

$$\left\langle C_{SU(3)}\right\rangle = \lambda^2 + \mu^2 + \lambda\mu + 3\left(\lambda+\mu\right). \tag{A.7}$$

States within a given irrep are only connected to states in the same irrep.

From Eq. (A.6) it is clear that a quadrupole-quadrupole interaction[1] can be decomposed in a term which is invariant under the SU(3) group and an $L\cdot L$ component. This latter term breaks the SU(3) symmetry of the Hamiltonian but, as it is formed only by generators of the group, it still does not mix states belonging to different representations. It does only break the energy degeneracy between the members of the same irrep —and different angular momentum. Now, the energy of the states reads:

$$E_{(\lambda\mu)L} = \hbar\omega\left[m\left(p+\frac{3}{2}\right)\right] - 2a\left(\lambda^2+\mu^2+\lambda\mu+3\left(\lambda+\mu\right)\right) + \frac{3}{2}aL\left(L+1\right) \tag{A.8}$$

where a is the strength of an attractive quadrupole-quadrupole interaction.

From Eq. (A.8) it can be seen that we have, for each irrep of SU(3), an structure whose levels have the energy dependence $\sim L\left(L+1\right)$. If we add the spin to this picture this would transform into a $\sim J\left(J+1\right)$ dependence. In addition to this, these states have strong transitions between them but are not connected with other states belonging to different irreps. In short, these structures can be seen as

[1] The quadrupole operator of SU(3) is the algebraic operator in contrast to the collective operator which is function only of the spatial coordinates. However, since in the same oscillator shell the matrix elements of the operators $(r\times r)^{(2)}_{\mu}$ and $(p\times p)^{(2)}_{\mu}$ coincide, both interactions can be safely interchanged.

rotational bands.

In summary, the SU(3) symmetry of the harmonic oscillator Hamiltonian combined with a quadrupole-quadrupole interaction brings out a rotational spectra or, equivalently, is able to give the microscopic foundations of nuclear deformation in the ISM.

A.2 The pseudo-SU(3) model

We have seen in the previous section that the SU(3) symmetry is strongly related to the isotropic three dimensional Mean Field potential. However, we know that in nuclei the actual potential soon deviates from this form as the spin-orbit interaction gains importance. The pseudo-SU(3) [101, 102] recovers the SU(3) symmetry in the case of a large spin-orbit interaction.

After the one body potential (2.1), it follows that in the case the spin-orbit and the dipole-dipole coefficients are related by $C = 4D$, the relation,

$$E_{pl\,j=l+1/2} = E_{p(l+2)\,j=(l+2)-1/2}, \tag{A.9}$$

is fulfilled. In other words, two states with $\Delta l = 2$ appear degenerated in energy and with $\Delta j = 1$, this is, they look like spin-orbit partners in a situation without spin-orbit interaction. This actually happens in nuclei —e.g. for the $(0d_{3/2}\text{-}1s_{1/2})$, $(0f_{5/2}\text{-}1p_{3/2})$, $(0g_{7/2}\text{-}1d_{5/2})$, $(0h_{9/2}\text{-}1f_{7/2})$ orbits— meaning that the above condition is, at least, approximately valid —in fact Relativistic Mean Field calculations predict $C \approx (3-5)D$ [185].

Taking advantage of this situation a pseudo angular momentum $\widetilde{l}$ can be defined so that the above degenerated orbits have the new labels:

$$\begin{matrix} l_{j=l+1/2} \\ l+2_{j=l+2-1/2} \end{matrix} \rightarrow \begin{matrix} \widetilde{l+1}_{j=\widetilde{l+1}-1/2} \\ \widetilde{l+1}_{j=\widetilde{l+1}+1/2} \end{matrix}, \tag{A.10}$$

which now correspond to pseudo spin-orbit partners. This kind of transformation can be applied to every state of a given major oscillator shell p but the orbit with $j = p + 1/2$. Accordingly, the members of the shell being transformed form a pseudo shell which is now:

$$p \rightarrow \widetilde{p-1}. \tag{A.11}$$

In this pseudo scheme there is no spin-orbit interaction, or at least it is very weak —in the case the two orbits above are not exactly degenerated. Hence, the pseudo SU(3) symmetry holds, acting in the pseudo $\widetilde{p-1}$ shell. Then, as in the original SU(3) case, the quadrupole-quadrupole interaction will generate the rotational motion of the nucleus.

A.3 The quasi-SU(3) model

The quasi scheme [103, 42] takes into account the collectivity of the orbits with $j = p + 1/2$, which are not included into the pseudo model. The basic idea is to notice the resemblance of the quadrupole matrix elements of the orbital —a good quantum number without spin-orbit interaction— and total angular momenta.

Since the radial matrix elements will not change, the operator C_2 is defined as the quadrupole operator with its radial part removed:

$$C_2 = \sqrt{\frac{16\pi}{5}}\mathbf{Y}_2(\theta,\phi). \tag{A.12}$$

The matrix elements of this operator, in the good l and good j schemes read:

$$\begin{aligned}\langle jm|C_2|jm\rangle &= \frac{j(j+1)-3m^2}{2j(2j+2)},\\ \langle lm|C_2|lm\rangle &= \frac{l(l+1)-3m^2}{(2l-1)(2l+3)}.\end{aligned} \tag{A.13}$$

$$\langle jm|C_2|j+2m\rangle = \frac{3}{2}\left(\frac{\left[(j+2)^2-m^2\right]\left[(j+1)^2-m^2\right]}{(2j+2)^2(2j+4)^2}\right)^{\frac{1}{2}},$$

$$\langle lm\,|C_2|\,l+2m\rangle = \frac{3}{2}\left(\frac{\left[(l+2)^2-m^2\right]\left[(l+1)^2-m^2\right]}{(2l+5)\,(2l+3)^3\,(2l+1)}\right)^{\frac{1}{2}}. \qquad \text{(A.14)}$$

$$\langle jm\,|C_2|\,j+1m\rangle = -\frac{3m\left[(j+2)^2-m^2\right]^{\frac{1}{2}}}{2j\,(2j+2)\,(2j+4)}. \qquad \text{(A.15)}$$

Two conclusions can be obtained from the equations above:

1. The matrix elements of the C_2 operator with $\Delta j = 0/\Delta l = 0$ and $\Delta j = 2/\Delta l = 2$ are approximately the same.

2. The matrix element with $\Delta j = 1$ is very small for both large and small values of m, which correspond to the lowest oblate and prolate orbits, respectively. In other words, $\Delta j = 1$ is very small in deformed situations at which the quasi scheme will be applied.

Therefore, the quasi-SU(3) model neglects the $\Delta j = 1$ matrix elements and proposes the identification:

$$\begin{matrix} l \\ m \end{matrix} \rightarrow \begin{matrix} j = l + \frac{1}{2} \\ m + sign\,(m)\,\frac{1}{2} \end{matrix}, \qquad \text{(A.16)}$$

which is one to one except for $m = 0$. Hence, the collectivity will be given by the pair of orbits with $\Delta j = 2$.

This condition is independent on the angular momentum of the orbit. Hence, orbits with $j = p + 1/2$ originally belonging to the p harmonic oscillator shell can, after being lowered by the spin-orbit interaction, be associated with other orbits belonging to the $p-1$ shell, as long as they have $\Delta j = 2$.

The value of the quadrupole moment in this scheme differ slightly from these of the pure SU(3). For the latter, acting on a single harmonic oscillator shell the —dimensionless[2] — eigenvalues are:

[2] The corresponding units are given by the electron charge e and the harmonic oscillator parameter b^2.

Figure A.1: Level scheme for the quadrupole operator Q_0 in the SU(3) —also valid for pseudo-SU(3)— and quasi-SU(3) models. The lowest states —highest values of Q_0— correspond, in dimensionless units, to $Q_0 = 2p$ in the SU(3) case and $Q_0 = 2p - \frac{1}{2}$ for quasi-SU(3).

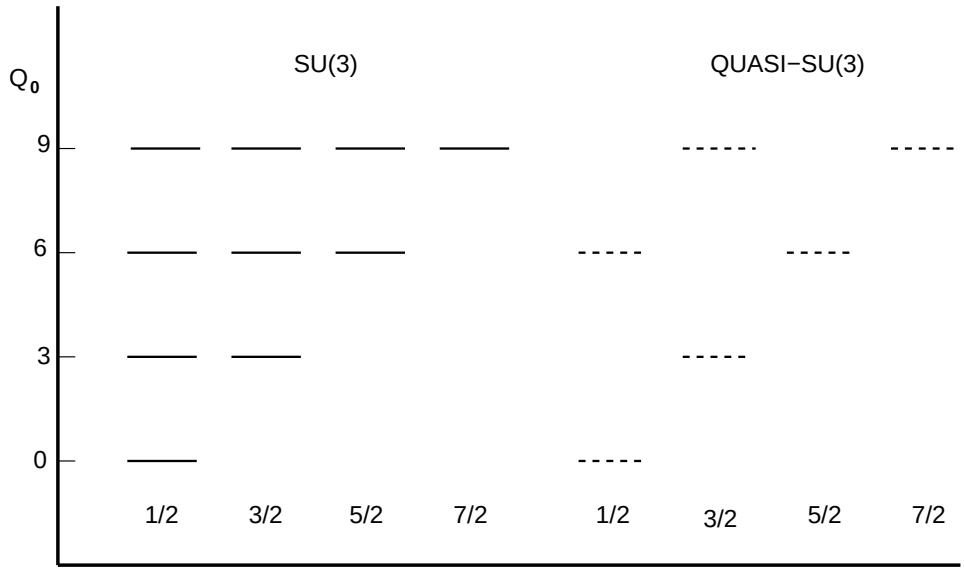

$$\langle Q_0 \rangle = \left\langle 2z^2 - x^2 - y^2 \right\rangle = 2p, 2p-3, 2p-6, \ldots \tag{A.17}$$

In the quasi scheme the energies will be shifted $1/2$ according to Eq. (A.16). Additionally, the neglection of $\Delta j = 1$ transitions reduces the number of orbits and hence the multiplicity of the eigenvalues. A level scheme of the single particle quadrupole moments can be seen in Figure A.1.

Appendix B

The Center of Mass

The atomic nuclear problem is an A body problem, consequently involving wave functions with $3A$ degrees of freedom —only spatial coordinates are taken into account for simplicity. However, not all them are physically relevant, since only the intrinsic motion of the nuclei is significant. This motion amounts to $3A-3$ degrees of freedom. The remaining 3 correspong to the Center of Mass (CM), and need to be separated from the rest in order to get proper results.

In principle, the nuclear problem should be solved in such a way that the translational invariance of the whole nucleus was preserved, so that its CM wave function would be directly factorised as:

$$|\Psi(r)\rangle = |\phi(R)\rangle \left|\psi\left(r'\right)\right\rangle, \tag{B.1}$$

where R is the centre of mass coordinate and r_i' the relative ones. They read:

$$R = \frac{1}{A}\sum_{i=1}^{A} r_i, \tag{B.2}$$

$$r_i' = r_i - R. \tag{B.3}$$

In general, the SM does not fulfill this condition. Instead, nucleons move rather independently within a potential fixed in space with the CM bound in some way

to this potential as well. In the atomic SM this is not a problem since the nucleus can be considered fixed indeed. The problem arises in the nuclear SM. Now, the CM does not experience the free particle behaviour that it would have in a translationally invariant potential. Even though a many-body factorization like that of Eq. (B.1) can be demanded by construction, it is not practical because it results into very hard antisymmetrization problems.

The special case of the use of Harmonic Oscillator wave functions —which is the choice made in Chapter 2— allows for another solution to this problem. In this particular case, the one body potential can be written as:

$$\begin{aligned} H_{HO}^{1b} &= \frac{1}{2m}\sum_{i=1}^{A} p_i^2 + \frac{1}{2}m\omega^2 \sum_{i=1}^{A} r_i^2 \\ &= \frac{1}{2m}\sum_{i=1}^{A} p_i'^2 + \frac{1}{2}m\omega^2 \sum_{i=1}^{A} r_i'^2 + \frac{1}{2mA}P^2 + \frac{1}{2}mA\omega^2 R^2 \\ &= H_{rel} + H_{cm}, \end{aligned} \tag{B.4}$$

where P is the CM momentum and p_i' the relative ones, defined as:

$$P = \sum_{i=1}^{A} p_i, \tag{B.5}$$

$$p_i' = p_i - \frac{1}{A}P. \tag{B.6}$$

In addition to the separation of Eq. (B.4), we have that $[H_{rel}, H_{cm}] = 0$, so that the two parts decouple. As long as additional two body residual interactions depend only on the relative positions and momenta, this condition remains to be satisfied. This means that a factorization like that of eq. (B.1) can be obtained for this choice of the basis states.

Thus, the energy of the full system can be separated into the excitations of the CM and that of the intrinsic system:

$$H\left|\Psi\left(r\right)\right\rangle = \left(\left(N_{rel}+\frac{3}{2}\left(A-1\right)\right)\hbar\omega+\left(N_{cm}+\frac{3}{2}\right)\hbar\omega\right)\left|\Psi\left(r\right)\right\rangle. \tag{B.7}$$

As was mentioned above, the only physically relevant excitations are that of the intrinsic system. Those excited states that are associated to excitations of the CM —i.e. with $N_{cm} > 0$— are called spurious states [99], since they give no information about the nucleus itself. Therefore, a strategy must be developed in order to eliminate these spurious states from the solutions. The prodedure consists in performing calculations not with the usual two body Hamiltonian but with an additional CM term:

$$\widetilde{H} = H + \beta H_{cm}, \tag{B.8}$$

that will lift the spourious states when the value of the β coefficient is large. Only the states with no CM excitation would remain at low energies.

Unfortunately, this recipe can not always be used. Looking more carefully at the form of H_{cm}, Eq.(B.4), it can be maybe more clearly rewritten as:

$$\begin{aligned} H_{cm} &= H_{HO}^{1b} + H_{rel} \\ &= H_{HO}^{1b} - \frac{1}{A}\left(\frac{1}{2m}\sum_{i<j}^{A}\left(p_i-p_j\right)^2 + \frac{1}{2}m\omega^2\sum_{i<j}^{A}\left(r_i-r_j\right)^2\right), \end{aligned} \tag{B.9}$$

in other words, a one body oscillator plus a two body oscillator force. The latter, by virtue of the Talmi-Moshinsky transformation gives non vanishing matrix elements only when $n\hbar\omega$ is the same in the initial and final states. This is, to be able to describe completely H_{cm}, all states up to a given $n\hbar\omega$ are required to lie within the valence space. If this valence space does not encompass all these states, then neither the Hamiltonian remains H_{cm}, nor the above prescription to eliminate spurious states keeps to be valid.

This is precisely the situation faced in chapter 3 when studying ^{40}Ca, with the r_2pf valence space allowing excited states up to $12\hbar\omega$ but even without all $1\hbar\omega$

excitations included. In these cases, the elimination of spurious states can not be done safely. A compromise solution [186] is to mantain the form of the modified hamiltonian (B.8) but choosing a rather small value of the β coefficient —of the order of 1—. This remedy is based on the assumption that, even though in the valence space H_{cm} is not the actual CM Hamiltonian, at least it must be closely connected to the true one. A too large value for β would tend to eliminate parts of the valence space from the calculation —thus artificially truncating the valence space— while a too small β parameter would not lift enough the spurious terms that are required to be eliminated.

This is the approach followed through our theoretical calculations, as referred at section 3.3.

Appendix C

Analytical form of the neutrino potentials

In Chapter 4, the components of the $0\nu\beta\beta$ transition operator in momentum space were introduced in Eq. (4.21). Their explicit form is:

$$
\begin{aligned}
h_{VV}^{F}(q) &= -\frac{g_V^2(0)}{\left(1+\frac{q^2}{\Lambda_V^2}\right)^4}, \\
h_{AA}^{GT}(q) &= \frac{g_A^2(0)}{\left(1+\frac{q^2}{\Lambda_A^2}\right)^4}, \\
h_{AP}^{GT}(q) &= -\frac{2}{3}\frac{g_A^2(0)\,q^2}{\left(1+\frac{q^2}{\Lambda_A^2}\right)^4 (q^2+m_\pi^2)}\left(1-\frac{m_\pi^2}{\Lambda_A^2}\right), \\
h_{PP}^{GT}(q) &= \frac{1}{3}\frac{g_A^2(0)\,q^4}{\left(1+\frac{q^2}{\Lambda_A^2}\right)^4 (q^2+m_\pi^2)^2}\left(1-\frac{m_\pi^2}{\Lambda_A^2}\right)^2, \\
h_{MM}^{GT}(q) &= \frac{2}{3}\frac{(\mu_p-\mu_n)^2 g_V^2(0)\,q^2}{4M_p^2\left(1+\frac{q^2}{\Lambda_V^2}\right)^4}, \\
h_{AP}^{T}(q) &= \frac{2}{3}\frac{g_A^2(0)\,q^2}{\left(1+\frac{q^2}{\Lambda_A^2}\right)^4 (q^2+m_\pi^2)}\left(1-\frac{m_\pi^2}{\Lambda_A^2}\right),
\end{aligned}
$$

$$
\begin{aligned}
h^T_{PP}(q) &= -\frac{1}{3}\frac{g_A^2(0)\,q^4}{\left(1+\frac{q^2}{\Lambda_A^2}\right)^4\left(q^2+m_\pi^2\right)^2}\left(1-\frac{m_\pi^2}{\Lambda_A^2}\right)^2, \\
h^T_{MM}(q) &= \frac{1}{3}\frac{(\mu_p-\mu_n)^2\,g_V^2(0)\,q^2}{4M_p^2\left(1+\frac{q^2}{\Lambda_V^2}\right)^4}.
\end{aligned}
\tag{C.1}
$$

From these expressions, the neutrino potentials have been calculated analytically through the equations:

$$
\begin{aligned}
V_x^{F/GT}(r) &= \frac{2}{\pi}\frac{R}{g_A^2(0)}\int_0^\infty j_0(qr)\,\frac{h_x^{F/GT}(q)}{(q+\mu)}q\,dq, \\
V_x^{T}(r) &= \frac{2}{\pi}\frac{R}{g_A^2(0)}\int_0^\infty -j_2(qr)\,\frac{h_x^{T}(q)}{(q+\mu)}q\,dq,
\end{aligned}
\tag{4.22}
$$

Since in the solution numerous terms appear, we will only keep the most relevant ones due to physical considerations depending on the value of the energies μ, m_π and Λ —taken generically as Λ_v and Λ_a. In our approximation terms will be considered up to:

$$
1, \frac{m_\pi}{\Lambda}, \frac{\mu}{m_\pi}, \left(\frac{m_\pi}{\Lambda}\right)^2, o\left(\frac{\mu}{\Lambda}\right), o\left(\frac{\mu}{m_\pi}\right)^2, o\left(\frac{m_\pi}{\Lambda}\right)^3 \ldots \tag{C.2}
$$

This is, neglected contributions can be estimated to be $\sim 1\%$ or less.

According to this, the analytical form of the neutrino potentials reads:

$$
\begin{aligned}
&V_{vv}^F(r) = -\frac{g_V^2(0)}{g_A^2(0)}\frac{R}{r}\times \\
&\quad\left\{\frac{2}{\pi}\left(\sin(\mu r)\,Ci(\mu r)-\cos(\mu r)\,Si(\mu r)\right)-\right. \\
&-e^{-\Lambda_v r}\left(1+\frac{11}{16}(\Lambda_v r)+\frac{3}{16}(\Lambda_v r)^2+\frac{1}{48}(\Lambda_v r)^3\right)+ \\
&\left.+\;o(\ldots)\right\}
\end{aligned}
\tag{C.3}
$$

$$
\begin{aligned}
V_{aa}^{GT}(r) = & \frac{R}{r}\times \\
& \left\{\frac{2}{\pi}\left(\sin(\mu r)\,Ci(\mu r)-\cos(\mu r)\,Si(\mu r)\right)-\right. \\
& -e^{-\Lambda_a r}\left(1+\frac{11}{16}(\Lambda_a r)+\frac{3}{16}(\Lambda_a r)^2+\frac{1}{48}(\Lambda_a r)^3\right)+ \\
& \left.+\,o(...)\right\}
\end{aligned}
\tag{C.4}
$$

$$
\begin{aligned}
V_{ap}^{GT}(r) = & -\frac{2}{3}\frac{R}{r}\times \\
& \left\{e^{-m_\pi r}\left(1+4\frac{m_\pi^2}{\Lambda_a^2}\right)-\right. \\
& -e^{-\Lambda_a r}\left(\left(1+\frac{11}{16}(\Lambda_a r)+\frac{3}{16}(\Lambda_a r)^2+\frac{1}{48}(\Lambda_a r)^3\right)+\right. \\
& \quad\left.+\left(\frac{m_\pi^2}{\Lambda_a^2}\right)\left(4+\frac{29}{16}(\Lambda_a r)+\frac{5}{16}(\Lambda_a r)^2+\frac{1}{48}(\Lambda_a r)^3\right)\right)+ \\
& +\left(\frac{\mu}{m_\pi}\right)\frac{2}{\pi}\left(\sinh(m_\pi r)\,Chi(m_\pi r)-\cosh(m_\pi r)\,Shi(m_\pi r)\right)+ \\
& \left.+\,o(...)\right\}\left(1-\frac{m_\pi^2}{\Lambda_a^2}\right)
\end{aligned}
\tag{C.5}
$$

$$
\begin{aligned}
V_{ap}^{T}(r) \;=\; & \frac{2}{3}\frac{R}{r}\frac{1}{(m_\pi^2 r^2)}\times \\
& \left\{\;\frac{2}{\pi}\left(\cos(\mu r)\,Si(\mu r)-\sin(\mu r)\,Ci(\mu r)\right)\times\right. \\
& \qquad\left.\times\left(3-\left(3+(m_\pi r)^2\right)\left(10\frac{m_\pi^4}{\Lambda_a^4}+\frac{\mu^2}{m_\pi^2}+4\frac{\mu^2}{\Lambda_a^2}\right)\right)+\right. \\
& +\frac{6}{\pi}(\mu r)\left(\cos(\mu r)\,Ci(\mu r)+\sin(\mu r)\,Si(\mu r)\right)\left(1-\frac{\mu^2}{m_\pi^2}\right)+ \\
& \left.+\,e^{-m_\pi r}\left(3+3(m_\pi r)+(m_\pi r)^2\right)\left(1+4\frac{m_\pi^2}{\Lambda_a^2}-\frac{\mu^2}{m_\pi^2}\right)-\right.
\end{aligned}
$$

$$
\begin{aligned}
&- e^{-\Lambda_a r}\left(\frac{m_\pi^2}{\Lambda_a^2}\right)\left(\left(12+12\left(\Lambda_a r\right)+\frac{11}{2}\left(\Lambda_a r\right)^2+\frac{3}{2}\left(\Lambda_a r\right)^3+\frac{1}{4}\left(\Lambda_a r\right)^4+\frac{1}{48}\left(\Lambda_a r\right)^5\right)+\right.\\
&\qquad\left.+\left(\frac{m_\pi^2}{\Lambda_a^2}\right)\left(30+30\left(\Lambda_a r\right)+13\left(\Lambda_a r\right)^2+3\left(\Lambda_a r\right)^3+\frac{3}{8}\left(\Lambda_a r\right)^4+\frac{1}{48}\left(\Lambda_a r\right)^5\right)\right)\\
&+\left(\frac{\mu}{m_\pi}\right)\frac{2}{\pi}\left(\sinh\left(m_\pi r\right)Chi\left(m_\pi r\right)-\cosh\left(m_\pi r\right)Shi\left(m_\pi r\right)-\right.\\
&\qquad\left.-3\left(m_\pi r\right)\left(\cosh\left(m_\pi r\right)Chi\left(m_\pi r\right)-\sinh\left(m_\pi r\right)Shi\left(m_\pi r\right)\right)\right)\left(1+4\frac{m_\pi^2}{\Lambda_a^2}\right)+\\
&+\left(\frac{m_\pi^2}{\Lambda_a^2}\right)\left(\frac{\mu}{\Lambda_a}\right)\frac{1}{\pi}\left(-9\left(\Lambda_a r\right)+\right.\\
&\qquad+\left(33+\left(\Lambda_a r\right)^2\right)\left(\cosh\left(\Lambda_a r\right)Chi\left(\Lambda_a r\right)-\sinh\left(\Lambda_a r\right)Shi\left(\Lambda_a r\right)\right)-\\
&\qquad\left.-\left(33+12\left(\Lambda_a r\right)^2\right)\left(\sinh\left(\Lambda_a r\right)Chi\left(\Lambda_a r\right)-\cosh\left(\Lambda_a r\right)Shi\left(\Lambda_a r\right)\right)\right)+\\
&+\left.o\left(...\right)\right\}\left(1-\frac{m_\pi^2}{\Lambda_a^2}\right)
\end{aligned}
\tag{C.6}
$$

$$
\begin{aligned}
V_{pp}^{GT}\left(r\right) &= \frac{1}{3}\frac{R}{r}\times\\
&\left\{\ e^{-m_\pi r}\left(\left(1-\frac{1}{2}\left(m_\pi r\right)\right)+\left(\frac{m_\pi^2}{\Lambda_a^2}\right)\left(8-2\left(m_\pi r\right)\right)\right)-\right.\\
&- e^{-\Lambda_A r}\left(\left(1+\frac{11}{16}\Lambda_a r+\frac{3}{16}\left(\Lambda_a r\right)^2+\frac{1}{48}\left(\Lambda_a r\right)^3\right)+\right.\\
&\qquad\left.+\left(\frac{m_\pi^2}{\Lambda_a^2}\right)\left(8+\frac{29}{8}\left(\Lambda_a r\right)+\frac{5}{8}\left(\Lambda_a r\right)^2+\frac{1}{24}\left(\Lambda_a r\right)^3\right)\right)+\\
&+\left(\frac{\mu}{m_\pi}\right)\frac{1}{\pi}\left(\sinh\left(m_\pi r\right)Chi\left(m_\pi r\right)-\cosh\left(m_\pi r\right)Shi\left(m_\pi r\right)+\right.\\
&\qquad\left.+\left(m_\pi r\right)\left(\cosh\left(m_\pi r\right)Chi\left(m_\pi r\right)-\sinh\left(m_\pi r\right)Shi\left(m_\pi r\right)\right)\right)+\\
&+\left.o\left(...\right)\right\}\left(1-\frac{m_\pi^2}{\Lambda_a^2}\right)^2
\end{aligned}
\tag{C.7}
$$

$$
\begin{aligned}
V_{pp}^{T}(r) &= -\frac{1}{3}\frac{R}{r}\frac{1}{m_\pi^2 r^2}\times \\
&\left\{ e^{-m_\pi r}\left(\frac{m_\pi^2}{\Lambda_a^2}\right)\left(\left(12+12(m_\pi r)+2(m_\pi r)^2-2(m_\pi r)^3\right)+(\Lambda_a r)^2\left(-\frac{1}{2}-\frac{1}{2}(m_\pi r)\right)+\right.\right. \\
&\qquad \left.+\frac{5}{2}\left(\frac{m_\pi^2}{\Lambda_a^2}\right)\left(24+27(m_\pi r)+11(m_\pi r)^2\right)\right)- \\
&- e^{-\Lambda_a r}\left(\frac{m_\pi^2}{\Lambda_a^2}\right)\left(\left(12+12(\Lambda_a r)+\frac{11}{2}(\Lambda_a r)^2+\frac{3}{2}(\Lambda_a r)^3+\frac{1}{4}(\Lambda_a r)^4+\frac{1}{48}(\Lambda_a r)^5\right)+\right. \\
&\qquad \left.+\left(\frac{m_\pi^2}{\Lambda_a^2}\right)\left(60+60(\Lambda_a r)+26(\Lambda_a r)^2+6(\Lambda_a r)^3+\frac{3}{4}(\Lambda_a r)^4+\frac{1}{24}(\Lambda_a r)^5\right)\right)- \\
&- \frac{2}{\pi}\left(\frac{m_\pi^6}{\Lambda_a^6}\right)\left(120+10(\Lambda_a r)^2\right)(\cos(\mu r)\,Si(\mu r)-\sin(\mu r)\,Ci(\mu r))- \\
&- \frac{1}{\pi}\left(\frac{\mu}{m}\right)(3(m_\pi r)+ \\
&\qquad +\left(3+2(m_\pi r)^2-12\left(\frac{m_\pi^2}{\Lambda_a^2}\right)\right)(\sinh(m_\pi r)\,Chi(m_\pi r)-\cosh(m_\pi r)\,Shi(m_\pi r))- \\
&\qquad -\left(3(m_\pi r)+(m_\pi r)^3\right)(\cosh(m_\pi r)\,Chi(m_\pi r)-\sinh(m_\pi r)\,Shi(m_\pi r))- \\
&- \frac{3}{\pi}(\mu r)(3+3(\Lambda_a r)(\sinh(\Lambda_a r)\,Chi(\Lambda_a r)-\cosh(\Lambda_a r)\,Shi(\Lambda_a r))- \\
&\qquad -8(\cosh(\Lambda_a r)\,Chi(\Lambda_a r)-\sinh(\Lambda_a r)\,Shi(\Lambda_a r)))+ \\
&+ o(\ldots)\}\left(1-\frac{m_\pi^2}{\Lambda_a^2}\right)^2
\end{aligned}
\tag{C.8}
$$

$$
\begin{aligned}
V_{mm}^{GT}(r) &= \frac{2}{3}(\mu_p-\mu_n)^2\frac{g_V^2(0)}{g_A^2(0)}\frac{R}{r}\frac{1}{4}\left(\frac{\Lambda_v^2}{M_p^2}\right)\times \\
&\left\{e^{-\Lambda_v r}(\Lambda_v r)\left(\frac{3}{48}+\frac{3}{48}(\Lambda_v r)+\frac{1}{48}(\Lambda_v r)^2\right)+o(\ldots)\right\}
\end{aligned}
\tag{C.9}
$$

$$
\begin{aligned}
V_{mm}^{T}(r) &= \frac{1}{3}(\mu_p-\mu_n)^2\frac{g_V^2(0)}{g_A^2(0)}\frac{R}{r}\frac{1}{4\left(M_p^2r^2\right)}\times \\
&\left\{\ \frac{6}{\pi}\left(\left(\cos(\mu r)\,Si(\mu r)-\sin(\mu r)\,Ci(\mu r)\right)\right)+\right. \\
&+\frac{6}{\pi}\left((\mu r)\left(\cos(\mu r)\,Ci(\mu r)+\sin(\mu r)\,Si(\mu r)\right)\right)+ \\
&+e^{-\Lambda_v r}\left(3+3(\Lambda_v r)+\frac{3}{2}(\Lambda_v r)^2+\frac{1}{2}(\Lambda_v r)^3+\frac{1}{8}(\Lambda_v r)^4+\frac{1}{48}(\Lambda_v r)^5\right)+ \\
&+\frac{3}{\pi}(\mu r)\left(1-3\left(\cosh(\Lambda_v r)\,Chi(\Lambda_v r)-\sinh(\Lambda_v r)\,Shi(\Lambda_v r)\right)\right)+ \\
&\quad+\left(\frac{\mu}{\Lambda_v}\right)\frac{3}{\pi}\left(3+(\Lambda_v r)^2\right)\left(\sinh(\Lambda_v r)\,Chi(\Lambda_v r)-\cosh(\Lambda_v r)\,Shi(\Lambda_v r)\right) \\
&+\left.\ o(...)\right\}
\end{aligned}
\tag{C.10}
$$

List of Figures

2.1 Energy levels of the harmonic oscillator and shell structure modification by a large spin-orbit term. 17

3.1 Superdeformed band in ^{40}Ca. E_γ's, experimental data *vs* fixed $8\hbar\omega$ theoretical calculation. 35
3.2 Superdeformed band in ^{40}Ca. Transition quadrupole moments $Q_0(t)$. Experimental data *vs* fixed $8\hbar\omega$ theoretical calculation. 37
3.3 Normal deformed $K = 0$ band in ^{40}Ca. E_γ's, experimental data *vs* fixed $4\hbar\omega$ theoretical results. 38
3.4 Energies of the lowest states in the different np-nh configurations of ^{40}Ca. Lowest Slater Determinant, lowest 0^+ state in the r_2pf space at fixed $n\hbar\omega$ and full r_2pf calculation. 41
3.5 Energies of the yrast states of ^{40}Ca, in the different fixed np-nh configurations, for even J up to $J = 16$. 42
3.6 E_γ's in the superdeformed band in ^{40}Ca. Experimental data *vs* full r_2pf theoretical calculation. 45
3.7 Transition quadrupole moments in the superdeformed band of ^{40}Ca. Full r_2pf theoretical results compared to experimental data. . . . 48
3.8 Normal deformed $K = 0$ band in ^{40}Ca. E_γ's, experimental data *vs* full r_2pf theoretical calculation. 50
3.9 Transition quadrupole moments in the $K = 0$ normal deformed band in ^{40}Ca. Full r_2pf theoretical results compared to experimental data. 53
3.10 Theoretical *vs* experimental level schemes of ^{40}Ca. 60

4.1 Energies of the ground states of the $A = 76$ isotones. The single beta decay between ^{76}Ge and ^{76}Se is energetically forbidden, leaving ββ as the only available decay channel 62

4.2 Feynman diagrams for the 0νββ and 2νββ decays 63

4.3 $M'^{0\nu\beta\beta}$'s for ISM and QRPA calculations treating the short range correlations with the Jastrow approach 79

4.4 $M'^{0\nu\beta\beta}$'s for ISM and QRPA calculations treating the short range correlations with the UCOM approach 80

4.5 Evolution of $C(r)$ with r 83

4.6 Evolution of the Fermi and Gamow-Teller parts of $C(r)$ with r . . 84

4.7 Evolution of the Gamow-Teller part of $C(r)$ for the ^{82}Se $\rightarrow$ ^{82}Kr 0νββ transition 85

5.1 Contributions to the Gamow-Teller component of the 0νββ NME as a function of the J^π of the transformed pair for the 0νββ ^{82}Se $\rightarrow$ ^{82}Kr transition 91

5.2 Evolution of the NME of the 0νββ decay with the maximum seniority allowed in the wave functions 94

5.3 $M'^{0\nu\beta\beta}$'s for ISM, ISM with truncated maximum seniority $s_m = 4$, and QRPA calculations. Jastrow type short range correlations . . . 95

5.4 $M'^{0\nu\beta\beta}$'s for ISM, ISM with truncated maximum seniority $s_m = 4$, and QRPA calculations. UCOM type short range correlations . . . 96

5.5 0νββ NME for the equally deformed ^{66}Ge $\rightarrow$ ^{66}Se decay, as a function of the strength of the extra quadrupole-quadrupole interaction 102

5.6 0νββ NME for the ^{66}Ge $\rightarrow$ ^{66}Se decay as a function of the extra quadrupole-quadrupole interaction on ^{66}Se 103

5.7 Contributions to the Gamow-Teller component of the 0νββ NME as a function of the J^π of the transformed pair for the fictitious mirror ^{66}Ge $\rightarrow$ ^{66}Se transition. Evolution with the amount of extra quadrupole-quadrupole interaction added to the Hamiltonian . . . 105

5.8 Contributions to the Gamow-Teller component of the 0νββ NME as a function of the J^{π} of the transformed pair for the fictitious mirror ^{50}Cr → ^{50}Fe transition. Evolution with the amount of extra quadrupole-quadrupole interaction added to the Hamiltonian . . . 106

5.9 Equally deformed ^{66}Ge → ^{66}Se 2νββ NME as a function of the strength of the extra quadrupole-quadrupole interaction 107

5.10 ^{66}Ge → ^{66}Se 2νββ NME as a function of the extra quadrupole-quadrupole interaction on ^{66}Se 108

5.11 Evolution of the 0νββ NME of the ^{66}Ge → ^{66}Se transition with the quadrupole-quadrupole correlations of ^{66}Ge and ^{66}Se 109

5.12 Evolution of the normalized 0νββ NME of the ^{66}Ge → ^{66}Se transition with the quadrupole-quadrupole correlations of ^{66}Ge and ^{66}Se 110

5.13 Evolution of the overlap of the wave functions in the ^{66}Ge → ^{66}Se 0νββ transition with the quadrupole-quadrupole correlations of ^{66}Ge and ^{66}Se 110

5.14 Evolution of the ^{76}Ge → ^{76}Se 0νββ NME with the quadrupole-quadrupole correlations of ^{76}Ge and ^{76}Se 111

5.15 Evolution of the 0νββ NME of the ^{82}Se → ^{82}Kr decay with the quadrupole-quadrupole correlations of ^{82}Se and ^{82}Kr 112

5.16 Evolution of the 0νββ NME of the ^{136}Xe → ^{136}Ba decay with the quadrupole-quadrupole correlations of ^{136}Xe and ^{136}Ba 113

5.17 Quadrupole correlations in ^{82}Kr s a function of the amount of extra quadrupole-quadrupole interaction added to the Hamiltonian, for different values of the maximum seniority permitted in the wave functions, s_m 114

5.18 Gamow-Teller part of the NME for the ^{82}Se → ^{82}Kr decay as a function of the maximun seniority permitted in the wave functions, s_m, calculated for different values of the strength of the extra quadrupole-quadrupole interaction 115

5.19 Comparison between experimental and theoretical occupation numbers for ^{76}Ge and ^{76}Se 118

A.1 Level scheme for the quadrupole operator Q_0 in the SU(3) —also valid for pseudo-SU(3)— and quasi-SU(3) models. 139

List of Tables

3.1 Quadrupole properties the superdeformed band in ^{40}Ca. Fixed $8\hbar\omega$ configuration theoretical calculation 36

3.2 Experimental and theoretical energies of the deformed γ band in ^{40}Ca. Theoretical results from a fixed $4\hbar\omega$ calculation. 39

3.3 Quadrupole properties of the $K = 0$ normal deformed band of ^{40}Ca. Fixed $4\hbar\omega$ theoretical calculation. 39

3.4 Percentage of np-nh components and energy of the first three 0^+ states —ground state, normal deformed and superdeformed bandheads— of ^{40}Ca. Full r_2pf theoretical calculation. 44

3.5 Percentage of np-nh components of the superdeformed band of ^{40}Ca. Full r_2pf theoretical calculation. 46

3.6 Quadrupole properties of the superdeformed band in ^{40}Ca. Full r_2pf theoretical calculation. 47

3.7 Percentage of np-nh components of the $K = 0$ normal deformed band of ^{40}Ca. Full r_2pf theoretical calculation. 49

3.8 Experimental and theoretical energies for the deformed γ band in ^{40}Ca. Full r_2pf theoretical calculation. 51

3.9 Percentage of np-nh components of the deformed γ band of ^{40}Ca. Full r_2pf theoretical calculation. 51

3.10 Quadrupole properties of the $K = 0$ normal deformed band in ^{40}Ca. Full r_2pf theoretical calculation. 52

3.11 Quadrupole properties of the deformed γ band in ^{40}Ca. Full r_2pf theoretical calculation. 54

3.12 Out-band transitions from the superdeformed and normal deformed bands of ^{40}Ca. Full r_2pf theoretical calculation. 55
3.13 Comparison between the theoretical in-band and out-band transition probabilities for the states of the superdeformed band of ^{40}Ca with $J \geq 6$. Full r_2pf theoretical calculation. 56
3.14 Out-band transitions from the deformed γ band of ^{40}Ca. 57

4.1 Available energy, $E_f - E_i = Q_{\beta\beta} + 2m_e$, abundancies and kinematic factor G_{01} for the different $0\nu\beta\beta$ transitions 69
4.2 Evolution of the Fermi component of the $0\nu\beta\beta$ NME for $A = 76$. 73
4.3 Evolution of the Gamow-Teller component of the $0\nu\beta\beta$ NME for $A = 76$ 74
4.4 Evolution of the Tensor component of the $0\nu\beta\beta$ NME for $A = 76$. 74
4.5 Evolution of the full NME for $A = 76$ 75
4.6 [Evolution of the $0\nu\beta\beta$ NME's for the different decays studied.] Evolution of the $0\nu\beta\beta$ NME's for the different decays studied. The reduction due to HOC —both before and after FNS—, FNS and SRC's with respect to the previous result are shown, in percentage. 77
4.7 Comparison between ISM and QRPA of the $0\nu\beta\beta$ NME of the $A = 76$ transition 77
4.8 Contributions of the Jastrow and UCOM type short range correlations to the NME for the different decays studied. 78
4.9 NME's for the $0\nu\beta\beta$ decays to the excited 0_1^+ states, for all the transitions studied. Also, Half-lives are calculated for $\langle m_\nu \rangle = 1$ eV. 85

5.1 Contributions to the Gamow-Teller part of the $0\nu\beta\beta$ NME from decaying pairs coupled to $J = 0$ and $J > 0$, for the different transitions studied 92
5.2 Decomposition of the $0\nu\beta\beta$ NME as a function of the seniority components of the initial and final wave functions, for the $A = 82$ decay. 93
5.3 Decomposition of the wave functions in function of the seniority components for the nuclei studied 97

5.4 Evolution of $-\chi^F$ as a function of the maximum seniority allowed in the wave functions, s_m, for all the studied $0\nu\beta\beta$ decays 98
5.5 Comparison of the values of χ^F between ISM, ISM with truncated maximum seniority $s_m = 4$, and QRPA results 99
5.6 Evolution of χ^T with the maximum seniority permitted in the wave functions, s_m, for all the studied $0\nu\beta\beta$ decays. 100
5.7 Evolution of the $0\nu\beta\beta$ NME with the maximum seniority allowed in the wave function, for the $A = 76$ transition 101
5.8 Proton and neutron occupation numbers of nuclei ^{76}Ge and ^{76}Se. Experiment *vs* theoretical results, obtained for the GCN28.50 and RG.PROLATE interactions 117
5.9 Values of $M'^{0\nu\beta\beta}$ for the $^{76}\text{Ge} \rightarrow {}^{76}\text{Se}$ decay for ISM and QRPA interactions 120

Bibliography

[1] E. RUTHERFORD, The scattering of α and β particles by matter and the structure of the atom, *Phil. Mag.* **21**, 669 (1911).

[2] J. CHADWICK, The existence of a neutron, *Proc. R. Soc. London Ser. A* **136**, 692 (1932).

[3] W. HEISENBERG, Über den Bau der Atomkerne. I, *Z. Phys.* **77**, 1 (1932).

[4] C. R. CHEN, G. L. PAYNE, J. L. FRIAR and B. F. GIBSON, Convergence of Faddeev partial-wave series for triton ground state, *Phys. Rev. C* **31**, 2266 (1985).

[5] J. CARLSON and R. SCHIAVILLA, Structure and dynamics of few-nucleon systems, *Rev. Mod. Phys.* **70**, 743 (1998).

[6] A. KIEVSKY, M. VIVIANI, S. ROSATI, D. HÜBER, W. GLÖCKLE, H. KAMADA, H. WITAŁA and J. GOLAK, Benchmark calculations for polarization observables in three-nucleon scattering, *Phys. Rev. C* **58**, 3085 (1998).

[7] H. KAMADA, A. NOGGA, W. GLÖCKLE, E. HIYAMA, M. KAMIMURA, K. VARGA, Y. SUZUKI, M. VIVIANI, A. KIEVSKY, S. ROSATI, J. CARLSON, S. C. PIEPER, R. B. WIRINGA, P. NAVRÁTIL, B. R. BARRETT, N. BARNEA, W. LEIDEMANN and G. ORLANDINI, Benchmark test calculation of a four-nucleon bound state, *Phys. Rev. C* **64**, 44001 (2001).

[8] B. S. PUDLINER, V. R. PANDHARIPANDE, J. CARLSON and R. B. WIRINGA, Quantum Monte Carlo Calculations of $A \leq 6$ Nuclei, *Phys. Rev. Lett.* **74**, 4396 (1995).

[9] S. C. PIEPER and R. B. WIRINGA, Quantum Monte Carlo calculations of light nuclei, *Ann. Rev. Nucl. Part. Sci.* **51**, 53 (2001).

[10] B. S. PUDLINER, V. R. PANDHARIPANDE, J. CARLSON, S. C. PIEPER and R. B. WIRINGA, Quantum Monte Carlo calculations of nuclei with $A \leq 7$, *Phys. Rev. C* **56**, 1720 (1997).

[11] R. B. WIRINGA, S. C. PIEPER, J. CARLSON and V. R. PANDHARIPANDE, Quantum Monte Carlo calculations of $A = 8$ nuclei, *Phys. Rev. C* **62**, 14001 (2000).

[12] S. C. PIEPER, K. VARGA and R. B. WIRINGA, Quantum Monte Carlo calculations of $A = 9, 10$ nuclei, *Phys. Rev. C* **66**, 44310 (2002).

[13] P. NAVRÁTIL, J. P. VARY and B. R. BARRETT, Properties of ^{12}C in the Ab Initio Nuclear Shell Model, *Phys. Rev. Lett.* **84**, 5728 (2000).

[14] P. NAVRÁTIL, J. P. VARY and B. R. BARRETT, Large-basis ab initio no-core shell model and its application to ^{12}C, *Phys. Rev. C* **62**, 54311 (2000).

[15] P. NAVRÁTIL and W. E. ORMAND, Ab Initio Shell Model Calculations with Three-Body Effective Interactions for *p*-Shell Nuclei, *Phys. Rev. Lett.* **88**, 152502 (2002).

[16] E. CAURIER, P. NAVRÁTIL, W. E. ORMAND and J. P. VARY, Ab initio shell model for $A = 10$ nuclei, *Phys. Rev. C* **66**, 24314 (2002).

[17] D. J. DEAN and M. HJORTH-JENSEN, Coupled-cluster approach to nuclear physics, *Phys. Rev. C* **69**, 54320 (2004).

[18] S. FUJII, R. OKAMOTO and K. SUZUKI, Charge-dependent calculations of single-particle energies in nuclei around ^{16}O with modern nucleon-nucleon interactions, *Phys. Rev. C* **69**, 34328 (2004).

[19] K. KOWALSKI, D. J. DEAN, M. HJORTH-JENSEN, T. PAPENBROCK and P. PIECUCH, Coupled Cluster Calculations of Ground and Excited States of Nuclei, *Phys. Rev. Lett.* **92**, 132501 (2004).

[20] G. HAGEN, D. J. DEAN, M. HJORTH-JENSEN, T. PAPENBROCK and A. SCHWENK, Benchmark calculations for ^{3}H, ^{4}He, ^{16}O and ^{40}Ca with ab initio coupled-cluster theory, *Phys. Rev. C* **76**, 44305 (2007).

[21] S. FUJII, T. MIZUSAKI, T. OTSUKA, T. SEBE and A. ARIMA, Microscopic shell-model description of the exotic nucleus ^{16}C, *Phys. Lett. B* **650**, 9 (2007).

[22] T. H. R. SKYRME, The nuclear surface, *Phil. Mag.* **1**, 1043 (1956).

[23] J. S. BELL and T. H. R. SKYRME, The nuclear spin-orbit coupling, *Phil. Mag.* **1**, 1055 (1956).

[24] D. VAUTHERIN and D. M. BRINK, Hartree-Fock Calculations with Skyrme's Interaction. I. Spherical Nuclei, *Phys. Rev. C* **5**, 626 (1972).

[25] D. VAUTHERIN, Hartree-Fock Calculations with Skyrme's Interaction. II. Axially Deformed Nuclei, *Phys. Rev. C* **7**, 296 (1973).

[26] D. GOGNY, Simple separable expansions for calculating matrix elements of two-body local interactions with harmonic oscillator functions, *Nucl. Phys. A* **237**, 399 (1975).

[27] J. DECHARGÉ and D. GOGNY, Hartree-Fock-Bogolyubov calculations with the *D*1 effective interaction on spherical nuclei, *Phys. Rev. C* **21**, 1568 (1980).

[28] B. D. SEROT and J. WALECKA, The relativistic nuclear many-body problem, *Adv. Nucl. Phys.* **16**, 1 (1986).

[29] P. RING and P. SCHUCK, The nuclear many body problem, Springer-Verlag, Berlin (1980).

[30] M. BENDER, P.-H. HEENEN and P.-G. REINHARD, Self-consistent mean-field models for nuclear structure, *Rev. Mod. Phys.* **75**, 121 (2003).

[31] T. R. RODRÍGUEZ and J. L. EGIDO, New Beyond-Mean-Field Theories: Examination of the Potential Shell Closures at $N = 32$ or 34, *Phys. Rev. Lett.* **99**, 62501 (2007).

[32] M. G. MAYER, On Closed Shells in Nuclei, *Phys. Rev.* **74**, 235 (1948).

[33] M. G. MAYER, On Closed Shells in Nuclei. II, *Phys. Rev.* **75**, 1969 (1949).

[34] O. HAXEL, J. H. D. JENSEN and H. E. SUESS, On the "Magic Numbers" in Nuclear Structure, *Phys. Rev.* **75**, 1766 (1949).

[35] M. G. MAYER, Nuclear Configurations in the Spin-Orbit Coupling Model. I. Empirical Evidence, *Phys. Rev.* **78**, 16 (1950).

[36] V. R. PANDHARIPANDE, I. SICK and P. K. A. DEWITT HUBERTS, Independent particle motion and correlations in fermion systems, *Rev. Mod. Phys.* **69**, 981 (1997).

[37] L. TALMI and I. UNNA, Theoretical Interpretation of Energy Levels in Light Nuclei, *Ann. Rev. Nucl. Part. Sci.* **10**, 353 (1960).

[38] J. D. MCCULLEN, B. F. BAYMAN and L. ZAMICK, Spectroscopy in the Nuclear $1f_{\frac{7}{2}}$ Shell, *Phys. Rev.* **134**, B515 (1964).

[39] A. P. ZUKER, B. BUCK and J. B. MCGRORY, Structure of ^{16}O, *Phys. Rev. Lett.* **21**, 39 (1968).

[40] B. A. BROWN and B. H. WILDENTHAL, Status of the nuclear shell model, *Ann. Rev. Nucl. Part. Sci.* **38**, 29 (1988).

[41] E. CAURIER, A. P. ZUKER, A. POVES and G. MARTÍNEZ-PINEDO, Full pf shell model study of $A = 48$ nuclei, *Phys. Rev. C* **50**, 225 (1994).

[42] G. MARTÍNEZ-PINEDO, A. P. ZUKER, A. POVES and E. CAURIER, Full pf shell study of $A = 47$ and $A = 49$ nuclei, *Phys. Rev. C* **55**, 187 (1997).

[43] A. POVES, J. SÁNCHEZ-SOLANO, E. CAURIER and F. NOWACKI, Shell model study of the isobaric chains $A = 50$, $A = 51$ and $A = 52$, *Nucl. Phys. A* **694**, 157 (2001).

[44] E. CAURIER, F. NOWACKI and A. POVES, Shell Model Description of the Decay Out of the Superdeformed Band of ^{36}Ar, *Phys. Rev. Lett.* **95**, 042502 (2005).

[45] A. GNIADY, E. CAURIER and F. NOWACKI, to be published.

[46] V. G. J. STOKS, R. A. M. KLOMP, M. C. M. RENTMEESTER and J. J. DE SWART, Partial-wave analysis of all nucleon-nucleon scattering data below 350 MeV, *Phys. Rev. C* **48**, 792 (1993).

[47] H. YUKAWA, On the Interaction of Elementary Particles, *Proc. Phys. Math. Soc. Jap.* **17**, 48 (1935).

[48] V. G. J. STOKS, R. A. M. KLOMP, C. P. F. TERHEGGEN and J. J. DE SWART, Construction of high-quality NN potential models, *Phys. Rev. C* **49**, 2950 (1994).

[49] R. B. WIRINGA, V. G. J. STOKS and R. SCHIAVILLA, Accurate nucleon-nucleon potential with charge-independence breaking, *Phys. Rev. C* **51**, 38 (1995).

[50] R. MACHLEIDT, F. SAMMARRUCA and Y. SONG, Nonlocal nature of the nuclear force and its impact on nuclear structure, *Phys. Rev. C* **53**, R1483 (1996).

[51] R. MACHLEIDT, High-precision, charge-dependent Bonn nucleon-nucleon potential, *Phys. Rev. C* **63**, 24001 (2001).

[52] S. WEINBERG, Nuclear forces from chiral lagrangians, *Phys. Lett. B* **251**, 288 (1990).

[53] S. WEINBERG, Effective chiral lagrangians for nucleon-pion interactions and nuclear forces, *Nucl. Phys. B* **363**, 3 (1991).

[54] D. R. ENTEM and R. MACHLEIDT, Accurate nucleon nucleon potential based upon chiral perturbation theory, *Phys. Lett. B* **524**, 93 (2002).

[55] D. R. ENTEM and R. MACHLEIDT, Accurate Charge-Dependent Nucleon-Nucleon Potential at Fourth Order of Chiral Perturbation Theory, *Phys. Rev. C* **68**, 41001 (2003).

[56] K. A. BRUECKNER, C. A. LEVINSON and H. M. MAHMOUD, Two-Body Forces and Nuclear Saturation. I. Central Forces, *Phys. Rev.* **95**, 217 (1954).

[57] K. A. BRUECKNER, Nuclear Saturation and Two-Body Forces. II. Tensor Forces, *Phys. Rev.* **96**, 508 (1954).

[58] K. A. BRUECKNER, Two-Body Forces and Nuclear Saturation. III. Details of the Structure of the Nucleus, *Phys. Rev.* **97**, 1353 (1955).

[59] K. A. BRUECKNER and C. A. LEVINSON, Approximate Reduction of the Many-Body Problem for Strongly Interacting Particles to a Problem of Self-Consistent Fields, *Phys. Rev.* **97**, 1344 (1955).

[60] M. HJORTH-JENSEN, T. KUO and E. OSNES, Realistic effective interactions for nuclear systems, *Phys. Rep.* **261**, 125 (1997).

[61] T. T. S. KUO and G. E. BROWN, Structure of finite nuclei and the free nucleon-nucleon interaction. An application to ^{18}O and ^{18}F, *Nucl. Phys.* **85**, 40 (1966).

[62] T. T. S. KUO and G. E. BROWN, Reaction matrix elements for the $0f-1p$ shell nuclei, *Nucl. Phys. A* **114**, 241 (1968).

[63] S. KAHANA, H. C. LEE and C. K. SCOTT, Effect of Woods-Saxon Wave Functions on the Calculation of $A = 18,\ 206,\ 210$ Spectra with a Realistic Interaction, *Phys. Rev.* **180**, 956 (1969).

[64] T. HAMADA and I. D. JOHNSTON, A potential model representation of two-nucleon data below 315 MeV, *Nucl. Phys.* **34**, 382 (1962).

[65] S. BOGNER, T. T. S. KUO and L. CORAGGIO, Low momentum nucleon-nucleon potentials with half-on-shell T-matrix equivalence, *Nucl. Phys. A* **684**, 432c (2001).

[66] S. K. BOGNER, T. T. S. KUO and A. SCHWENK, Model-independent low momentum nucleon interaction from phase shift equivalence, *Phys. Rep.* **386**, 1 (2003).

[67] S. K. BOGNER, T. T. S. KUO, A. SCHWENK, D. R. ENTEM and R. MACHLEIDT, Towards a model-independent low momentum nucleon-nucleon interaction, *Phys. Lett. B* **576**, 265 (2003).

[68] A. SCHWENK and A. P. ZUKER, Shell-model phenomenology of low-momentum interactions, *Phys. Rev. C* **74**, 61302 (2006).

[69] B. H. WILDENTHAL, Empirical strengths of spin operators in nuclei, *Prog. Part. Nucl. Phys.* **11**, 5 (1984).

[70] W. A. RICHTER, M. G. VAN DER MERWE, R. E. JULIES and B. A. BROWN, New effective interactions for the $0f1p$ shell, *Nucl. Phys. A* **523**, 325 (1991).

[71] M. HONMA, T. OTSUKA, B. A. BROWN and T. MIZUSAKI, Effective interaction for pf-shell nuclei, *Phys. Rev. C* **65**, 61301 (2002).

[72] A. ABZOUZI, E. CAURIER and A. P. ZUKER, Influence of saturation properties on shell-model calculations, *Phys. Rev. Lett.* **66**, 1134 (1991).

[73] A. P. ZUKER and M. DUFOUR, Separation of the monopole contribution to the nuclear Hamiltonian (1995), nucl-th/9505012.

[74] E. PASQUINI, Ph.D. thesis, Université Louis Pasteur, Strasbourg (1976).

[75] E. PASQUINI and A. P. ZUKER, in P. BLASI and R. A. RICCI (eds.), Physics of Medium Light Nuclei, Editrice Compositiori, Bologna, Florence (1977).

[76] A. POVES and A. P. ZUKER, Theoretical spectroscopy and the fp shell, *Phys. Rep.* **70**, 235 (1981).

[77] A. P. ZUKER, Three-body monopole corrections to the realistic interactions, *Phys. Rev. Lett.* **90**, 42502 (2003).

[78] M. DUFOUR and A. ZUKER, The realistic collective nuclear Hamiltonian, *Phys. Rev. C* **54**, 1641 (1996).

[79] J. B. FRENCH, E. C. HALBERT, J. B. MCGRORY and S. S. M. WONG, Advances in Nuclear Physics, chap. Complex spectroscopy, p. 193, Plenum, New York (1969).

[80] R. R. WHITEHEAD, A. WATT, B. J. COLE and I. MORRISON, Computational methods for shell-model calculations, *Adv. Nucl. Phys.* **9**, 123 (1977).

[81] A. ETCHEGOYEN, W. D. M. RAE, N. S. GODWIN, W. A. RICHTER, C. H. ZIMMERMAN, B. A. BROWN, W. E. ORMAND and J. S. WINFIELD, OXBASH Shell Model code, Tech. Rep. 524, MSU-NSCL (1985).

[82] B. A. BROWN, The nuclear shell model towards the drip lines, *Prog. Part. Nucl. Phys.* **47**, 517 (2001).

[83] E. CAURIER, A. P. ZUKER and A. POVES, A Full $0\hbar\omega$ description of the $2\nu\beta\beta$ decay of ^{48}Ca, *Phys. Lett. B* **252**, 13 (1990).

[84] E. CAURIER, A. POVES and A. P. ZUKER, Spin quenching and orbital enhancement in the Ti isotopes, *Phys. Lett. B* **256**, 301 (1991).

[85] F. NOWACKI, Description microcospique des processus faibles dans les noyaux spheriques, Ph.D. thesis, Centre de Recherches Nucleaires, Strasbourg (1996).

[86] E. CAURIER, G. MARTÍNEZ-PINEDO, F. NOWACKI, A. POVES, J. RETAMOSA and A. P. ZUKER, Full $0\hbar\omega$ shell model calculation of the binding energies of the $1f_{7/2}$ nuclei, *Phys. Rev. C* **59**, 2033 (1999).

[87] E. CAURIER and F. NOWACKI, Present Status of Shell Model Techniques, *Act. Phys. Pol. B* **30**, 705 (1999).

[88] E. CAURIER, G. MARTINEZ-PINEDO, F. NOWACKI, A. POVES and A. P. ZUKER, The Shell Model as Unified View of Nuclear Structure, *Rev. Mod. Phys.* **77**, 427 (2005).

[89] S. E. KOONIN, D. J. DEAN and K. LANGANKE, Shell Model Monte Carlo Methods, *Phys. Rep.* **278**, 1 (1997).

[90] T. OTSUKA, M. HONMA, T. MIZUSAKI, N. SHIMIZU and Y. UTSUNO, Monte Carlo shell model for atomic nuclei, *Prog. Part. Nucl. Phys.* **47**, 319 (2001).

[91] A. BOHR, The coupling of nuclear surface oscillations to the motion of individual nucleons, *Kgl. Danske Videnskab. Selskab, Mat.-fys. Medd.* **26**, 1 (1952).

[92] A. BOHR and B. R. MOTTELSON, Collective and individual-particle aspects of nuclear structure, *Kgl. Danske Videnskab. Selskab, Mat.-fys. Medd.* **27**, 2 (1953).

[93] C. F. V. WEIZSÄCKER, Zur Theorie der Kernmassen, *Z. Phys.* **96**, 431 (1935).

[94] H. A. BETHE and R. F. BACHER, Nuclear Physics *A*. Stationary States of Nuclei, *Rev. Mod. Phys.* **8**, 82 (1936).

[95] A. BOHR and B. R. MOTTELSON, Nuclear Structure, vol. 2, W. A. Benjamin, Inc., New York (1969).

[96] S. G. NILSSON, Binding states of individual nucleons in strongly deformed nuclei, *Kgl. Danske Videnskab. Selskab, Mat.-fys. Medd.* **29**, 1 (1955).

[97] R. E. PEIERLS and J. YOCCOZ, The Collective Model of Nuclear Motion, *Proc. Phys. Soc. A* **70**, 381 (1957).

[98] A. BOHR, B. R. MOTTELSON and D. PINES, Possible Analogy between the Excitation Spectra of Nuclei and Those of the Superconducting Metallic State, *Phys. Rev.* **110**, 936 (1958).

[99] J. P. ELLIOTT, Collective Motion in the Nuclear Shell Model. I. Classification Schemes for States of Mixed Configurations, *Proc. R. Soc. London Ser. A* **245**, 128 (1958).

[100] J. P. ELLIOTT, Collective Motion in the Nuclear Shell Model. II. The Introduction of Intrinsic Wave-Functions, *Proc. R. Soc. London Ser. A* **245**, 562 (1958).

[101] A. ARIMA, M. HARVEY and K. SHIMIZU, Pseudo LS coupling and pseudo SU(3) coupling schemes, *Phys. Lett. B* **30**, 517 (1969).

[102] K. T. HECHT and A. ADLER, Generalized seniority for favored $J \neq 0$ pairs in mixed configurations, *Nucl. Phys. A* **137**, 129 (1969).

[103] A. P. ZUKER, J. RETAMOSA, A. POVES and E. CAURIER, Spherical shell model description of rotational motion, *Phys. Rev. C* **52**, 1741 (1995).

[104] E. B. CARTER, G. E. MITCHELL and R. H. DAVIS, Elastic Scattering of Alpha Particles by ^{12}C in the Bombarding Energy Range 10 to 19 MeV, *Phys. Rev.* **133**, B1421 (1964).

[105] P. CHEVALLIER, F. SCHEIBLING, G. GOLDRING, I. PLESSER and M. W. SACHS, Breakup of ^{16}O into ^{8}Be+^{8}Be, *Phys. Rev.* **160**, 827 (1967).

[106] G. E. BROWN and A. M. GREEN, Even parity states of ^{16}O and ^{17}O, *Nucl. Phys.* **75**, 401 (1966).

[107] R. MIDDLETON, J. D. GARRETT and H. T. FORTUNE, Search for multiparticle-multihole states of ^{40}Ca with the ^{32}S(^{12}C,α) reaction, *Phys. Lett. B* **39**, 339 (1972).

[108] D. RUDOLPH, C. BAKTASH, M. J. BRINKMAN, E. CAURIER, D. J. DEAN, M. DEVLIN, J. DOBACZEWSKI, P.-H. HEENEN, H.-Q. JIN, D. R. LAFOSSE, W. NAZAREWICZ, F. NOWACKI, A. POVES, L. L. RIEDINGER, D. G. SARANTITES, W. SATUŁA and C.-H. YU, Rotational Bands in the Doubly Magic Nucleus ^{56}Ni, *Phys. Rev. Lett.* **82**, 3763 (1999).

[109] C. E. SVENSSON, A. O. MACCHIAVELLI, A. JUODAGALVIS, A. POVES, I. RAGNARSSON, S. ÅBERG, D. E. APPELBE, R. A. E. AUSTIN, C. BAKTASH, G. C. BALL, M. P. CARPENTER, E. CAURIER, R. M. CLARK, M. CROMAZ, M. A. DELEPLANQUE, R. M. DIAMOND, P. FALLON, M. FURLOTTI, A. GALINDO-URIBARRI, R. V. F. JANSSENS, G. J. LANE, I. Y. LEE, M. LIPOGLAVSEK, F. NOWACKI, S. D. PAUL, D. C. RADFORD and D. G. SARANTITES, Superdeformation in the $N = Z$ Nucleus ^{36}Ar: Experimental, Deformed Mean Field, and Spherical Shell Model Descriptions, *Phys. Rev. Lett.* **85**, 2693 (2000).

[110] E. IDEGUCHI, D. G. SARANTITES, W. REVIOL, A. V. AFANASJEV, M. DEVLIN, C. BAKTASH, R. V. F. JANSSENS, D. RUDOLPH, A. AXELSSON, M. P. CARPENTER, A. GALINDO-URIBARRI, D. R. LAFOSSE, T. LAURITSEN, F. LERMA, C. J. LISTER, P. REITER, D. SEWERYNIAK, M. WEISZFLOG and J. N. WILSON, Superdeformation in the Doubly Magic Nucleus $^{40}_{20}$Ca$_{20}$, *Phys. Rev. Lett.* **87**, 222501 (2001).

[111] L. ZAMICK, The importance of the strong isotopic spin dependence of particle-hole matrix elements on the many particle-many hole states in nuclei, *Phys. Lett.* **19**, 580 (1965).

[112] W. J. GERACE and A. M. GREEN, The effect of deformed states in the Ca isotopes, *Nucl. Phys. A* **93**, 110 (1967).

[113] W. J. GERACE and A. M. GREEN, K-band mixing and 8p-8h states in ^{40}Ca, *Nucl. Phys. A* **123**, 241 (1968).

[114] D. C. ZHENG, D. BERDICHEVSKY and L. ZAMICK, Calculations of many-particle–many-hole deformed state energies: Near degeneracies, deformation condensates, *Phys. Rev. C* **38**, 437 (1988).

[115] G.-L. LONG and Y. SUN, Superdeformed Band in ^{36}Ar Described by Projected Shell Model, *Phys. Rev. C* **63**, 21305 (2001).

[116] T. INAKURA, S. MIZUTORI, M. YAMAGAMI and K. MATSUYANAGI, Cranked Skyrme-Hartree-Fock calculation for superdeformed and hyperdeformed rotational bands in $N = Z$ nuclei from ^{32}S to ^{48}Cr, *Nucl. Phys. A* **710**, 261 (2002).

[117] M. BENDER, H. FLOCARD and P. H. HEENEN, Beyond-mean-field-model analysis of low-spin normal-deformed and superdeformed collective states of ^{32}S, ^{36}Ar, ^{38}Ar and ^{40}Ca, *Phys. Rev. C* **68**, 44321 (2003).

[118] R. R. RODRIGUEZ-GUZMAN, J. L. EGIDO and L. M. ROBLEDO, Description of the superdeformed band of ^{36}Ar with the Gogny force, *Int. J. Mod. Phys.* **E13**, 139 (2004).

[119] S. BHOWAL, S. DAS and G. GANGOPADHYAY, Many-particle many-hole states near the magic number 20: deformed and superdeformed states (2004), nucl-th/0404043.

[120] T. SAKUDA and S. OHKUBO, Superdeformation and α-cluster structure of the nucleus ^{36}Ar, *Nucl. Phys. A* **744**, 77 (2004).

[121] Y. KANADA-EN'YO and M. KIMURA, Superdeformation and clustering in ^{40}Ca studied with Antisymmetrized Molecular Dynamics, *Phys. Rev. C* **72**, 64322 (2005).

[122] Y. TANIGUCHI, M. KIMURA, Y. KANADA-EN'YO and H. HORIUCHI, Clustering and Triaxial Deformations of ^{40}Ca, *Phys. Rev. C* **76**, 44317 (2007).

[123] M. OI, Description of superdeformed bands in light $N = Z$ nuclei using the cranked HFB method, *Phys. Rev. C* **76**, 44308 (2007).

[124] E. CAURIER, F. NOWACKI, A. POVES and A. ZUKER, The superdeformed excited band of ^{40}Ca (2002), nucl-th/0205036.

[125] A. POVES, E. CAURIER, F. NOWACKI and A. ZUKER, Spherical shell model description of deformation and superdeformation, *Eur. Phys. J. A* **20**, 119 (2003).

[126] I. ANGELI, A consistent set of nuclear rms charge radii: properties of the radius surface $R(N,Z)$, *At. Data Nucl. Data Tables* **87**, 185 (2004).

[127] E. CAURIER, J. MENÉNDEZ, F. NOWACKI and A. POVES, Coexistence of spherical states with deformed and superdeformed bands in doubly magic ^{40}Ca: A shell-model challenge, *Phys. Rev. C* **75**, 054317 (2007).

[128] E. CAURIER, J. MENÉNDEZ, F. NOWACKI and A. POVES, Erratum:Coexistence of spherical states with deformed and superdeformed bands in doubly magic ^{40}Ca: A shell-model challenge [Phys. Rev. C **75**, 54317 (2007)], *Phys. Rev. C* **76**, 049901 (2007).

[129] J. L. WOOD, K. HEYDE, N. NAZAREVICH, M. HUYSE and P. VAN DUPPEN, Coexistence in even-mass nuclei, *Phys. Rept.* **215**, 101 (1992).

[130] C. J. CHIARA, E. IDEGUCHI, M. DEVLIN, D. R. LAFOSSE, F. LERMA, W. REVIOL, S. K. RYU, D. G. SARANTITES, C. BAKTASH, A. GALINDO-URIBARRI, M. P. CARPENTER, R. V. F. JANSSENS, T. LAURITSEN, C. J. LISTER, P. REITER, D. SEWERYNIAK, P. FALLON, A. GÖRGEN, A. O. MACCHIAVELLI and D. RUDOLPH, Transition quadrupole moments in the superdeformed band of ^{40}Ca, *Phys. Rev. C* **67**, 41303 (2003).

[131] P. M. ENDT, Energy levels of $A = 21 - 44$ nuclei (VII), *Nucl. Phys. A* **521**, 1 (1990).

[132] A. S. DAVYDOV and G. F. FILIPPOV, Rotational states in even atomic nuclei, *Nuclear Physics* **8**, 237 (1958).

[133] M. GOEPPERT-MAYER, Double Beta-Disintegration, *Phys. Rev.* **48**, 512 (1935).

[134] S. R. ELLIOTT, A. A. HAHN and M. K. MOE, Direct evidence for two-neutrino double-beta decay in ^{82}Se, *Phys. Rev. Lett.* **59**, 2020 (1987).

[135] A. S. BARABASH, Average and recommended half-life values for two neutrino double beta decay: Upgrade'05, *Czech. J. Phys.* **56**, 437 (2006).

[136] W. H. FURRY, On Transition Probabilities in Double Beta-Disintegration, *Phys. Rev.* **56**, 1184 (1939).

[137] E. MAJORANA, Teoria simmetrica dell'elettrone e del positrone, *Nuov. Cim.* **14**, 171 (1937).

[138] Y. FUKUDA, T. HAYAKAWA, E. ICHIHARA, K. INOUE, K. ISHIHARA, H. ISHINO, Y. ITOW, T. KAJITA, J. KAMEDA, S. KASUGA, K. KOBAYASHI, Y. KOBAYASHI, Y. KOSHIO, M. MIURA, M. NAKAHATA, S. NAKAYAMA, A. OKADA, K. OKUMURA, N. SAKURAI, M. SHIOZAWA, Y. SUZUKI, Y. TAKEUCHI, Y. TOTSUKA, S. YAMADA, M. EARL, A. HABIG and E. KEARNS, Evidence for Oscillation of Atmospheric Neutrinos, *Phys. Rev. Lett.* **81**, 1562 (1998).

[139] Q. R. AHMAD, R. C. ALLEN, T. C. ANDERSEN, J. D.ANGLIN, J. C. BARTON, E. W. BEIER, M. BERCOVITCH, J. BIGU, S. D. BILLER, R. A. BLACK, I. BLEVIS, R. J. BOARDMAN, J. BOGER, E. BONVIN, M. G. BOULAY, M. G. BOWLER, T. J. BOWLES, S. J. BRICE, M. C. BROWNE, T. V. BULLARD, G. BÜHLER, J. CAMERON, Y. D. CHAN, H. H. CHEN, M. CHEN, X. CHEN and B. T. CLEVELAND, Direct Evidence for Neutrino Flavor Transformation from Neutral-Current Interactions in the Sudbury Neutrino Observatory, *Phys. Rev. Lett.* **89**, 11301 (2002).

[140] K. EGUCHI, S. ENOMOTO, K. FURUNO, J. GOLDMAN, H. HANADA, H. IKEDA, K. IKEDA, K. INOUE, K. ISHIHARA, W. ITOH, T. IWAMOTO, T. KAWAGUCHI, T. KAWASHIMA, H. KINOSHITA, Y. KISHIMOTO, M. KOGA, Y. KOSEKI, T. MAEDA, T. MITSUI, M. MOTOKI, K. NAKAJIMA, M. NAKAJIMA, T. NAKAJIMA, H. OGAWA, K. OWADA, T. SAKABE and I. SHIMIZU, First Results from KamLAND: Evidence for Reactor Antineutrino Disappearance, *Phys. Rev. Lett.* **90**, 21802 (2003).

[141] H. V. KLAPDOR-KLEINGROTHAUS, A. DIETZ, H. L. HARNEY and I. V. KRIVOSHEINA, Evidence for neutrinoless double beta decay, *Mod. Phys. Lett.* **A16**, 2409 (2001).

[142] H. V. KLAPDOR-KLEINGROTHAUS, I. V. KRIVOSHEINA, A. DIETZ and O. CHKVORETS, Search for neutrinoless double beta decay with enriched ^{76}Ge in Gran Sasso 1990-2003, *Phys. Lett. B* **586**, 198 (2004).

[143] R. ARNOLD, C. AUGIER, J. BAKER, A. BARABASH, G. BROUDIN, V. BRUDANIN, A. J. CAFFREY, E. CAURIER, V. EGOROV, K. ERRAHMANE, A. I. ETIENVRE, J. L. GUYONNET, F. HUBERT, P. HUBERT, C. JOLLET, S. JULLIAN, O. KOCHETOV, V. KOVALENKO, S. KONOVALOV, D. LALANNE, F. LECCIA, C. LONGUEMARE, G. LUTTER, C. MARQUET, F. MAUGER, F. NOWACKI, H. OHSUMI, F. PIQUEMAL, J. L. REYSS, R. SAAKYAN, X. SARAZIN, L. SIMARD, F. ŠIMKOVIC, Y. SHITOV, A. SMOLNIKOV, L. STEKL, J. SUHONEN, C. S. SUTTON, G. SZKLARZ, J. THOMAS, V. TIMKIN, V. TRETYAK, V. UMATOV, L. VALA, I. VANUSHIN, V. VASILYEV, V. VOROBEL and T. VYLOV, First Results of the Search for Neutrinoless Double-Beta Decay with the NEMO 3 Detector, *Phys. Rev. Lett.* **95**, 182302 (2005).

[144] C. ARNABOLDI, D. R. ARTUSA, F. T. A. III, M. BALATA, I. BANDAC, M. BARUCCI, J. W. BEEMAN, C. BROFFERIO, C. BUCCI, S. CAPELLI, L. CARBONE, S. CEBRIAN, O. CREMONESI, R. J. CRESWICK, A. DE WAARD, H. A. FARACH, E. FIORINI, G. FROSSATI, E. GUARDINCERRI, A. GIULIANI, P. GORLA, E. E. HALLER, R. J. MCDONALD, A. MORALES, E. B. NORMAN, A. NUCCIOTTI, E. OLIVIERI, M. PALLAVICINI, E. PALMIERI, E. PASCA, M. PAVAN, M. PEDRETTI, G. PESSINA, S. PIRRO, E. PREVITALI, L. RISEGARI, C. ROSENFELD, S. SANGIORGIO, M. SISTI, A. R. SMITH, L. TORRES and G. VENTURA, New Limit on the Neutrinoless beta beta Decay of ^{130}Te, *Phys. Rev. Lett.* **95**, 142501 (2005).

[145] F. T. AVIGNONE III, S. R. ELLIOTT and J. ENGEL, Double Beta Decay, Majorana Neutrinos, and Neutrino Mass, *Rev. Mod. Phys.* **80**, 481 (2008).

[146] M. DOI, T. KOTANI, H. NISHIURA, K. OKUDA and E. TAKASUGI, Neutrino masses and the double beta decay, *Phys. Lett. B* **103**, 219 (1981).

[147] M. DOI, T. KOTANI and E. TAKASUGI, Double beta Decay and Majorana Neutrino, *Prog. Theor. Phys. Suppl.* **83**, 1 (1985).

[148] J. SUHONEN, From nucleons to nucleus, Springer (2007).

[149] J. BAREA and F. IACHELLO, private communication.

[150] J. RETAMOSA, E. CAURIER and F. NOWACKI, Neutrinoless double beta decay of ^{48}Ca, *Phys. Rev. C* **51**, 371 (1995).

[151] E. CAURIER, F. NOWACKI, A. POVES and J. RETAMOSA, Shell Model Studies of the Double Beta Decays of ^{76}Ge, ^{82}Se, and ^{136}Xe, *Phys. Rev. Lett.* **77**, 1954 (1996).

[152] E. CAURIER, F. NOWACKI, A. POVES and J. RETAMOSA, Shell Model Study of the Neutrinoless Double Beta Decays, *Nucl. Phys. A* **654**, 973 (1999).

[153] E. CAURIER, F. NOWACKI and A. POVES, Nuclear Structure Aspects of the Neutrinoless Double Beta Decay, *Eur. Phys. J. A.* **36**, 195 (2008).

[154] E. CAURIER, J. MENÉNDEZ, F. NOWACKI and A. POVES, The influence of pairing on the nuclear matrix elements of the neutrinoless double beta decays, *Phys. Rev. Lett.* **100**, 52503 (2008).

[155] J. MENENDEZ, A. POVES, E. CAURIER and F. NOWACKI, Disassembling the Nuclear Matrix Elements of the Neutrinoless double beta Decay (2008), arXiv:0801.3760.

[156] J. D. VERGADOS, Lepton violating $\beta^-\beta^-$,$\beta^+\beta^+$ decays (e^-,e^+) conversion and double electron capture in gauge theories., *Nucl. Phys. B* **218**, 109 (1983).

[157] I. S. TOWNER and J. C. HARDY, in W. C. HAXTON and E. M. HENLEY (eds.), Symmetries and Fundamental Interactions in Nuclei, chap. Currents and their Couplings in the Weak Sector of the Standard Model, pp. 183–249, World Scientific Publishing Company (1995).

[158] K. MUTO, Neutrinoless double beta decay beyond closure approximation, *Nucl. Phys. A* **577**, 415c (1994).

[159] F. ŠIMKOVIC, G. PANTIS, J. D. VERGADOS and A. FAESSLER, Additional nucleon current contributions to neutrinoless double beta decay, *Phys. Rev. C* **60**, 55502 (1999).

[160] H. F. WU, H. Q. SONG, T. T. S. KUO, W. K. CHENG and D. STROTTMAN, Majorana neutrino and lepton number nonconservation in ^{48}Ca double beta decay, *Phys. Lett. B* **162**, 227 (1985).

[161] G. A. MILLER and J. E. SPENCER, A Survey of Pion Charge-Exchange Reactions with Nuclei, *Ann. Phys.* **100**, 562 (1976).

[162] M. KORTELAINEN, O. CIVITARESE, J. SUHONEN and J. TOIVANEN, Short-range correlations and neutrinoless double beta decay, *Phys. Lett. B* **647**, 128 (2007).

[163] H. FELDMEIER, T. NEFF, R. ROTH and J. SCHNACK, A unitary correlation operator method, *Nucl. Phys. A* **632**, 61 (1998).

[164] R. ROTH, H. HERGERT, P. PAPAKONSTANTINOU, T. NEFF and H. FELDMEIER, Matrix Elements and Few-Body Calculations within the Unitary Correlation Operator Method, *Phys. Rev. C* **72**, 34002 (2005).

[165] M. KORTELAINEN and J. SUHONEN, Improved short-range correlations and 0nu beta beta nuclear matrix elements of ^{76}Ge and ^{82}Se, *Phys. Rev. C* **75**, 51303 (2007).

[166] V. A. RODIN, A. FAESSLER, F. ŠIMKOVIC and P. VOGEL, Erratum: Assessment of uncertainties in QRPA 0νββ-decay nuclear matrix elements [Nucl. Phys. A 766, 107 (2006)], *Nucl. Phys. A* **793**, 213 (2007).

[167] J. SUHONEN and M. KORTELAINEN, Nuclear Matrix Elements for Double Beta Decay, *Int. J. Mod. Phys. E* **17**, 1 (2008).

[168] F. ŠIMKOVIC, A. FAESSLER, V. A. RODIN, P. VOGEL and J. ENGEL, Anatomy of nuclear matrix elements for neutrinoless double-beta decay, *Phys. Rev. C* **77**, 45503 (2008).

[169] M. KORTELAINEN and J. SUHONEN, Nuclear matrix elements of neutrinoless double beta decay with improved short-range correlations, *Phys. Rev. C* **76**, 24315 (2007).

[170] J. ENGEL and G. HAGEN, private communication.

[171] F. SIMKOVIC, A. FAESSLER and P. VOGEL, 0νββ nuclear matrix elements and the occupancy of individual orbits (2008), arXiv:0812.0348.

[172] J. SUHONEN, Neutrinoless double beta decay to excited collective 0^+ states, *Phys. Lett. B* **477**, 99 (2000).

[173] J. SUHONEN, Sub-eV neutrino masses from 0νββ decay to an excited 0^+ state, *Phys. Rev. C* **62**, 42501 (2000).

[174] J. SUHONEN, Opening of the $Z = 40$ subshell gap and the double-beta decay of ^{100}Mo, *Nucl. Phys. A* **700**, 649 (2002).

[175] J. SUHONEN and M. AUNOLA, Systematic study of neutrinoless double beta decay to excited 0^+ states, *Nucl. Phys. A* **723**, 271 (2003).

[176] F. ŠIMKOVIC, M. NOWAK, W. A. KAMINSKI, A. A. RADUTA and A. FAESSLER, Neutrinoless double beta decay of ^{76}Ge, ^{82}Se, ^{100}Mo and ^{136}Xe to excited 0^+ states, *Phys. Rev. C.* **64**, 35501 (2001).

[177] J. P. SCHIFFER, S. J. FREEMAN, J. A. CLARK, C. DEIBEL, C. R. FITZPATRICK, S. GROS, A. HEINZ, D. HIRATA, C. L. JIANG, B. P. KAY, A. PARIKH, P. D. PARKER, K. E. REHM, A. C. C. VILLARI, V. WERNER and C. WREDE, Nuclear Structure Relevant to Neutrinoless Double Beta Decay: ^{76}76 and ^{76}Se, *Phys. Rev. Lett.* **100**, 112501 (2008).

[178] B. P. KAY, J. P. SCHIFFER, S. J. FREEMAN, T. ADACHI, J. A. CLARK, C. DEIBEL, H. FUJITA, Y. FUJITA, P. GRABMAYR, K. HATANAKA, D. ISHIKAWA, H. MATSUBARA, Y. MEADA, H. OKAMUDA, K. E. REHM, Y. SAKEMI, Y. SHIMIZU, H. SHIMODA, K. SUDA, Y. TAMESHIGE, A. TAMII and C. WREDE, Nuclear Structure Relevant to Neutrinoless Double Beta Decay: the Valence Protons in ^{76}Ge and ^{76}Se (2008), arXiv:0810.4108.

[179] J. MENENDEZ, A. POVES, E. CAURIER and F. NOWACKI, Deformation and the Nuclear Matrix Elements of the Neutrinoless Double Beta Decay (2008), arXiv:0809.2183.

[180] F. ŠIMKOVIC and P. VOGEL, private communication.

[181] R. ÁLVAREZ RODRÍGUEZ, P. SARRIGUREN, E. MOYA DE GUERRA, L. PACEARESCU, A. FAESSLER and F. ŠIMKOVIC, A deformed QRPA formalism for single and two-neutrino double beta decay, *Phys. Rev.* **C70**, 64309 (2004).

[182] K. CHATURVEDI, R. CHANDRA, P. K. RATH, P. K. RAINA and J. G. HIRSCH, Nuclear deformation and neutrinoless double-β decay of ^{94,96}Zr, ^{98,100}Mo, ^{104}Ru, ^{110}Pd, ^{128,130}Te and ^{150}Nd nuclei in mass mechanism, *Phys. Rev.* **C78**, 54302 (2008).

[183] F. NOWACKI, private communication.

[184] J. SUHONEN and O. CIVITARESE, Neutrinoless beta-beta matrix element of ^{76}Ge from spectroscopic data, *Phys. Lett. B* **668**, 277 (2008).

[185] J. MENG, K. SUGAWARA-TANABE, S. YAMAJI, P. RING and A. ARIMA, Pseudospin symmetry in relativistic mean field theory, *Phys. Rev. C* **58**, R628 (1998).

[186] D. J. DEAN, M. T. RESSELL, M. HJORTH-JENSEN, S. E. KOONIN, K. LANGANKE and A. P. ZUKER, Shell-model Monte Carlo studies of neutron-rich nuclei in the $1s-0d-1p-0f$ shells, *Phys. Rev. C* **59**, 2474 (1999).